Blue-Emitting Ligand-Mediated Assembly of Rare-Earth MOFs toward White-Light Emission, Sensing, Magnetic, and Catalytic Studies

Krishna Manna, J. P. Sutter, Srinivasan Natarajan

Blue Emitting Ligand Mediated Assembly of Rare-Earth MOFs Towards White-Light Emission, Sensing, Magnetic and Catalytic Studies

Krishna Manna[a], Jean-Pascal Sutter[b]* and Srinivasan Natarajan[a]*

(a) Ms. Krishna Manna, Prof. S. Natarajan:
Framework solids Laboratory, Solid State and Structural Chemistry Unit
Indian Institute of Science
Bangalore 560012 (India)
Email: snatarajan@iisc.ac.in
Homepage: http://sscu.iisc.ac.in/people/frameworkslab/

(b) Dr. Jean-Pascal Sutter
Laboratoire de Chimie de Coordination du CNRS
Université de Toulouse, CNRS
205 route de Narbonne, 31077 Toulouse (France)
E-mail : jean-pascal.sutter@lcc-toulouse.fr

ABSTRACT:

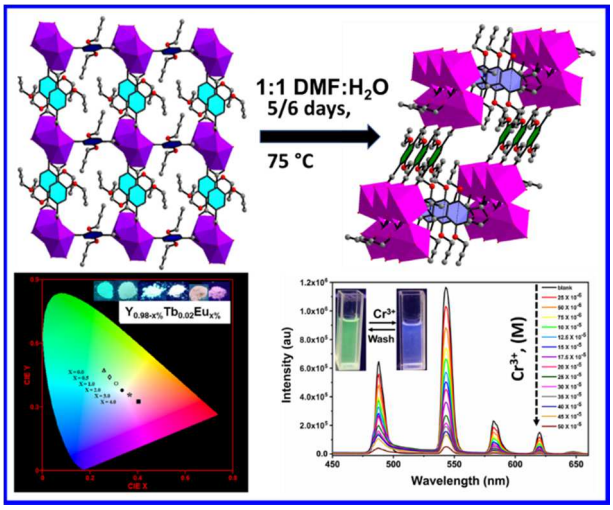

New lanthanide Carboxylate compounds with two – and three – dimensional structure have been prepared employing 2, 5-bis(prop-2-yn-1-yloxy)terephthalic acid (2, 5 – BPTA) as the organic linker. The compounds, $[Ln(C_{14}H_8O_6)(C_7O_3H_4)\cdot 2H_2O]\cdot 4(H_2O)$, Ln = Y, Pr, Nd, Sm, Eu, Gd, Tb, Dy; and $[Ln(C_7O_3H_4)_3.(C_3H_7ON).(H_2O)]\cdot 2(H_2O)$ (C_3H_7NO), Ln = La, Ce, Pr; have two- and three-dimensional structures, respectively. In all the compounds, lanthanide ions are connected together forming a dimer, which are connected by the 2, 5 - BPTA ligand. In the two-dimensional structure, there are two 2, 5 - BPTA moieties present and in the three-dimensional structure, there are three 2, 5 – BPTA moieties present. The lanthanide centers are nine-coordinated and in the 2D-structure has a tricapped trigonal prismatic arrangement and, in the 3D-structure has a mono-capped distorted square antiprismatic arrangement. The Pr compound forms both in 2D as well as in the 3D structure, the formation of which depends on the time of reaction (2 days-2D and 5-6 days 3D). The ligand emits in the blue region and using the characteristic emission of Eu^{3+} (red) and Tb^{3+} (green) ions, we have achieved white light emission in $(Y_{0.96}Tb_{0.02}Eu_{0.02})$ – compound. The overall quantum yield for the white light emission is 28%. The strong green luminescence of the Tb^{3+} containing compound was employed to selectively sense the Cr^{3+} and Fe^{3+} ions, in aqueous solution with the limit of detection (LOD) at 0.41 and 8.6 ppm, respectively. Tb-compound was found to be a good heterogeneous catalyst for the Ullman type O – Arylation reaction between phenol and bromoarene with yields of 95%. Magnetic studies on the Gd, Tb and Dy containing compounds showed weak exchange interactions within the dimeric Ln2 units. The present work demonstrates the many utilities of the rare earth containing MOFs, especially towards white - light emission, metal – ion sensing and heterogeneous catalysis.

Keywords: Metal Organic Framework, Lanthanide, Magnetism, White Light Emission, Sensing, O Arylation reaction

INTRODUCTION:

Metal-organic frameworks (MOFs) also known as coordination polymers (CPs) have been in the forefront of important hybrid materials during the last two decades.[1–3] Their large surface area, tunable porosity and functionality, have contributed towards the target specific guest-accessible applications in the areas of gas storage and capture, gas separation, catalysis, magnetism, drug delivery etc.[4–15]

Recent research on luminescent MOFs, based on lanthanides, has been attracting considerable attention. Most of the early efforts on MOF compounds were focused on porous MOFs. The lanthanide MOFs, are attractive due to the high coordination numbers, which can be gainfully utilised to prepare compounds with unusual structure.[16–22] In addition, the properties emerging from the *f-f* electronic transitions can lead to compounds having element specific emission with high quantum yield. The *f-f* transitions, and their emissions in general, are characteristically sharp giving brilliant colours.[23–25] The organic linkers employed in the preparation of rare earth MOFs can perform the role of the sensitizer by transferring the absorbed energy to the metal centre via inter-system crossing leading to characteristic emissions – the antenna effect.[26–30]

The Lanthanide ions exhibits specific luminescence when excited suitably. Thus, Eu^{3+} ions give red colour, Tb^{3+} ions exhibit green colour and Tm^{3+} ions exhibit blue colour. It has been shown that a combination of these ions in an inert host can give rise to white light emission and much studies have been carried out in this direction.[31–33] The white light emitting materials find wide applications in lasers, indicators, displays etc.[34–36] The white-light has also been produced by the combination of dichromatic components (blue and yellow)[37–42] and also by trichromatic components (red, green and blue)[43–46]. In the trichromatic approach, the MOF exhibits a blue emission and the red and green emissions are generated by substitutions employing Eu^{3+} and Tb^{3+} ions in the host. [47–50]This combination gives rise to white light emission.

Another area which attracted the attention of many researchers working with MOFs is sensing of metal ions. [51–55] Of the many metal ions Cr^{3+} and Fe^{3+} ions, has important role in biological activity. Iron and Chromium are extensively employed in electroplating, paints, tanning and steel manufacturing.[56–60] It is necessary that the detection of these in the effluents of the above industries to treat them for safer disposal. The unique emission behaviour of the lanthanide ions can be utilised for the detection of those elements by employing fluorimetry.[61–67]

The MOFs have found a number of applications in the area of heterogeneous catalysis. Both Lewis acid and base catalysis as well as Brönsted acid catalysis have been carried out

employing different MOFs.[68–73] Many important, multi-component green catalysis have been attempted successfully using MOFs. One such reaction is Ullman type coupling for the synthesis of diaryl ethers.[74–76] Buchwald and Hartwig employed Pd-catalysts for the reaction between aryl halides and phenols.[77–80] Many C-O coupling reactions are also known using transition metal catalysts.[81–83] The use of the rare earth elements as catalysts for this type of reaction have not been explored much.

In the present study, new series of metal organic framework compounds based on lanthanides, has been prepared employing 2, 5-bis (prop-2-yn-1-yloxy)terephthalic acid (2,5 BPTA) as a ligand. Among the Ln^{III} lanthanides, Y, Pr, Nd, Sm, Eu, Gd, Tb and Dy form in a two-dimensional structure with a formula of $[Ln(C_{14}H_8O_6)(C_7O_3H_4)\cdot 2H_2O]\cdot 4(H_2O)$. The La and Ce containing ones form with a three-dimensional structure having the formula of $[Ln(C_7O_3H_4)_3.(C_3H_7ON).(H_2O)]\cdot 2(H_2O)(C_3H_7NO)$. The Pr containing compound can be prepared in both the two – and three – dimensional structures. The present compounds were investigated for white light emission by substituting Eu^{3+} and Tb^{3+} ions in the Y containing compound. A strong white light emission was observed for 2% substitution of Eu^{3+} and Tb^{3+} ions. The Tb-compound was explored for sensing of metal ions and exhibited selective sensing of Cr^{3+} and Fe^{3+} ions. The C–O coupling reaction between aryl halide and phenols gave diaryl ether products with good conversions and yield. In this paper, we present the synthesis, structure, luminescent, sensing and catalytic behaviour of the rare-earth MOF compounds.

EXPERIMENTAL SECTION

Materials:

The chemicals required for the synthesis of the compounds: $La(NO_3)_2.xH_2O$ (Ln= Y, La, Ce, Pr, Nd, Sm, Eu, Gd, Tb, Dy) propargyl bromide (80 wt% in toluene, 0.3% magnesium oxide as stabilizer) (Sigma-Aldrich); the compounds for the catalytic studies and 2, 5-dihyroxyterephthalic acid (TCI); THF, DMF, EtOH, KOH, MeOH, HCl (SDfine, India). The water used was double distilled through a Millipore membrane. All the chemicals were used as purchased without any further purifications.

Syntheses:

Synthesis of 2, 5-bis(prop-2-yn-1-yloxy)terephthalic acid (2,5 BPTA): 2,5-bis(prop-2-yn-1-yloxy)terephthalic acid (2,5 BPTA) was prepared using a procedure reported elsewhere.[84]

***Synthesis of [Ln($C_{14}H_8O_6$)($C_7H_4O_3$)·2H_2O]·4(H_2O); (Ln = Y, La, Ce, Pr, Nd, Sm, Eu, Gd, Tb, Dy) and [Ln($C_7O_3H_4$)$_3$.(C_3H_7ON).(H_2O)]·2(H_2O)(C_3H_7NO) (M=La, Ce, Pr)*:** All the compounds were prepared by the sequential layering of three different solutions. Thus, the ligand 2,5-BPTA (0.05 mmol, 0.013 g) was dissolved in 1 mL of N,N-DMF (Solution **A**). The lanthanide nitrates, $Ln(NO_3)_2 \cdot xH_2O$, (0.05 mmol , ~0.020 g) was dissolved in 1 mL water (Solution **C**). Buffer solution (1 mL) was prepared by mixing 1:1 H_2O and DMF (Solution **B**). In a Teflon-capped reaction vessel, solution **C** (1 mL) containing the lanthanide salt was added at the bottom. Then, 1 mL of solution **B** was carefully layered on the top of solution **C** followed by the addition of 1 mL of solution **A**. The reaction vessel was closed with a cap, and kept undisturbed in an oven at 75 ºC for 3-6 days. In the case of La, Ce and Pr, large amount of cubic block shaped crystals were isolated after 2-3 days. The remaining lanthanides, including Y, gave products with similar morphology after 6 days. Except for Nd (light purple) and Pr (light green), the remaining crystals were found to be yellowish in colour. We made attempts to prepare 2D analogues of La and Ce and also the 3D analogue of the remaining lanthanides by carrying out many variations of the reaction conditions. During this effort, we were successful in converting the 2D analogue of Pr compound into the 3D structure by keeping the 2D crystals in 1:1 mixture of DMF and water solution at 75 °. In spite of our best efforts, we could not convert any other compound from 2D to3D or vice versa. The crystals were separated by filtration after washing with water, it was dried under vacuum condition. The yield in all cases was found to be in the range of ~60 - 70 % with respect to the lanthanide ions. Elemental analysis for all the compounds is listed in Table S1. Powder X-ray diffraction (PXRD) studies (Figure S1) has confirmed the phase purity of the prepared samples. The mixed metal compounds were also prepared employing a similar procedure (Figure S2, S3).

INITIAL CHARACTERIZATION:

Initial characterization of all the compounds were characterised employing a number of techniques. PXRD patterns were recorded using Cu Kα radiation (PANalytical, Empyrean, λ = 1.5418 Å) (Figure S1, S2, S3). The UV-Vis spectra were recorded using PerkinElmer Lambda 950 UV/vis double beam spectrometer at room temperature (Figure S4). Infrared (IR) spectra were recorded at room temperature (PerkinElmer Spectrum 1000) (Figure S5). Elemental analyses (carbon, oxygen, hydrogen, and nitrogen) were performed in a Thermo Finnigan EA Flash 1112 Series. PerkinElmer Optima 2000DV spectrometer has been used to perform ICP-OES study. Thermogravimetric analysis (TGA) (Metler-Toledo) was carried out in an N_2 atmosphere (flow rate = 40 mL/min) in the temperature range 30– 800 °C (heating

rate = 5 °C/min) (Figure S6, S7). The photoluminescence studies were carried out at room temperature (Horiba Fluoromax Plus). Employing an Edinburgh Instruments, FLS 920 spectrofluorometer Luminescence decay studies were carried out. Absolute solid-state quantum yields were measured with a calibrated Horiba JOBIN YVON integrating sphere. ^{1}H NMR data were collected using a Bruker 400 MHz spectrometer. Chemical shifts are reported in ppm using tetramethylsilane as the internal reference. High resolution mass spectra were obtained from Q-TOF instrument by electrospray ionization (ESI). JEOL JSM-6500F has been used to record SEM and EDX data. Magnetic measurements for all the samples were carried out with a Quantum Design MPMS 5S SQUID magnetometer in the temperature range 2−300 K. The measurements were performed on polycrystalline samples kept in gelatin capsules. The crystalline powders of the complexes of Tb and Dy were mixed with grease. The temperature dependence of the magnetization was measured in an applied field of 1kOe and the isothermal field dependence of the magnetizations were collected up to 5 T. The molar susceptibility (χ_M) was corrected for sample holder, grease and for the diamagnetic contribution of all the atoms by using Pascal's tables. AC susceptibility data have been collected for AC frequency of 997 Hz, with and without applied field of 1 kOe

Single crystal structure determination.

The single crystal structure was determined at 100 K using a Bruker SMART APEX CCD X-ray diffractometer (graphite-monochromator, $\lambda = 0.71073$ Å). The cell refinements and absorption corrections were carried out by SAINT[85] and SADABS[86] programs. Direct methods were used to solve the structure using SHELXL2018 suite of programs.[87] The guest molecules were disordered and the SQUEEZE option in PLATON was employed for the compounds **9 - 11**.[88] After the squeeze routine, 57, 55 and 51 electrons per asymmetric unit were found to be squeezed that corresponded to one DMF and two H_2O molecules. A summary of crystal data and the relevant refinement parameters for compounds **1-8** and **9-11** are presented in Table 1 and Table 2. CCDC 2184686-2184693 and 2184743-2184745 contain the crystallographic data for this paper. The data can be obtained free of charge from The Cambridge Crystallographic Data Centre via www.ccdc.cam.ac.uk/data_request/cif.

Structural parameter	**Compound 1**	**Compound 2**	**Compound 3**	**Compound 4**	**Compound5**	**Compound 6**	**Compound 7**	**Compound 8**
Empirical formula	$[Y(C_{14}H_8O_6)(C_7O_3H_4)\cdot 2H_2O]\cdot 4(H_2O)$	$[Pr(C_{14}H_8O_6)(C_7O_3H_4)\cdot 2H_2O]\cdot 4(H_2O)$	$[Nd(C_{14}H_8O_6)(C_7O_3H_4)\cdot 2H_2O]\cdot 4(H_2O)$	$[Sm(C_{14}H_8O_6)(C_7O_3H_4)\cdot 2H_2O]\cdot 4(H_2O)$	$[Eu(C_{14}H_8O_6)(C_7O_3H_4)\cdot 2H_2O]\cdot 4(H_2O)$	$[Gd(C_{14}H_8O_6)(C_7O_3H_4)\cdot 2H_2O]\cdot 4(H_2O)$	$[Tb(C_{14}H_8O_6)(C_7O_3H_4)\cdot 2H_2O]\cdot 4(H_2O)$	$[Dy(C_{14}H_8O_6)(C_7O_3H_4)\cdot 2H_2O]\cdot 4(H_2O)$
Crystal system	Triclinic	Triclinic	Triclinic	Triclinic	Triclinic	Triclinic	Triclinic	Triclinic
Space group	P-*1*	P-*1*	P-*1*	P-*1*	P-*1*	P-*1*	P-*1*	P-*1*
a (Å)	10.54 (2)	10.53(3)	10.52(3)	10.50(4)	10.49(7)	10.48 (8)	10.47(7)	10.57(1)
b (Å)	11.43 (2)	11.48(3)	11.49(4)	11.46(4)	11.45(8)	11.44(8)	11.44(7)	11.45(11)
c (Å)	11.52(3)	11.60(3)	11.59(4)	11.53(4)	11.52(7)	11.50(8)	11.48(8)	11.50(11)
α(°)	88.17(1)	79.09(1)	79.21(2)	79.29(2)	79.28(3)	79.36(3)	79.37(3)	88.2(4)
β(°)	63.011(1)	76.31(1)	76.3(2)	76.44(2)	76.52(3)	76.45(3)	76.50(3)	62.97(4)
γ(°)	76.436(1)	63.25(1)	63.19(1)	63.18(2)	63.21(3)	63.18(2)	63.10(2)	76.59(4)
V (Å^3)	1196.95(5)	1211.14(6)	1209.40(7)	1199.46(8)	1195.68(14)	1191.92(15)	1187.04(14)	1202.0(2)
Z	2	2	2	2	2	2	2	2
T(K)	100(2)	100(2)	100(2)	100(2)	100(2)	100(2)	100(2)	100(2)
ρ_{calcd} (g cm^{-3})	1.68	1.82	1.81	1.81	1.85	1.88	1.89	1.85
μ (mm^{-1})	2.5	1.09	2.22	2.53	2.70	2.86	3.057	3.19
λ (Mo Kα/Å)	0.71073	0.71073	0.71073	0.71073	0.71073	0.71073	0.71073	0.71073
θ range (deg)	1.84-30.57	1.81-30.59	1.82-30.59	1.824–30.600	1.83-30.60	1.83-30.55	1.83-30.54	1.84-30.68
Final *R* indices[$I>2\sigma(I)$]	*R1*=0.034 *wR2*= 0.092	*R1*=0.035 *wR2*= 0.099	*R1*= 0.032 *wR2*= 0.085	*R1*=0.029 *wR2*= 0.079	*R1*= 0.034 *wR2*= 0.088	*R1*= 0.028 *wR2*= 0.078	*R1*= 0.028 *wR2*= 0.077	*R1*= 0.025 *wR2*= 0.071
R indices (all data)	*R1*= 0.039 *wR2*= 0.095	*R1*=0.036 *wR2*= 0.099	*R1*= 0.033 *wR2*= 0.086	*R1*= 0.029 *wR2*= 0.08	*R1*= 0.038 *wR2*= 0.091	*R1*= 0.028 *wR2*= 0.078	*R1*= 0.029 *wR2*= 0.077	*R1*= 0.026 *wR2*= 0.072
R_{int}	0.027	0.029	0.022	0.020	0.030	0.0281	0.0343	0.022

[a] $R_1 = \sum ||F_o| - |F_c|| / \sum |F_o|$; $wR_2 = \{\sum [w(F_o^2 - F_c^2)] / \sum [w(F_o^2)^2]\}^{1/2}$.
$w = 1/[\rho^2(F_o)^2 + (aP)^2 + bP]$. $P = [\max(F_o, 0) + 2(F_c)^2]/3$
where a = 0.050 and b = 1.28for **1;** a =0.050 and b = 4.66 for **2;** a =0.04 and b = 4.16 for **3;** a =0.04 and b = 3.92 for **4;** a =0.041 and b = 5.19 for **5;** a =0.037 and b = 3.72 for **6;** a =0.032 and b = 4.84 for **7;** a =0.039 and b = 1.98 for **8.**

Table 1: Crystallographic data and structure refinement parameters for 2D compounds **1-8**[a]

Structural parameter	**Compound 9**	**Compound 10**	**Compound 11**
Empirical formula	$[La(C_7O_3H_4)_3.(C_3H_7ON).(H_2O)]\cdot 2(H_2O)(C_3H_7NO)$	$[Ce(C_7O_3H_4)_3.(C_3H_7ON)(H_2O)]\cdot 2(H_2O)(C_3H_7NO))$	$[Pr_2(C_7O_3H_4)_6\cdot(C_3H_7ON)_2(H_2O)_2]\cdot 2(H_2O)(C_3H_7NO)$
Crystal system	Triclinic	Triclinic	Triclinic
Space group	P-*1*	P-*1*	P-*1*
a (Å)	10.09(7)	10.05(7)	10.095(8)
b (Å)	11.25(7)	11.23(8)	11.14(9)
c (Å)	13.82(9)	13.83(10)	13.72(11)
α(º)	74.40(4)	73.893(4)	74.07(3)
β(º)	72.85(4)	72.665(4)	72.80(4)
γ(º)	80.08(4)	80.032(3)	79.71(4)
V ($Å^3$)	1435.45(17)	1424.77(18)	1409.8(2)
Z	2	2	2
T(K)	100(2)	100(2)	100(2)
ρ_{calcd} (g cm^{-3})	1.47	1.491	1.462
μ (mm^{-1})	1.54	1.65	1.78
λ (Mo Kα/Å)	0.71073	0.71073	0.71073
θ range (deg)	1.59-30.69	1.59-30.58	
Final *R* indices[$I > 2\sigma(I)$]	*R1*=0.059 *wR2* = 0.15	*R1*= 0.043 *wR2* = 0.11	*R1*= 0.037 *wR2* = 0.093
R indices (all data)	*R1*=0.068 *wR2*= 0.16	*R1*= 0.0468 *wR2*= 0.12	*R1*= 0.034 *wR2*= 0.095
R_{int}	0.041	0.031	0.021

[a] $R_1 = \sum ||F_o| - |F_c|| / \sum |F_o|$; $wR_2 = \{\sum [w(F_o^2 - F_c^2)] / \sum [w(F_o^2)^2]\}^{1/2}$.
$w = 1/[\rho^2(F_o)^2 + (aP)^2 + bP]$. $P = [\max(F_o, 0) + 2(F_c)^2]/3$
where a = 0.108 and b = 1.70 for **9;** a =0.050 and b = 4.66 for **10;** a = 0.064 and b = 3.96 for **11**

Table 2: Crystallographic data and structure refinement parameters for 3D compounds **9-11**[a]

UV – Vis and IR investigations:

The room temperature UV-Vis spectra of the ligand (Figure S4) showed absorption bands corresponding to the л–л* (278 nm) and the n–л* (340 nm) transitions. Compound **1-11** exhibited a small red-shift in the UV-Vis spectra of both the л–л* and n–л* transitions at 280 and 320-350 nm. In addition to the ligand-centred transitions, the characteristic lanthanide *f-f* transitions are observed (Table S6). Similar absorptions have been observed before.[89,90]

Infrared (IR) Spectroscopic Studies:

The IR spectra (Figure S5) of the ligand, 2, 5 BPTA and the compounds were recorded at room temperature. The IR bands are in the range expected for the various moieties in the structure. The important observed IR bands and their corresponding assignments are given in Table S7.[91]

Thermal Studies:

Thermogravimetric analysis (TGA) on all the compounds has been carried out from 30–800 °C in N_2 flow (heating rate = 5 °C/min, Figure S6 and S7). The thermal decomposition behaviour of all the two-dimensional compounds were found to be similar (Figure S6). For example, the Tb compound (**7**), a weight loss of ~14.8% was observed in the region of 100 - 150 °C, which corresponds to the loss of six water molecules that indicates both the lattice water and coordinated one (calc. 16%). A second and continuous weight loss in the broad temperature range of 250–500 °C, corresponds to the decomposition of all the organic moieties.

For the three-dimensional compounds, for example the Ce-Compound (**10**), a weight loss of 4.5% in the temperature range of room temperature to 70 °C corresponds to the loss of two uncoordinated water molecules (calc. 4.8%). The weight loss of 11.1% at ~ 220 °C corresponds to the loss of one uncoordinated DMF and one coordinated H_2O molecules (calc. 12.1%). Further broad and gradual weight loss in the temperature range of 220-700 °C corresponds to all the solvent molecules along with the elimination of the organic molecules (Figure S7). The final calcined product for all the compounds was found to be the corresponding oxides of the lanthanides (Figure S8).

RESULTS AND DISCUSSION:

Structure of the two-Dimensional compounds: $[Ln(C_{14}H_8O_6)(C_7H_4O_3)\cdot 2H_2O]\cdot 4(H_2O)$; (Ln = Y(1), Pr (2), Nd(3), Sm(4), Eu(5), Gd(6), Tb(7), Dy(8))

The compounds $[Ln(C_{14}H_8O_6)(C_7H_4O_3)\cdot 2H_2O]\cdot 4(H_2O)$, **1-8** (Ln = Y, Pr, Nd, Sm, Eu, Gd, Tb, Dy) has two dimensional structure. For example, the structure of Yttrium compound (**1**) would

be described here. The asymmetric unit contains 36 non-hydrogen atoms with one crystallographically independent Y^{3+} ion and one and half 2, 5, BPTA anion (Figure S9a). The acid, 2,5 BPTA can be classified into two different types (acid-1 and acid-2) (Figure S9b). There are six water molecules present in the asymmetric unit, of which two are coordinated [O(100) and O(200)] and the remaining [O(300), O(400), O(500) and O(600)] are present as extra framework moieties. The extra-framework water molecules are located in between the layers.

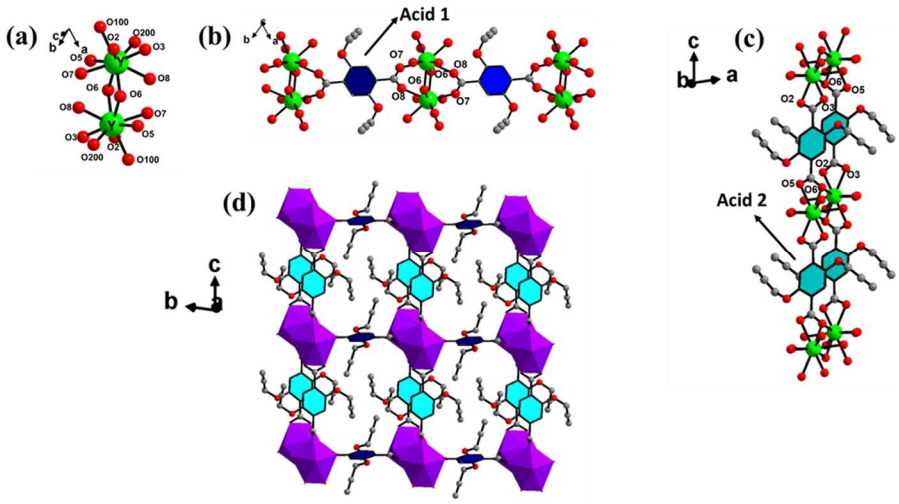

Figure 1: (a) Y units are connected another Y through a μ3 coordinated oxygen (O (6)) forming a dimer**, (b)**, **(c)** Dimers are connected via acid 1 and acid 2 forming one dimensional chains. **(d)** 2-dimensional layer formation

The Y^{3+} ion is surrounded by nine oxygen atoms with a distorted tricapped trigonal prismatic arrangement (Figure S10a). Of the nine oxygens, two oxygens, O(100), and O(200) are coordinated water molecules, and the remaining seven oxygens are from the carboxylate group. Among the carboxylate oxygens, O(6) has a *μ3* connectivity connecting two metal centres and a carbon, and all the remaining have *μ2* connectivity (one metal centre and one carbon atom). The Y-O bonds have distances in the range of 2.332 (3) – 2.547 (2) Å (av: 2.419 Å), and the O-Y-O bond angles are in the range of 53.70 (6) – 152.98 (7)° (av: 85.95°)[92,93]

The selected bond distances and angles for the 2D MOF compounds from **1-8** are listed in Table S2. Of the two acids, acid 1 connects to four Y-centres through the carboxylate oxygens and acid-2 connects to three Y-centres (Figure S9b)**.** The two-dimensional structure can be explained by considering smaller building units. Thus, the yttrium polyhedral units are connected through a common edge with another Y through a μ3 coordinated oxygen (O(6)) forming a dimer (Figure 1a). The dimers are, connected to each other through the 2,5 BPTA

ligand (acid-1) forming a one-dimensional chain (Figure 1b). A similar one-dimensional chain is formed through the acid-2 (Figure 1c). The connectivity between these two one dimensional chains results in a two-dimensional layer (Figure 1d). Inter layer hydrogen bond interactions between the alkyne H(1) and the carboxylate oxygen, O(5) are present in the structure (Figure 2a). The simplified structure is given in Figure 2b. The coordinated water molecules along with the lattice water molecules occupy spaces in between the layers (Figure S11). The water molecules also interact with the layers through the H bond interaction. (Figure S11).

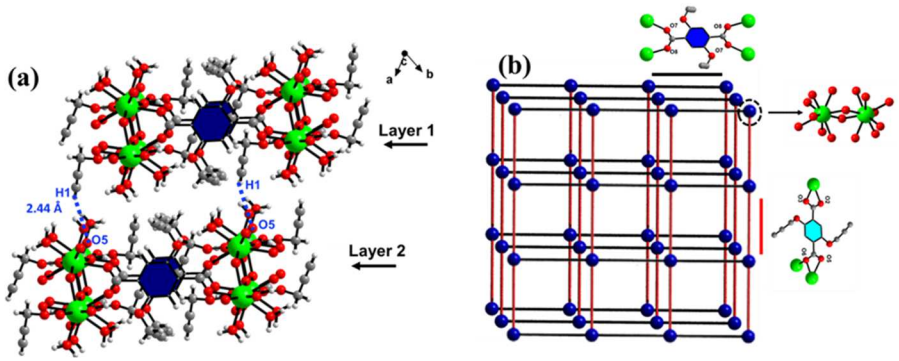

Figure 2: (a) The arrangement of the layers. Note that the layers are arranged one over the other in a AAA⋯ fashion. **(b)** Schematic view of the layers

Structure of the three-dimensional compounds

$[Ln(C_7O_3H_4)_3.(C_3H_7ON).(H_2O)]\cdot 2(H_2O)(C_3H_7NO)$ (Ln=La(9), Ce(10), Pr(11))

The compounds $[Ln(C_7O_3H_4)_3(C_3H_7ON)(H_2O)]\cdot 2(H_2O)(C_3H_7NO)$ (Ln = La(**9**), Ce(**10**), Pr(**11**)) has three dimensional structure. As a representative example, the structure of Lanthanum compound (**9**) would be described here. The asymmetric unit contains 37 non-hydrogen atoms with one crystallographically independent La^{3+} ion and one and half 2,5-BPTA anion (Figure S12a). The acid, 2,5-BPTA can be classified to be of three different types (acid-1, acid-2 and acid-3). There is one water molecule and one DMF molecules present in the asymmetric unit, both of them are coordinated [O(100) and O(DMF)].

The La^{3+} ion is surrounded by nine oxygen atoms with a distorted monocapped square antiprismatic arrangement (Figure S10b). Of the nine oxygens, two oxygens, O(100), and O(DMF) are coordinated water and DMF molecules, and the remaining seven oxygens are from the carboxylate group. Among the carboxylate oxygens, O(6) has a $\mu 3$ connectivity connecting

two metal centres and a carbon, and all the remaining have $\mu 2$ connectivity (one metal centre and one carbon atom). The La-O bonds have distances in the range of 2.444 (4)- 2.647(4) Å (av: 2.557 Å), and the O-La-O bond angles are in the range of 49.32(12)- 149.09 (14)° (av: 95.47°).[94–96] The selected bond distances and angles for all the compounds are listed in Table S4. Of the three acids, acid-1and acid-3 connects to four La-centres through the carboxylate oxygens and acid-2 connects to two La - centres (Figure S11b).

The three-dimensional structure can be explained by considering smaller building units. Thus, the lanthanum polyhedral units are connected through a μ3 coordinated oxygen (O(6)) forming a dimer (Figure 3a). The dimers are, connected to each other through the 2,5-BPTA ligand (acid-1) forming a one-dimensional chain (Figure 3b). Another one-dimensional chain are connected through acid-2 forming a two-dimensional layer (Figure 3c). The two–dimensional layers are connected through acid-3 giving rise to the observed three dimensional structure (Figure 3d, S13).

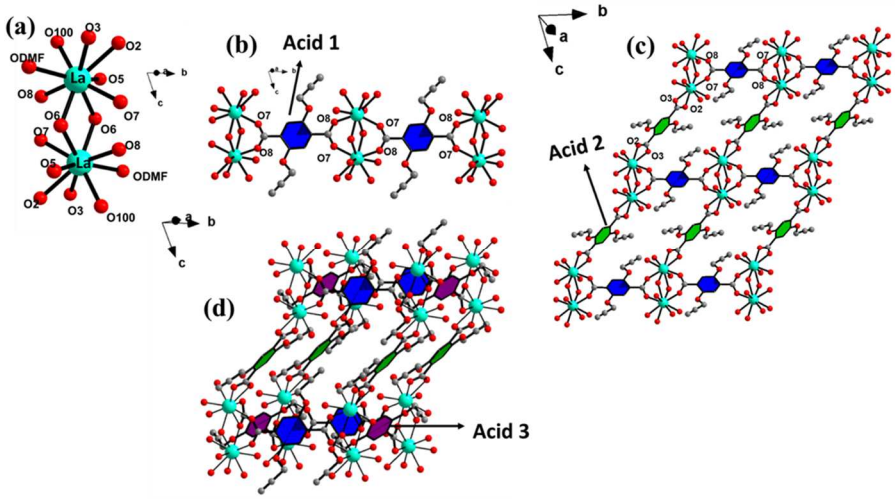

Figure 3: (a) The formation of the dimer units in the three-dimensional structure, **(b)** The connectivity between the dimers through acid-1 forming one dimensional chains, **(c)** The connectivity between the chains through Acid-2 forming the layers, **(d)** The connectivity between the layers through Acid-3 forming the three-dimensional structure.

In the present study, we have stabilized the prepared rare-earth carboxylates with two- and three-dimensional structures. The larger lanthanides, La, Ce and Pr forms in a three-dimensional structure and the remaining lanthanides including Y forms with a two-dimensional structure. The praseodymium compound forms in both the two- and three- dimensional structure. From the synthetic point of view, the Pr compound with a two-dimensional structure was isolated within 48 h of the reaction and the three-dimensional structure results when

prolonging the reaction to 5-6 days. This observation suggests that the two-dimensional structure would be a precursor to the three dimensional one. Normally, it is observed that, when there is a change in dimensionality in lanthanide structures, there is a coordination change.[97] In the present structures, we did not observe any coordination changes in the central metal. The geometry around the lanthanide ions changes from tricapped trigonal prism (2D structures) to mono-capped square antiprismatic (3D structures), which suggests a level of distortion in the 3D structure compared to the 2D structures. In the 3D structure, the lanthanide ion is coordinated by both the solvent molecules (DMF and H_2O) whereas in the 2D structures, only the H_2O molecule is coordinated. The number of acid molecules present in 2D and 3D structures are also different. In the former, there is only two acid moieties, whereas in the latter, there are three acid moieties. A combination of all the above probably resulted in the change in the overall dimensionality of the structures. Change in the dimensionality of the structure due to coordination variation of the lanthanides have been known.[98–101] Changes in the mode of connectivity between the acid and the lanthanide ions, observed in the present structures, appears to have given rise to differences in the dimensionality.[102] The present observations appear to be new and underlines the subtitles involved in the preparation of these compounds. More careful studies would be required to understand and correlate the relationships between the synthesis conditions, co-ordination geometry and mode of binding between the acids and central metal ions.

Photoluminescence investigation:

It is known that the lanthanides exhibit sharp electronic transition transitions, but needs to be sensitized by molecules having π-systems.[103] Due to the low molar absorptivity of the lanthanides, direct excitation produces weak emission spectra. Enhanced emission from rare earth ions can result when the metals are complexed or chelated with organic moieties that can efficiently absorb and transfer the energy. Direct excitation of the ligand to a singlet state followed by an intersystem crossing (ISC) to a triplet state and a nonradiative energy transfer occurs to the lanthanide ion result in the characteristic emission from the rare earth metal. The excited lanthanide ion can emit a photon or relax via a series of nonradiative processes. This effect is commonly known as the "antenna effect".[104]

The emission spectra of the Ligand, 2, 5 BPTA exhibits a broad emission centred around 428 nm. The compounds containing the rare earth ions, exhibit a broad emission band centred at 400-500 nm, when excited using a wavelength of 320 nm. This emission would be due to the intra-ligand luminescence ($\pi^* \rightarrow n$ or $\pi^* \rightarrow \pi$) (Figure S14).

For Compound **4** (Sm), and **8** (Dy), in addition to the ligand centric emissions, peaks at 568 and 606 nm were observed (λ_{ex}=320 nm). These peaks are due to the f–f transitions and for **4** (Sm), $^4G_{5/2} \rightarrow {}^6H_{5/2}$, $^6H_{7/2}$ transitions. For the Dy compound (**8**) the peaks corresponds to $F_{9/2} \rightarrow {}^6H_J$ **,** where J=15, 13, 11 (Figure S14).[105]

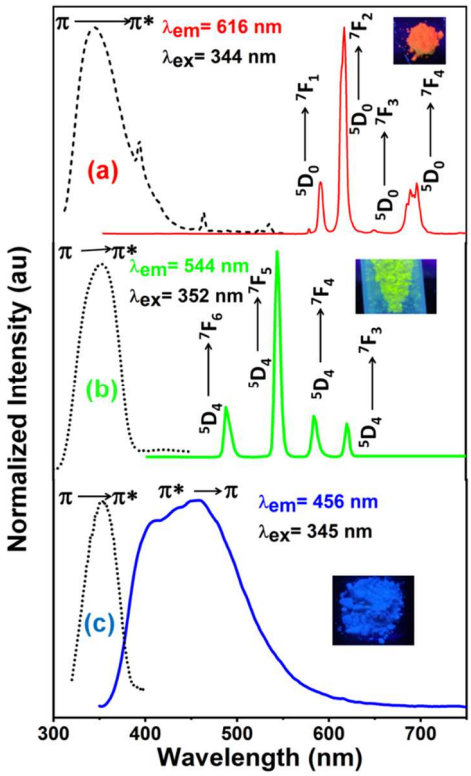

Figure 4: Excitation (black dotted) and emission spectra of (a) Eu-MOF (b) Tb-MOF (c) Y-MOF in the solid-state Inset: Photograph showing the luminescence colour of the MOFs under long UV lamp. Note the characteristic red, green and blue colour for Eu^{3+}, Tb^{3+} and the Y containing compound.

It is well established that the Eu^{3+} and Tb^{3+} ions exhibit characteristic emissions. In the present case, we observed red, green and blue emissions for (Ln = Eu^{3+} **(5)**, Tb^{3+}**(7),** and Y^{3+} **(1)**) (Figure 4). The luminescence spectra of the Y-MOF compound exhibit a blue emission in the range of 400-460 nm when excited using a wavelength of 345 nm. This is a ligand centred emission and can be assigned to the intra-ligand electronic transitions ($\pi^* \rightarrow \pi$ transition). The luminescence spectrum of the Eu compound exhibits a strong red emission upon excitation at 345 nm. The observed emission bands at 590, 617, 650 and 695 nm can be assigned to the $^5D_0 \rightarrow {}^7F_1$, $^5D_0 \rightarrow {}^7F_2$, $^5D_0 \rightarrow {}^7F_3$ and $^5D_0 \rightarrow {}^7F_4$ transitions, respectively. Similarly, the Tb compound exhibits strong green emission in the visible region upon excitation at 352 nm. The

observed emission bands at 488, 544, 585 and 620 nm can be assigned to the $^5D_4 \rightarrow {}^7F_6$, $^5D_4 \rightarrow {}^7F_5$, $^5D_4 \rightarrow {}^7F_4$ and $^5D_4 \rightarrow {}^7F_3$ transitions, respectively. It is to be noted that the excitation spectra (the dashed line) are characterized by the broad absorption bands in the ultraviolet region centred at about ~350 nm. This indicates that the compounds absorb the ultraviolet light and then sensitize the emission of lanthanides by efficient energy transfer. The ligand exhibits a red shift as well as enhanced intensity when excited at 345 nm. This may be attributed to the increased rigidity of the ligand upon coordination with the lanthanide ion. The ligand rigidity would help in reducing the loss of energy that occurs through radiation less decay during the emission. In case of Y compound, the emission exhibits a red shift as well as enhanced intensity when excited at 345 nm. It may be noted that the ligand-centred emission almost vanishes in the luminescence spectra of the Tb and the Eu compounds. This indicates that the ligand serves as an excellent chromophore for sensitizing the lanthanide ions. Similar observations have been reported previously. [104,106] We have measured the lifetime of the $^5D_0$ (Eu^{3+}), $^5D_4$ (Tb^{3+}) and Y^{3+} at ambient temperatures (298 K) by monitoring the $^5D_0 \rightarrow {}^7F_2$ (Eu^{3+}) and $^5D_4 \rightarrow {}^7F_5$ (Tb^{3+}) transitions, respectively (Figure S15). Our studies indicated that the lifetime values for the Y-compound is larger (1.323 ms) compared to the $^5D_0$ lifetime of Eu (τ = 351 μs), and $^5D_4$ lifetime of Tb (811.6 μs). The reduced lifetime of the excited state in case of Eu^{3+} and Tb^{3+} ions could be due to the non-radiative decay associated with the vibronic coupling with the coordinated water molecules. Similar lowering of the lifetime has also been observed before.[107,108]

White light emission studies:

During this study, we established strong luminescence in the blue (Y), red (Eu) and green (Tb) region of the visible range. It has been shown that optimizing the conditions (combination of red, green and blue colour) would lead to the white light emission.

To observe the white light emission, we prepared a series of Tb^{3+} and Eu^{3+} substituted Y compound by varying concentrations. The luminescence studies indicated that, at the concentrations of 5% Tb^{3+} and 9% of Eu^{3+} substitutions in the Y compound, the spectra exhibit the maximum (Figure S16, S17). Once the maximum intensity in the emission spectra is established, we made attempts to co-substitute both the Tb^{3+} and Eu^{3+} in the Y compound starting from a low concentration. Thus, 2% of Tb^{3+} substituted compound was taken as the base compound and varied the concentrations of the Eu^{3+} ion (0%, 0.5%, 1%, 2%, 3%, 4%).

The co-substituted compounds were excited employing λ=345 nm. We observed a gradual change of the colour to reach white light at 2% substitution of Eu^{3+} (Figure 5). The CIE chromaticity coordinates of the $Y_{0.98-x}Tb_{0.02}Eu_x$ - compound (x = 0, 0.5, 1.0, 2.0, 3.0, 4.0) also confirms the white light emission for 2% Eu^{3+} substitution (Figure 6, Table S8). Increase in the concentration of Eu^{3+} (x = 0 to 4) in the $Y_{0.98}Tb_{0.02}$ compound also enhances the emission intensity of the red luminescence. It may be noted that the emission intensity of Tb^{3+} decreases consistently on increasing the concentration of Eu^{3+}, which suggests that there could be an energy transfer from Tb^{3+} to Eu^{3+} ions.

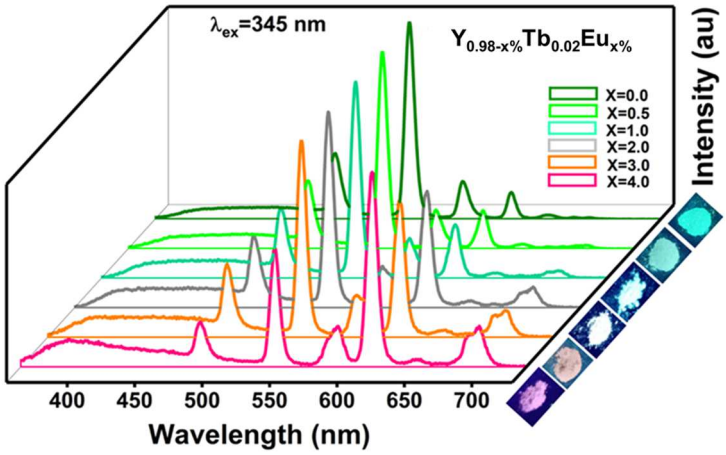

Figure 5: PL emission spectra (λ_{ex} = 345 nm) of $Y_{0.98-x\%}Tb_{0.02}Eu_{x\%}$ samples with different Eu^{3+} concentrations (0 < x < 4.0)

It is well established that the luminescence intensities of the rare-earth ions can be modified by efficient energy transfer between the ions by simultaneous substitutions in a suitable host. The transfer of energy between the Tb^{3+} and the Eu^{3+} has been known as the emissions of Tb^{3+} ions overlap with the absorption of Eu^{3+} ions. The spectral overlap between the excitation spectra of Eu^{3+} substituted Y compound and the emission spectra of Tb^{3+} substituted Y compound suggests that there is energy transfer between Tb^{3+} and Eu^{3+} (Figure S18). The excitation spectrum of the $Y_{0.98-x}Tb_{0.02}Eu_x$ – compound (x = 4%) was measured by monitoring the emission of Eu^{3+} $^5D_0 \rightarrow {}^7F_2$ transition at 616 nm, which exhibited not only the ligand-based transition and *f–f* transitions of the Eu^{3+} ions, but also the $^7F_6 \rightarrow {}^5D_4$ (488 nm) transition of the Tb^{3+} ions (Figure S19a). Similarly, the emission spectra of $Y_{0.98-x}Tb_{0.02}Eu_x$– compound (x=4%), (λ_{ex}=488 nm), gives peaks corresponding to the Eu^{3+} ions, which also indicates efficient energy transfer between the Eu^{3+} and Tb^{3+} metal centres (Figure S19b).

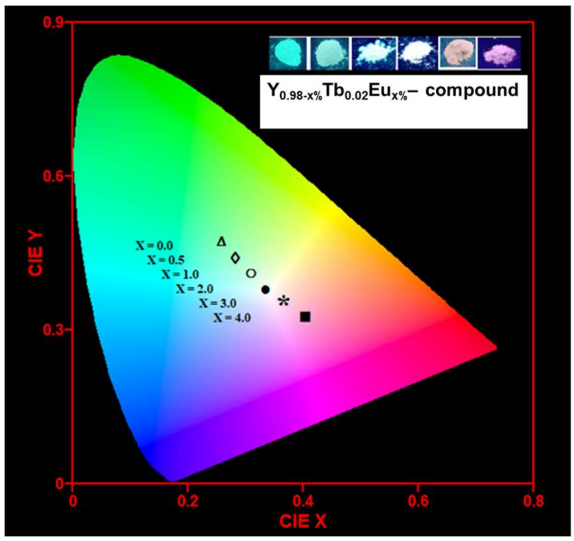

Figure 6: CIE color coordinate diagram of $Y_{0.98-x\%}Tb_{0.02}Eu_{x\%}$ samples with different Eu^{3+} concentrations ($0 < x < 4.0$). The insets are their corresponding digital photographs taken under 345 nm excitation.

To investigate the energy transfer from Tb^{3+} to Eu^{3+} ions, the fluorescence decay curves of the Tb^{3+} in $Y_{0.98-x}Tb_{0.02}Eu_x$– compound ($0 < x < 4.0$) (λ_{ex} 345 nm) were monitored following the emission of Tb^{3+} ions at 544 nm. (Figure 7). The average lifetime of the Tb^{3+} ions decrease with increasing Eu^{3+} concentration, which are 0.83, 0.75, 0.72, 0.67, 0.64 and 0.59 ms for x = 0, 0.5, 1.0, 2.0, 3.0 and 4.0, respectively. This clearly indicates and demonstrates that there is an efficient energy transfer from the Tb^{3+} to the Eu^{3+} ions in $Y_{0.98-x}Tb_{0.02}Eu_x$– MOF compound ($0 < x < 4.0$).

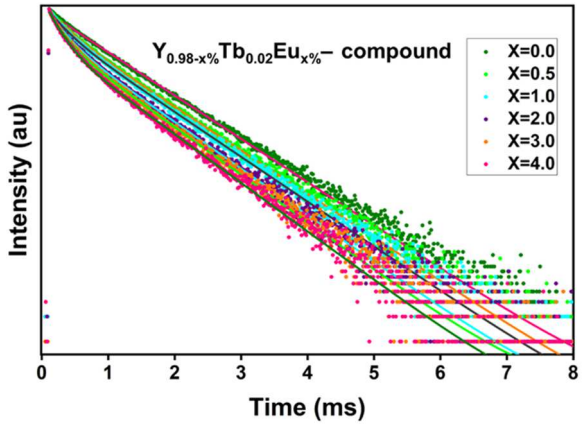

Figure 7: The decay curves for the luminescence of Tb^{3+} ions in $Y_{0.98-x\%}Tb_{0.02}Eu_{x\%}$– samples, with different Eu^{3+} concentrations (excited at 345 nm, monitored at 544 nm).

It is known that the lanthanides are sensitized using π conjugated organic molecules. The process involves excitation to the excited state singlet (S_1) followed by inter-system crossing to the triplet state (T_1) before returning to the ground state by having characteristic emission. In the present compound, $Y_{0.98-x}Tb_{0.02}Eu_x$ (x = 0, 0.5, 1.0, 2.0, 3.0 and 4.0), the Y-MOF was found to exhibit blue emission (Figure 4). When co-substituted by Tb^{3+} and Eu^{3+} ions, the ligand centred triplet state (T_1) transfers the energy to the Tb^{3+} ions ($^5D_4$) to result in characteristic Tb^{3+} emission (Figure 5). As mentioned above, the $^5D_4(Tb^{3+})$ state can transfer energy to the $^5D_0$ and $^5D_1$ states of Eu^{3+} ions through resonance energy transfer. This would populate the $^5D_0$ state of the Eu^{3+} ions and enhances the Eu^{3+} luminescence. This type of energy transfer has been observed before.[106] Thus, the combination of blue, green and red would give the white light emission (Figure 8).

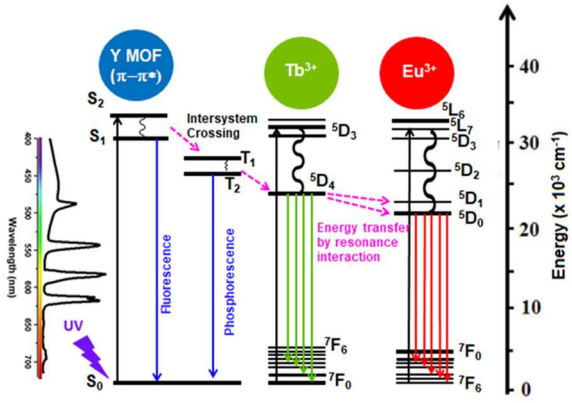

Figure 8: Schematic of possible energy transfer mechanism between the three rare earth MOF-compounds containing Y, Tb and Eu ions.

We have made attempts to prepare the Eu substituted Tb compound to investigate the possible energy transfer between Tb^{3+} and Eu^{3+} ions along with the blue emission noted for the ligand (Figure S20). A reaction was carried out in which the ligand, terbium nitrate along with europium nitrate with varying concentrations (x = 0, 0.5, 1.0, 2.0, 3.0, 4.0) was taken under the same synthesis conditions. This resulted in the terbium compound substituted with Eu^{3+} ions of varying concentrations. Our luminescence studies did not result in a white-light emission. This suggests that the intensity of the blue emission, observed for the ligand, may not be sufficient to combine with the green and red emissions from Tb^{3+} and Eu^{3+} ions to give white light emission (Figure S20). The emission studies, however, revealed that as the concentration of Eu^{3+} ions in the Tb compound increased, the luminescence of Tb^{3+} ions ($^5D_4 \rightarrow {}^7F_{6\text{-}3}$ states) diminish with an increase in the emission intensity corresponding to the Eu^{3+} ions ($^5D_0 \rightarrow {}^7F_{1\text{-}4}$

states). This clearly suggests that the energy transfer between Tb^{3+} and Eu^{3+} ions in the MOF is facile.

In addition, we attempted a study of the physical mixture Y-MOF, Tb-MOF (2%) and Eu-MOF (2%) by grinding the three compounds together to see whether we can observe the energy transfer process outlined above. Our attempts were not successful and we did not observe any white light emission. A broad blue emission along with characteristic emissions of Eu^{3+} and Tb^{3+} ions was observed by the physical mixture. This suggests that substitution of the respective rare earth ions in the same host is necessary to facilitate the efficient energy transfer and observe white light emission (Figure S21).

The quantum yield (QY) of the $Y_{0.98-x}Tb_{0.02}Eu_x$– compound (x=2%) was measured. The QY was found to be 28%. This value is comparable with those reported earlier.[38,40,48,49,109] We have also measured the individual quantum yields of the three compounds, Y, Tb and Eu MOFs and the quantum yield values were found to be 19%, 85% and 17%, respectively.[110]

Sensing studies:

As mentioned above, the Tb-MOF exhibits intense emission at 543 nm due to $^5D_4 \rightarrow {}^7F_4$ transition and also has a large quantum yield. The intense luminescence of the rare-earth ions has been exploited towards sensing of ions and molecules spectroscopically.[62,63,65,66,111] In the present compounds, we observed that the Tb-compound exhibits intense green emission with a high quantum yield of 85%. We explored the usefulness of the Tb-compound towards the metal-ion detection (Cr^{3+} and Fe^{3+}) in an aqueous solution based on the luminescence behaviour.

The aqueous dispersions of the Tb- compound was prepared by mixing 2 mg of the Tb-compound into 2.00 mL of H_2O and ultrasonicated for 1 hr. The dispersed solution was diluted to 10 mL before measuring the luminescence spectra. Different aqueous solutions of the metal nitrate salts (10 mM solution of nitrate salts of Na^+, K^+, Mg^{2+}, Cr^{3+}, Mn^{2+}, Fe^{3+}, Co^{2+}, Ni^{2+}, Zn^{2+}, Cd^{2+}) were added to 2 mL of the dispersed solution of the Tb-compound. The luminescence intensity was measured (λ_{ex}=340 nm) with and without the added metal solutions. We observed significant changes in the luminescence spectra for the addition of Cr^{3+} and Fe^{3+} solutions (Figure 9 and Figure S22).

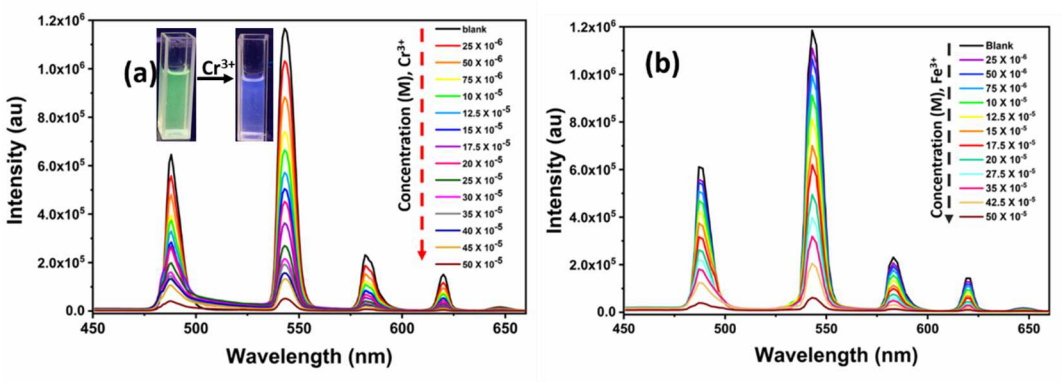

Figure 9: The change in photoluminescence intensity of **Tb -MOF** in aqueous solution at different concentrations of (a) Cr^{3+} (b) Fe^{3+}. The inset in (a) shows the change in colour of the Cr^{3+} solution in the presence of Tb-MOF compound.

The sensing of Cr^{3+} and Fe^{3+} ions were also examined in the presence of other metal ions (Figure S23). The studies indicated that the Tb-compound **(7)** is selective for Cr^{3+} and Fe^{3+} ions only. To explore the sensitivity of detection of Cr^{3+} and Fe^{3+} ions, we have carried out the luminescence quenching titrations with an incremental addition of analytes to the Tb-compound dispersed in water. Figure 9 shows the changes in the luminescence intensity with the increasing addition of the nitrates of chromium and iron nitrate solutions (up to 0.50 mM). The visible bright green emission of the Tb-MOF appears to completely vanish upon the addition of the Cr^{3+} and Fe^{3+} ions (inset, Figure 9). The loss of intensity of the emission spectra was observed to be nearly 95.7% and 94.7 % of the initial luminescence intensity (based on the $^5D_4 \rightarrow {}^7F_5$ emission of Tb compound).

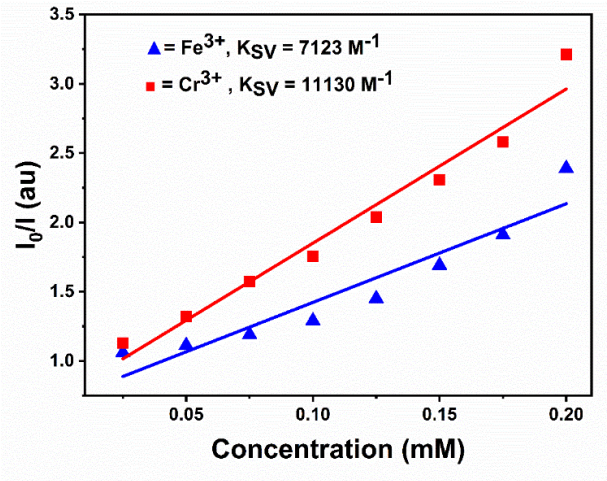

Figure 10: Stern–Volmer plots for **Tb-MOF** with Cr^{3+} (▲) and Fe^{3+} (■) at low concentrations. The solid lines represent the linear fits into the Stern–Volmer equation.

It has been shown that the Stern–Volmer (SV) plots were useful in arriving at the quenching constants of the analytes (Figure 10). The details of the SV equation and its relevance has been described and discussed before. [62,63,65,66,111] At low concentrations (up to 20 μM) of Cr^{3+} and Fe^{3+} analytes, a linear increase in the (I_0/I) was observed (Figure S24). This linear variation is due to the static quenching, that involves the interactions between the analytes and the host. The dynamic quenching, on the other hand, would involve the energy transfer between the analytes and the host. In addition, to the static and dynamic quenching, the excitation light (λ_{ex}) can also be absorbed by the analyte and contribute to the quenching of the luminescence. The fitting of the linear part of the SV plots gave the quenching constants (K_{sv}), which was found to be to be 1.1×10^4 M^{-1} for Cr^{3+} and 7.1×10^3 M^{-1} for Fe^{3+}. These values suggest good sensitivity. Thus, the Tb-MOF could be employed as a luminescence detector for Cr^{3+} and Fe^{3+} ions.

The limit of detection (LOD) was calculated to be 0.41 ppm (1.78 μM) and 8.6 ppm (36 μM), respectively, for Cr^{3+} and Fe^{3+} ions. The Tb-compound is not only selective but also good for the detection of Cr^{3+} and Fe^{3+} ions and the obtained LOD values are comparable to some of the earlier reported values in the literature.[112–114]

The quenching of the luminescence can be rationalized by examining the UV-vis spectra (Figure. S26). The UV-Vis spectra of Cr^{3+} and Fe^{3+} ions exhibit overlap between the absorption bands of the ions with that of the emission spectra of the Tb-compound **(7)** (Figure. S26). This overlap suggests the possibility of resonance energy transfer between the Tb-MOF and the cations. This would help in quenching the luminescence intensity. Apart from these, the excitation energy can also be lost due to the two possible mechanisms: (i) absorption of the excitation energy by the analytes by competing with the 2, 5 BPTA ligand, and (ii) part of excitation energy may be employed to transfer of electron from the ligand excited state to the LUMO of the analytes. The schematic of the possible energy/electron transfer processes are shown in Figure S27.

In addition to the above, we explored the possible reason for the observed quenching of the luminescence intensity during the interaction between the analytes (Cr^{3+} and Fe^{3+} ions) and the host (Tb-compound). The ligand in the host has –C≡C as part of the structure (Figure 2). The –C≡C stretching of the terminal alkyne arises in a weak band at 2119 cm^{-1} in the IR spectroscopy. On adding the Cr^{3+} and Fe^{3+} ions (up to 0.50 mM), we did not observe any

significant shift in the stretching frequency of other IR bands except the –C≡C band at 2119 cm^{-1}, which appear to lose the intensity (Figure S28). This indicates that the –C≡C moiety participates in binding with the analyte cations. From the IR spectra, the only pre-existing peaks that was perturbed was the –C≡C stretching, which indicates a possible shifting of the electron density from the bonding electrons in the alkyne group to the Cr^{3+} and Fe^{3+} ions. We did not observe any additional IR bands upon the interactions between the analytes and the MOF, which suggests that there were no chemical reaction, but only a week interaction (Figure S28). Similar observations have been reported before.[115]

A PXRD and SEM-EDX investigations were carried out after the sensing studies, which indicated that the structural integrity of the Tb-compound **(7)** is retained (Figure S29 and S30). The recyclability of the compound (compound was filtered, washed several times with water, and dried) towards the sensing of Cr^{3+} and Fe^{3+} ions was examined, which indicated that the compound retains the same sensing activity for at least 4 cycles (Figure S31).

Magnetic Study:

The magnetic behavior of Gd, Tb and Dy compounds were investigated in the temperature range 2-300 K. The magnetic behavior of the individual compounds were considered based on the dimeric unit of the formula $[Ln_2L_3(H_2O)_4]\cdot 8H_2O$ (Ln=Gd, Tb, Dy).

The temperature dependence of the magnetic susceptibility, χ_M, for the Gd derivative, **6** is plotted as $\chi_M T = f(T)$ in Figure 11. The value for $\chi_M T$ found at 300 K, 15.5 $cm^3mol^{-1}K$, is in good agreement with the Curie contribution expected for two Gd^{3+} spin centers (i.e. 2x 7.88 $cm^3mol^{-1}K$). This value remains unchanged when T is reduced to about 50 K, and at lower temperatures a slight decrease is observed, reaching 11.7 $cm^3mol^{-1}K$ for 2 K. The field dependence of the magnetization (Figure 11b) indicates a saturation magnetization of about 14 μ_B, with no feature in the low field range. These magnetic behaviors are characteristic for two weakly exchange-coupled magnetic centers.[116]

Modeling was performed by considering two interacting Gd(III) centers, - the simultaneous analysis of $\chi_M T = f(T)$ and $M = f(H)$ (red line in Figure 11) gave J = -0.06 cm^{-1} with g = 1.97, (reference Hamiltonian: $\boldsymbol{H} = -J\mathbf{S}_{Gd1}.\mathbf{S}_{Gd2}$) thus confirming the very weak antiferromagnetic Gd-Gd interaction.

For Tb (**7**) and Dy (**8**) derivatives, the values for $\chi_M T$ found at 300 K are respectively 23.3 and 28.2 $cm^3mol^{-1}K$, is in good agreement with that expected for two of these Ln centers (i.e. 23.6 and 28.34 $cm^3mol^{-1}K$).[117 118] Their $\chi_M T = f(T)$ behavior (Figure 11) is characterized by a steady decrease as T is lowered, in agreement with the crystal-field effect applying for these ions and possibly weak antiferromagnetic interactions. Their $M = f(H)$ (Figure S32) are in line with anticipated behaviors and do not provide evidence for antiferromagnetic interactions (i.e. an S-shape $M = f(H)$ behavior).

The possible slow magnetic relaxation for these compounds was probed by AC susceptibility measurements performed in absence and with an applied field. No out-of-phase component, χ_M'', was observed (Figure S32) which rules out any slow relaxation of the magnetization above 2 K.

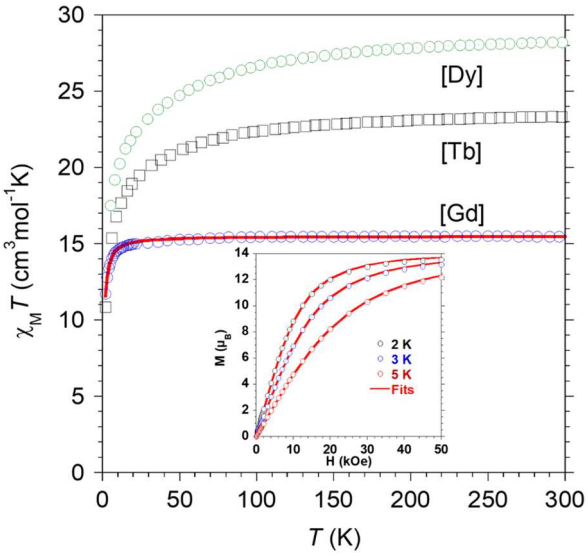

Figure 11. $\chi_M T = f(T)$ behaviors for **6**-**8**, and (inset) $M = f(H)$ behaviors for Gd derivative **6**. The red full-lines are the best-fits modeling. Individual plots are given in Figure S32.

Catalytic Study:

The lanthanide-based metal-organic framework compounds have been explored mainly towards their magnetic and luminescence behaviour.[119–121] Their possible catalytic activity has not been explored actively, though there are reports of employing lanthanide MOFs towards heterogeneous catalysis.[122–125] In the present study, the usefulness of Tb-MOF was examined in the Ullmann type cross coupling between a phenol and a bromobenzene. The O-Arylation (C – O coupling) reaction was investigated in the presence of a number of bases (Table S10),

which indicated that the Cs_2CO_3 was the most effective. The temperature for the catalytic reaction was arrived by carrying out the reactions from room temperature to 80 °C (Table S10). We also made attempts to carry out the reaction in different solvents which suggested that the DMF solvent gives a maximum yield of the product (Table S11). Thus, C–O coupling reaction between phenol (1 mmol) and methyl-4-bromobenzoate (1 mmol) was carried out in presence of 1.5 mmol of Cs_2CO_3 and 2 mL of DMF at 80 °C in the presence of 0.007 mol% of the catalyst (Tb-compound, **7**). The studies indicated that the C–O coupling reaction gave the highest yield of 95% after 5 hr at 80 °C. No increase in the yield was noted by varying the reaction temperature (90 °C) under the same catalytic reaction conditions. The same reaction was also attempted employing the Ce MOF compound (**10**) at 80 °C in the optimized reaction conditions, which gave a yield of 89% (Table S12). We have also carried out the cross-coupling reaction using the neat Tb and Ce nitrate salts, which gave a low yield (Table S12). The catalytic activity of the Tb-MOF was attempted by changing bromoarene derivatives containing both electron-rich as well as electron-poor bromoarenes. In all the cases, we observed the formation of the corresponding phenoxy compounds in good yields in ~5 hours under the optimized reaction conditions (Table 3). The coupling reactions of the electron–deficient phenol and aryl halides has been a challenging one as the corresponding phenolate is a weak nucleophile. The present catalyst Tb MOF appears to be efficient in activating this reaction. Our studies indicated that the presence of an electron-donating group (–Me) in the bromobenzene appears to give a lower yield (58%) (Table 3), which agrees well with those reported before.[81] The electron-withdrawing groups such as –CHO, –NC, –COOMe, $–NO_2$, –Cl, appears to enhance the reactivity giving rise to the expected products with maximum yield (95%). The obtained products in all the cases were purified by column chromatography and ^{1}H-NMR spectra was used for the characterization (Figure S35-S42). ESI-MS for the products of the catalytic reaction are given in Figure S43-S50. The Turn Over Number (TON) of the catalytic reaction has been calculated and the values are given in Table 3.[126–129] The recyclability of the Tb-MOF catalyst was examined under the standardized conditions, which gave yields of 95%, ~89%, and ~87%, respectively (Figure 12).

For recyclability studies, the catalyst was separated by centrifugation and washed several times with fresh DMF and dried at 70 °C in an oven for 2h, which was utilised for the recyclability studies under similar reaction conditions. The stability of the catalyst after the coupling reactions was examined by PXRD (Figure S33), which also indicated that the catalyst retains

the structure. We have also proposed a possible mechanism for the O-Arylation reaction following the earlier reports (Figure S34).

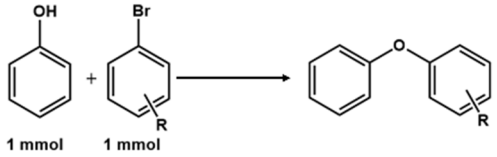

Entry	Reactant	Product	Yield (%)		TON
			With Catalyst	Without Catalyst	
1	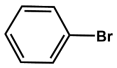	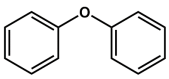	70	21	10000
2	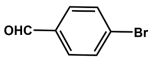	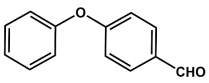	78	29	11142
3	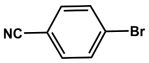	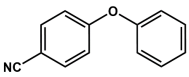	89	41	12714
4	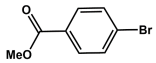	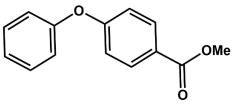	95	47	13571
5	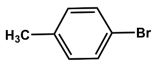	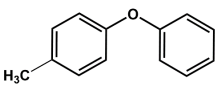	58	9	8285
6	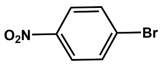	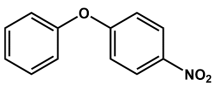	91	43	13000
7[b]	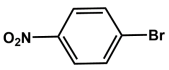	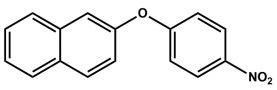	87	38	12428
8	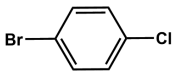	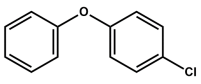	85	37	12142

[a]**Reaction condition**: Bromoarene (1 mmol), Phenol (1 mmol), Cs_2CO_3 (1.5 mmol), catalyst (5 mg, 0.007 mol%), DMF (2 mL) at 80 °C for 5h, yield based on column chromatography

[b]**Reaction condition**: 4-Bromonitrobenzene (1 mmol), β-naphthol (1 mmol), Cs_2CO_3 (1.5 mmol), catalyst (5 mg, 0.007 mol%), DMF (2 mL) at 80 °C for 5h, yield based on column chromatography

Table 3: O-arylation reaction of different aryl alcohols with substituted aryl bromides[a]

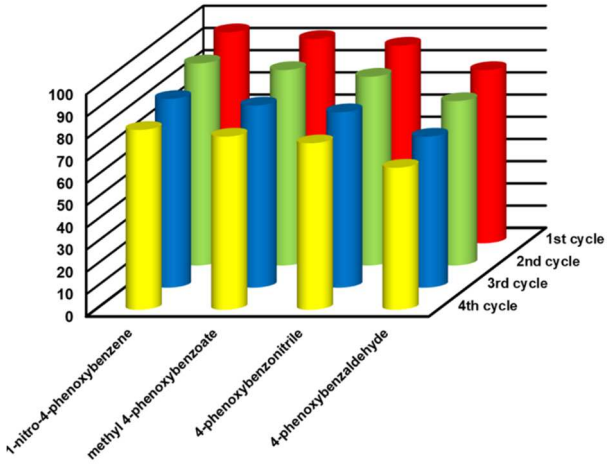

Figure 12: Recyclability studies for the O – Arylation reaction employing Tb-MOF compound.

After 1 h of the reaction, the catalyst was separated from the reaction mixture by centrifugation and the filtrate was allowed to react at 80 °C. The yield of the reaction with and without the Tb MOF catalyst indicated clearly that the in the absence of the catalyst, the reaction does not proceed (Figure 13). It may be noted that, in the absence of Tb MOF, there is no change in the yield of the reaction. The amount of the catalyst in the filtrate was also analysed by ICP-OES analysis, which does not indicate the presence of the catalyst. We have also carried out the reaction by doubling all the reactants in the catalytic study, which indicated similar activity as that of the test study. This suggests that the reactions can be scaled up to meet possible higher demand.

The heterogeneous catalytic nature of the reaction was confirmed by performing the hot filtration experiment. Thus, the mixture of bromobenzene (1.0 mmol), phenol (1.0 mmol), Cs_2CO_3 (1.5 mmol), DMF (2mL), and Tb MOF (5 mg, 0.007 mol %) was reacted at 80 °C.

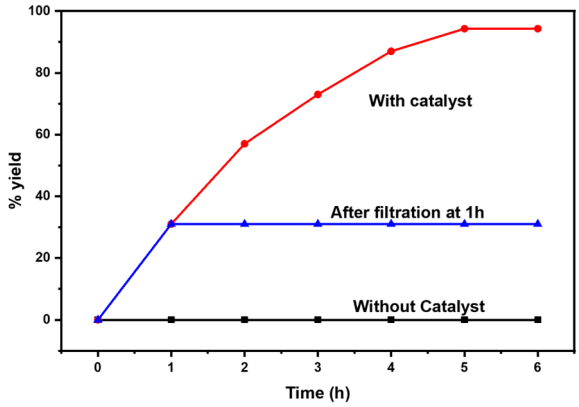

Figure 13. The hot filtration studies during C–O coupling reaction (■ without catalyst, ● With a catalyst, ◀ Yield after removing the catalyst by centrifugation after 1h)

CONCLUSION:

The synthesis of new lanthanide carboxylates with two–and three–dimensional structure has been accomplished. All the structures have face sharing polyhedral dimers of the lanthanide connected by 2, 5–BPTA ligand. The Pr-compound stabilises both in the 2D as well as 3D structure, the formation depends on the time of reaction. Photoluminescence studies indicate that the ligand emits in the blue region and transfer efficiently to the rare–earth ions giving characteristic emissions. The compound, ($Y_{0.96}Tb_{0.02}Eu_{0.02}$) MOF, gives rise to intense white light emission with a quantum yield of 28%. Of the rare earth ions investigated, the Tb^{3+} containing compound gives the largest quantum yield of 85%. The Tb – MOF was found to be a good and selective sensor for Cr^{3+} and Fe^{3+} ions in aqueous solution with high sensitivity. The Ullman type catalytic reaction between phenol and aryl halides in the presence of Tb – MOF gives excellent O – arylation product with 95% yield. The magnetic studies on Gd, Tb and Dy containing compounds indicated weak exchange interactions in the dimeric units and no slow magnetic relaxation features were observed for these compounds.

ASSOCIATED CONTENT:

Supporting Information:

Elemental analysis of all the MOFs (Table S1), the selected bond angles, bond distances, and hydrogen bonding interactions of all the MOFs (**1-11**) (Tables S2-S5), lists of UV-Vis Optical transitions and IR band (Tables S6, S7), CIE chromaticity coordinates for $Y_{0,98-x}Tb_{0.02}Eu_x$– MOF material (Table S8), LOD calculation for Fe^{3+} and Cr^{3+} sensing (Table S9), O – Arylation reaction Temperature, solvent, and catalyst optimization (Tables S10-S12), Experimental and simulated PXRD pattern for all the MOFs and structural integrity of $Y_{0.98-x\%}Tb_{0.02}Eu_{x\%}$– MOF (Figures S1, S2), SEM and EDX analysis for of $Y_{0.98-x\%}Tb_{0.02}Eu_{x\%}$– MOF (Figure S3), UV–Vis absorption and Infra-red spectra (Figures S4, S5), TGA analysis of the 2D and 3D compounds and PXRD after TGA (Figures S6-S8), Asymmetric unit and various coordination mode of linker in MOFs (Figures S9, S12), Metal coordination of Y and La in the MOF compound (Figure S10), Water molecule interaction in 2D MOFs (Figure S11), Simplified structure of 3D La MOF (Figure S13), Room-temperature photoluminescence spectra (Figure S14), Luminescence decay profiles for Y, Eu and Tb MOFs (Figure S15), PL spectra of different substitution of Eu^{3+} and Tb^{3+} in Y-MOF and corresponding CIE diagram (Figures S16, S17), Spectral overlap between the PLE spectrum of Y-MOF: Eu^{3+} and PL spectrum of Y-MOF:

Tb^{3+} materials (Figure S18), luminescence excitation and emission spectrum of Y-MOF, 2% Tb^{3+}, 4% Eu^{3+} sample (Figure S19), PL emission spectra (λ_{ex} = 340 nm) of 2,5 BPTA + 2% Tb^{3+} + x% Eu^{3+} and Physical mixing of Y MOF, 2% Tb MOF and 2% Eu MOF (Figures S20, S21), Tb-MOF intensity in presence of different cations (Figure S22), Comparison of the luminescence quenching effect (Figure S23), Stern-Volmer plots for Tb MOF at high concentration of $Cr^{3+}$and Fe^{3+} (Figure S24), The graph for the LOD calculation (Figure S25), The absorption bands of analytes along with the emission spectra of Tb MOF (Figure S26), Schematic of various energy/electron transfer processes in the sensing studies using the Tb MOF (Figure S27), IR titration of compound **7** upon the gradual addition of metal ions (Figure S28), PXRD, SEM study on the samples after the sensing (Figures S29, S30), Recyclability study in sensing (Figure S31), Magnetic Susceptibility of Gd, Tb and Dy MOFs (Figure S32), PXRD pattern of catalyst in O – Arylation reaction during recyclability studies (Figure S33), Mechanism and procedure of O – Arylation reaction (Figure S34), ^{1}H NMR and ESI-MS spectra of all catalytic O – Arylation products (Figure S35 – S50). (PDF)

Accession Codes: Accession Codes CCDC 2184686-2184693 and 2184743-2184745 contain the supplementary crystallographic data for this article. These data can be obtained free of charge via www.ccdc.cam.ac.uk/ data_request/cif, or by emailing data_request@ccdc.cam.ac.uk, or by contacting The Cambridge Crystallographic Data Centre, 12 Union Road, Cambridge CB2 1EZ, UK; fax: + 44 1223 336033.

AUTHOR INFORMATION:

Corresponding Authors:

Srinivasan Natarajan – *Frameworks Solids Laboratory, Solid State and Structural Chemistry Unit, Indian Institute of Science, Bangalore 560012, India*; https://orcid.org/0000-0002-4942-0968**,** E-mail: snatarajan@iisc.ac.in

Jean-Pascal Sutter – *Laboratoire de Chimie de Coordination du CNRS, Université de Toulouse, CNRS, 205 route de Narbonne, 31077 Toulouse (France)*

https://orcid.org/0000-0003-4960-0579

E-mail : jean-pascal.sutter@lcc-toulouse.fr

Author:

Krishna Manna – *Frameworks Solids Laboratory, Solid State and Structural Chemistry Unit, Indian Institute of Science, Bangalore 560012, India*

ACKNOWLEDGEMENTS:

SN thanks to Science and Engineering research Board, (SERB) Govt. of India for the award of JC Bose national fellowship. SN and KM thanks CSIR, Government of India, for the award of a research grant and research fellowship. We are thankful to Prof. P. Thilagar and Mr. Tanmay Kumar Sarkar of the Inorganic and Physical Chemistry Department, Indian Institute of Science for the lifetime and quantum yield measurements.

REFERENCES:

(1) Long, J. R.; Yaghi, O. M. The Pervasive Chemistry of Metal–Organic Frameworks. *Chem Soc Rev* **2009**, *38* (5), 1213–1214. https://doi.org/10.1039/B903811F.

(2) Introduction to Metal–Organic Frameworks. *Chem Rev* **2012**, *112* (2), 673–674. https://doi.org/10.1021/cr300014x.

(3) Natarajan, S.; Mahata, P. Metal–Organic Framework Structures – How Closely Are They Related to Classical Inorganic Structures? *Chem Soc Rev* **2009**, *38* (8), 2304–2318. https://doi.org/10.1039/B815106G.

(4) Li, B.; Wen, H.-M.; Zhou, W.; Chen, B. Porous Metal–Organic Frameworks for Gas Storage and Separation: What, How, and Why? *J Phys Chem Lett* **2014**, *5* (20), 3468–3479. https://doi.org/10.1021/jz501586e.

(5) Lei, B.; Wang, M.; Jiang, Z.; Qi, W.; Su, R.; He, Z. Constructing Redox-Responsive Metal–Organic Framework Nanocarriers for Anticancer Drug Delivery. *ACS Appl Mater Interfaces* **2018**, *10* (19), 16698–16706. https://doi.org/10.1021/acsami.7b19693.

(6) Qiao, J.; Zhang, B.; Yu, X.; Zou, X.; Liu, X.; Zhang, L.; Liu, Y. A Stable Y(III)-Based Amide-Functionalized Metal–Organic Framework for Propane/Methane Separation and Knoevenagel Condensation. *Inorg Chem* **2022**, *61* (8), 3708–3715. https://doi.org/10.1021/acs.inorgchem.1c03924.

(7) Mandal, S.; Natarajan, S.; Mani, P.; Pankajakshan, A. Post-Synthetic Modification of Metal–Organic Frameworks Toward Applications. *Adv Funct Mater* **2021**, *31* (4), 2006291. https://doi.org/https://doi.org/10.1002/adfm.202006291.

(8) Habib, N. R.; Asedegbega-Nieto, E.; Taddesse, A. M.; Diaz, I. Non-Noble MNP@MOF Materials: Synthesis and Applications in Heterogeneous Catalysis. *Dalton Transactions* **2021**, *50* (30), 10340–10353. https://doi.org/10.1039/D1DT01531A.

(9) Manna, K.; Suresh Kumar, B.; Maity, T.; Natarajan, S. C−C Coupling of Aryl Chlorides and Reduction of Nitroarenes to Amines Employing Recyclable Heterogeneous Green Catalysts. *ChemNanoMat* **2022**, *8* (6), e202200081. https://doi.org/https://doi.org/10.1002/cnma.202200081.

(10) Singha, D. K.; Bhattacharya, S.; Majee, P.; Mondal, S. K.; Kumar, M.; Mahata, P. Optical Detection of Submicromolar Levels of Nitro Explosives by a Submicron Sized Metal–Organic Phosphor Material. *J Mater Chem A Mater* **2014**, *2* (48), 20908–20915. https://doi.org/10.1039/C4TA05014B.

(11) Kundu, T.; Manna, K.; Jana, A. K.; Natarajan, S. A Luminescent Inorganic–Organic Hybrid, [Cd(C16H10N2O8S)(H2O)], for the Selective and Recyclable Detection of Chromates and Dichromates in Aqueous Solution. *New Journal of Chemistry* **2019**, *43* (33), 13263–13270. https://doi.org/10.1039/C9NJ03224J.

(12) Akhtar, M. N.; Chen, Y.-C.; AlDamen, M. A.; Tong, M.-L. 3D Oxalato-Bridged Lanthanide(Iii) MOFs with Magnetocaloric, Magnetic and Photoluminescence Properties. *Dalton Transactions* **2017**, *46* (1), 116–124. https://doi.org/10.1039/C6DT03843C.

(13) Zhang, C.; Ma, X.; Cen, P.; Jin, X.; Yang, J.; Zhang, Y.-Q.; Ferrando-Soria, J.; Pardo, E.; Liu, X. A Series of Lanthanide(Iii) Metal–Organic Frameworks Derived from a Pyridyl-Dicarboxylate Ligand: Single-Molecule Magnet Behaviour and Luminescence Properties. *Dalton Transactions* **2020**, *49* (40), 14123–14132. https://doi.org/10.1039/D0DT02736G.

(14) Wu, M.-X.; Yang, Y.-W. Metal–Organic Framework (MOF)-Based Drug/Cargo Delivery and Cancer Therapy. *Advanced Materials* **2017**, *29* (23), 1606134. https://doi.org/https://doi.org/10.1002/adma.201606134.

(15) Suresh, K.; Matzger, A. J. Enhanced Drug Delivery by Dissolution of Amorphous Drug Encapsulated in a Water Unstable Metal–Organic Framework (MOF). *Angewandte Chemie International Edition* **2019**, *58* (47), 16790–16794. https://doi.org/https://doi.org/10.1002/anie.201907652.

(16) Mahata, P.; Natarajan, S. A New Series of Three-Dimensional Metal−Organic Framework, [M2(H2O)][C5N1H3(COO)2]3·2H2O, M = La, Pr, and Nd: Synthesis, Structure, and Properties. *Inorg Chem* **2007**, *46* (4), 1250–1258. https://doi.org/10.1021/ic0617644.

(17) Sushrutha, S. R.; Hota, R.; Natarajan, S. Adenine-Based Coordination Polymers: Synthesis, Structure, and Properties. *Eur J Inorg Chem* **2016**, *2016* (18), 2962–2974. https://doi.org/https://doi.org/10.1002/ejic.201600111.

(18) Hu, J.-J.; Peng, Y.; Liu, S.-J.; Wen, H.-R. Recent Advances in Lanthanide Coordination Polymers and Clusters with Magnetocaloric Effect or Single-Molecule Magnet Behavior. *Dalton Transactions* **2021**, *50* (43), 15473–15487. https://doi.org/10.1039/D1DT02797B.

(19) Bernot, K.; Daiguebonne, C.; Calvez, G.; Suffren, Y.; Guillou, O. A Journey in Lanthanide Coordination Chemistry: From Evaporable Dimers to Magnetic Materials and Luminescent Devices. *Acc Chem Res* **2021**, *54* (2), 427–440. https://doi.org/10.1021/acs.accounts.0c00684.

(20) Theppitak, C.; Kielar, F.; Dungkaew, W.; Sukwattanasinitt, M.; Kangkaew, L.; Sahasithiwat, S.; Zenno, H.; Hayami, S.; Chainok, K. The Coordination Chemistry of Benzhydrazide with Lanthanide(Iii) Ions: Hydrothermal in Situ Ligand Formation, Structures, Magnetic and Photoluminescence Sensing Properties. *RSC Adv* **2021**, *11* (40), 24709–24721. https://doi.org/10.1039/D1RA03106F.

(21) Driscoll, D. M.; Shiery, R. C.; Balasubramanian, M.; Fulton, J. L.; Cantu, D. C. Ionic Contraction across the Lanthanide Series Decreases the Temperature-Induced Disorder of the Water Coordination Sphere. *Inorg Chem* **2022**, *61* (1), 287–294. https://doi.org/10.1021/acs.inorgchem.1c02837.

(22) Jiao, Y.; Sarwar, S.; Sanz, S.; van Leusen, J.; Izarova, N. v; Campbell, C. L.; Brechin, E. K.; Dalgarno, S. J.; Kögerler, P. Exploiting Complementary Ligands for the Construction of Square Antiprismatic Monometallic Lanthanide SMMs. *Dalton Transactions* **2021**, *50* (27), 9648–9654. https://doi.org/10.1039/D1DT00359C.

(23) Han, Y.-H.; Tian, C.-B.; Li, Q.-H.; Du, S.-W. Highly Chemical and Thermally Stable Luminescent EuxTb1−x MOF Materials for Broad-Range PH and Temperature Sensors. *J Mater Chem C Mater* **2014**, *2* (38), 8065–8070. https://doi.org/10.1039/C4TC01336K.

(24) White, K. A.; Chengelis, D. A.; Gogick, K. A.; Stehman, J.; Rosi, N. L.; Petoud, S. Near-Infrared Luminescent Lanthanide MOF Barcodes. *J Am Chem Soc* **2009**, *131* (50), 18069–18071. https://doi.org/10.1021/ja907885m.

(25) Hao, Z.; Yang, G.; Song, X.; Zhu, M.; Meng, X.; Zhao, S.; Song, S.; Zhang, H. A Europium(Iii) Based Metal–Organic Framework: Bifunctional Properties Related to Sensing and Electronic Conductivity. *J Mater Chem A Mater* **2014**, *2* (1), 237–244. https://doi.org/10.1039/C3TA13179C.

(26) Beltrán-Leiva, M. J.; Solis-Céspedes, E.; Páez-Hernández, D. The Role of the Excited State Dynamic of the Antenna Ligand in the Lanthanide Sensitization Mechanism. *Dalton Transactions* **2020**, *49* (22), 7444–7450. https://doi.org/10.1039/D0DT01132K.

(27) Uh, H.; Petoud, S. Novel Antennae for the Sensitization of near Infrared Luminescent Lanthanide Cations. *Comptes Rendus Chimie* **2010**, *13* (6), 668–680. https://doi.org/https://doi.org/10.1016/j.crci.2010.05.007.

(28) Ramya, A. R.; Sharma, D.; Natarajan, S.; Reddy, M. L. P. Highly Luminescent and Thermally Stable Lanthanide Coordination Polymers Designed from 4-(Dipyridin-2-Yl)Aminobenzoate: Efficient Energy Transfer from Tb3+ to Eu3+ in a Mixed Lanthanide Coordination Compound. *Inorg Chem* **2012**, *51* (16), 8818–8826. https://doi.org/10.1021/ic300654e.

(29) Sarma, D.; Prabu, M.; Biju, S.; Reddy, M. L. P.; Natarajan, S. Synthesis, Structure and Optical Studies of a Family of Three-Dimensional Rare-Earth Aminoisophthalates [M(M2-OH)(C8H5NO4)] (M = Y3+, La3+, Pr3+, Nd3+, Sm3+, Eu3+, Gd3+, Dy3+, and Er3+). *Eur J Inorg Chem* **2010**, *2010* (24), 3813–3822. https://doi.org/https://doi.org/10.1002/ejic.201000225.

(30) Xu, L.-J.; Xu, G.-T.; Chen, Z.-N. Recent Advances in Lanthanide Luminescence with Metal-Organic Chromophores as Sensitizers. *Coord Chem Rev* **2014**, *273–274*, 47–62. https://doi.org/https://doi.org/10.1016/j.ccr.2013.11.021.

(31) Zhang, B.; Zhang, J.; Guo, Y.; Wang, J.; Xie, J.; Li, X.; Huang, W.; Wang, L.; Zhang, Q. Synthesis and Photoluminescence of Double Perovskite La2LiSbO6:Ln3+ (Ln= Eu, Tb, Tm, Sm, Ho) Phosphors and Enhanced Luminescence of La2LiSbO6:Eu3+ Red Phosphor via Bi3+ Doping for White Light Emitting Diodes. *J Alloys Compd* **2019**, *787*, 1163–1172. https://doi.org/https://doi.org/10.1016/j.jallcom.2019.02.132.

(32) Zhang, Y.; Gong, W.; Yu, J.; Lin, Y.; Ning, G. Tunable White-Light Emission via Energy Transfer in Single-Phase LiGd(WO4)2:Re3+ (Re = Tm, Tb, Dy, Eu) Phosphors for UV-Excited WLEDs. *RSC Adv* **2015**, *5* (117), 96272–96280. https://doi.org/10.1039/C5RA19345A.

(33) Zhang, D.; Xue, Z.-Z.; Pan, J.; Shang, M.-M.; Mu, Y.; Han, S.-D.; Wang, G.-M. Solvated Lanthanide Cationic Template Strategy for Constructing Iodoargentates with Photoluminescence and White Light Emission. *Cryst Growth Des* **2018**, *18* (11), 7041–7047. https://doi.org/10.1021/acs.cgd.8b01207.

(34) Fred, S. E.; Kyu, K. J. Solid-State Light Sources Getting Smart. *Science (1979)* **2005**, *308* (5726), 1274–1278. https://doi.org/10.1126/science.1108712.

(35) Ma, M.-L.; Ji, C.; Zang, S.-Q. Syntheses, Structures, Tunable Emission and White Light Emitting Eu3+ and Tb3+ Doped Lanthanide Metal–Organic Framework Materials. *Dalton Transactions* **2013**, *42* (29), 10579–10586. https://doi.org/10.1039/C3DT50315A.

(36) Carlos, L. D.; Ferreira, R. A. S.; de Zea Bermudez, V.; Julián-López, B.; Escribano, P. Progress on Lanthanide-Based Organic–Inorganic Hybrid Phosphors. *Chem Soc Rev* **2011**, *40* (2), 536–549. https://doi.org/10.1039/C0CS00069H.

(37) Yang, Q.-Y.; Wu, K.; Jiang, J.-J.; Hsu, C.-W.; Pan, M.; Lehn, J.-M.; Su, C.-Y. Pure White-Light and Yellow-to-Blue Emission Tuning in Single Crystals of Dy(Iii) Metal–Organic Frameworks. *Chemical Communications* **2014**, *50* (57), 7702–7704. https://doi.org/10.1039/C4CC01763C.

(38) Wei, Y.; Li, Q.; Sa, R.; Wu, K. A White-Light-Emitting LnMOF with Color Properties Improved via Eu3+ Doping: An Alternative Approach to a Rational Design for Solid-State Lighting. *Chemical Communications* **2014**, *50* (15), 1820–1823. https://doi.org/10.1039/C3CC48344D.

(39) Lee, Y.-C.; Chen, H.-L.; Lu, C.-Y.; Wu, H.-S.; Chou, Y.-F.; Chen, S.-H. Using Nanoimprint Lithography to Improve the Light Extraction Efficiency and Color Rendering of Dichromatic White Light-Emitting Diodes. *Nanoscale* **2015**, *7* (39), 16312–16320. https://doi.org/10.1039/C5NR02988K.

(40) Peña-Rodríguez, R.; Molina-González, J. A.; Desirena-Enrriquez, H.; Armenta-Jaime, E.; Rivera, J. M.; Castillo-Blum, S. E. Doping of a Zn-MOF with Eu3+ and Tb3+ for Application in the Manufacture of a WLED. *J Mater Chem C Mater* **2021**, *9* (44), 15891–15899. https://doi.org/10.1039/D1TC03454E.

(41) Haldar, S.; Chakraborty, D.; Roy, B.; Banappanavar, G.; Rinku, K.; Mullangi, D.; Hazra, P.; Kabra, D.; Vaidhyanathan, R. Anthracene-Resorcinol Derived Covalent Organic Framework as Flexible White Light Emitter. *J Am Chem Soc* **2018**, *140* (41), 13367–13374. https://doi.org/10.1021/jacs.8b08312.

(42) Chen, P.; Li, Q.; Grindy, S.; Holten-Andersen, N. White-Light-Emitting Lanthanide Metallogels with Tunable Luminescence and Reversible Stimuli-Responsive Properties. *J Am Chem Soc* **2015**, *137* (36), 11590–11593. https://doi.org/10.1021/jacs.5b07394.

(43) Strukelj, M.; Jordan, R. H.; Dodabalapur, A. Organic Multilayer White Light Emitting Diodes. *J Am Chem Soc* **1996**, *118* (5), 1213–1214. https://doi.org/10.1021/ja953302n.

(44) Praveen, V. K.; Ranjith, C.; Armaroli, N. White-Light-Emitting Supramolecular Gels. *Angewandte Chemie International Edition* **2014**, *53* (2), 365–368. https://doi.org/https://doi.org/10.1002/anie.201306787.

(45) Xu, Y.-Y.; Chen, P.; Gao, T.; Li, H.-F.; Yan, P.-F. White-Light Emission Based on a Single Component Sm(Iii) Complex and Enhanced Optical Properties by Doping Methods. *CrystEngComm* **2019**, *21* (6), 964–970. https://doi.org/10.1039/C8CE01919C.

(46) Bhim, A.; Mohanty, A.; Natarajan, S. Tuning the Langasite, La3SbZn3Si2O14, towards White Light Emission: Synthesis, Structure, SHG and Photoluminescence Studies. *Dalton Transactions* **2020**, *49* (48), 17649–17657. https://doi.org/10.1039/D0DT03450A.

(47) Sheu, J.-K.; Chen, F.-B.; Wang, Y.-C.; Chang, C.-C.; Huang, S.-H.; Liu, C.-N.; Lee, M.-L. Warm-White Light-Emitting Diode with High Color Rendering Index Fabricated by Combining Trichromatic InGaN Emitter with Single Red Phosphor. *Opt Express* **2015**, *23* (7), A232–A239. https://doi.org/10.1364/OE.23.00A232.

(48) Ma, M.-L.; Ji, C.; Zang, S.-Q. Syntheses, Structures, Tunable Emission and White Light Emitting Eu3+ and Tb3+ Doped Lanthanide Metal–Organic Framework Materials. *Dalton Transactions* **2013**, *42* (29), 10579–10586. https://doi.org/10.1039/C3DT50315A.

(49) Xu, L.; Xu, Y.; Li, X.; Wang, Z.; Sun, T.; Zhang, X. Eu3+/Tb3+ Functionalized Bi-Based Metal–Organic Frameworks toward Tunable White-Light Emission and Fluorescence Sensing Applications. *Dalton Transactions* **2018**, *47* (46), 16696–16703. https://doi.org/10.1039/C8DT03474E.

(50) Rao, X.; Huang, Q.; Yang, X.; Cui, Y.; Yang, Y.; Wu, C.; Chen, B.; Qian, G. Color Tunable and White Light Emitting Tb3+ and Eu3+ Doped Lanthanide Metal–Organic Framework Materials. *J Mater Chem* **2012**, *22* (7), 3210–3214. https://doi.org/10.1039/C2JM14127B.

(51) Tajik, S.; Beitollahi, H.; Garkani Nejad, F.; Sheikhshoaie, I.; Nugraha, A. S.; Jang, H. W.; Yamauchi, Y.; Shokouhimehr, M. Performance of Metal–Organic Frameworks in the Electrochemical Sensing of Environmental Pollutants. *J Mater Chem A Mater* **2021**, *9* (13), 8195–8220. https://doi.org/10.1039/D0TA08344E.

(52) Li, Y.-W.; Li, J.; Wan, X.-Y.; Sheng, D.-F.; Yan, H.; Zhang, S.-S.; Ma, H.-Y.; Wang, S.-N.; Li, D.-C.; Gao, Z.-Y.; Dou, J.-M.; Sun, D. Nanocage-Based N-Rich Metal–Organic Framework for Luminescence Sensing toward Fe3+ and Cu2+ Ions. *Inorg Chem* **2021**, *60* (2), 671–681. https://doi.org/10.1021/acs.inorgchem.0c02629.

(53) Chand, S.; Verma, G.; Pal, A.; Pal, S. C.; Ma, S.; Das, M. C. Porous Anionic Co(II) Metal-Organic Framework, with a High Density of Amino Groups, as a Superior Luminescent Sensor for Turn-on Al(III) Detection. *Chemistry – A European Journal* **2021**, *27* (46), 11804–11810. https://doi.org/https://doi.org/10.1002/chem.202101692.

(54) Fajal, S.; Mandal, W.; Majumder, D.; Shirolkar, M. M.; More, Y. D.; Ghosh, S. K. Unfolding the Role of Building Units of MOFs with Mechanistic Insight Towards Selective Metal Ions Detection in Water**. *Chemistry – A European Journal* **2022**, *28* (21), e202104175. https://doi.org/https://doi.org/10.1002/chem.202104175.

(55) Yan, W.; Zhang, C.; Chen, S.; Han, L.; Zheng, H. Two Lanthanide Metal–Organic Frameworks as Remarkably Selective and Sensitive Bifunctional Luminescence Sensor for Metal Ions and Small Organic Molecules. *ACS Appl Mater Interfaces* **2017**, *9* (2), 1629–1634. https://doi.org/10.1021/acsami.6b14563.

(56) Singh, I. B.; Singh, D. R. Cr(VI) Removal in Acidic Aqueous Solution Using Iron-Bearing Industrial Solid Wastes and Their Stabilisation with Cement. *Environ Technol* **2002**, *23* (1), 85–95. https://doi.org/10.1080/09593332508618436.

(57) Zhitkovich, A. Chromium in Drinking Water: Sources, Metabolism, and Cancer Risks. *Chem Res Toxicol* **2011**, *24* (10), 1617–1629. https://doi.org/10.1021/tx200251t.

(58) Zongo, I.; Leclerc, J.-P.; Maïga, H. A.; Wéthé, J.; Lapicque, F. Removal of Hexavalent Chromium from Industrial Wastewater by Electrocoagulation: A Comprehensive Comparison of Aluminium and Iron Electrodes. *Sep Purif Technol* **2009**, *66* (1), 159–166. https://doi.org/https://doi.org/10.1016/j.seppur.2008.11.012.

(59) Razavi, S. A. A.; Masoomi, M. Y.; Morsali, A. Ultrasonic Assisted Synthesis of a Tetrazine Functionalized MOF and Its Application in Colorimetric Detection of Phenylhydrazine. *Ultrason Sonochem* **2017**, *37*, 502–508. https://doi.org/https://doi.org/10.1016/j.ultsonch.2017.02.011.

(60) Rodriguez-Proteau, R.; Grant, R. L. Toxicity Evaluation and Human Health Risk Assessment of Surface and Ground Water Contaminated by Recycled Hazardous Waste Materials. In *Water Pollution: Environmental Impact Assessment of Recycled Wastes on Surface and Ground Waters; Risk Analysis*; Kassim, T. A., Ed.; Springer Berlin Heidelberg: Berlin, Heidelberg, 2005; pp 133–189. https://doi.org/10.1007/b11434.

(61) Hao, J.-N.; Yan, B. Amino-Decorated Lanthanide(Iii) Organic Extended Frameworks for Multi-Color Luminescence and Fluorescence Sensing. *J Mater Chem C Mater* **2014**, *2* (33), 6758–6764. https://doi.org/10.1039/C4TC00962B.

(62) Huang, W.; Pan, F.; Liu, Y.; Huang, S.; Li, Y.; Yong, J.; Li, Y.; Kirillov, A. M.; Wu, D. An Efficient Blue-Emissive Metal–Organic Framework (MOF) for Lanthanide-Encapsulated Multicolor and Stimuli-Responsive Luminescence. *Inorg Chem* **2017**, *56* (11), 6362–6370. https://doi.org/10.1021/acs.inorgchem.7b00457.

(63) Xu, H.; Dong, Y.; Wu, Y.; Ren, W.; Zhao, T.; Wang, S.; Gao, J. An -OH Group Functionalized MOF for Ratiometric Fe3+ Sensing. *J Solid State Chem* **2018**, *258*, 441–446. https://doi.org/https://doi.org/10.1016/j.jssc.2017.11.013.

(64) Hao, Z.; Song, X.; Zhu, M.; Meng, X.; Zhao, S.; Su, S.; Yang, W.; Song, S.; Zhang, H. One-Dimensional Channel-Structured Eu-MOF for Sensing Small Organic Molecules and Cu2+ Ion. *J Mater Chem A Mater* **2013**, *1* (36), 11043–11050. https://doi.org/10.1039/C3TA12270K.

(65) Ge, K.-M.; Wang, D.; Xu, Z.-J.; Chu, R.-Q. A Luminescent Eu(III)-MOF for Selective Sensing of Ag+ in Aqueous Solution. *J Mol Struct* **2020**, *1208*, 127862. https://doi.org/https://doi.org/10.1016/j.molstruc.2020.127862.

(66) Cui, Z.; Zhang, X.; Liu, S.; Zhou, L.; Li, W.; Zhang, J. Anionic Lanthanide Metal–Organic Frameworks: Selective Separation of Cationic Dyes, Solvatochromic Behavior, and Luminescent Sensing of Co(II) Ion. *Inorg Chem* **2018**, *57* (18), 11463–11473. https://doi.org/10.1021/acs.inorgchem.8b01319.

(67) Du, T.; Wang, J.; Zhang, L.; Wang, S.; Yang, C.; Xie, L.; Liu, Z.; Ni, Y.; Xie, X.; Sun, J.; Zhang, W.; Wang, J. Missing-Linker Engineering of Eu (III)-Doped UiO-MOF for Enhanced Detection of

Heavy Metal Ions. *Chemical Engineering Journal* **2022**, *431*, 134050. https://doi.org/https://doi.org/10.1016/j.cej.2021.134050.

(68) Trickett, C. A.; Osborn Popp, T. M.; Su, J.; Yan, C.; Weisberg, J.; Huq, A.; Urban, P.; Jiang, J.; Kalmutzki, M. J.; Liu, Q.; Baek, J.; Head-Gordon, M. P.; Somorjai, G. A.; Reimer, J. A.; Yaghi, O. M. Identification of the Strong Brønsted Acid Site in a Metal–Organic Framework Solid Acid Catalyst. *Nat Chem* **2019**, *11* (2), 170–176. https://doi.org/10.1038/s41557-018-0171-z.

(69) Zhou, Y.-H.; Zhang, Z.; Patrick, M.; Yang, F.; Wei, R.; Cheng, Y.; Gu, J. Cleaving DNA-Model Phosphodiester with Lewis Acid–Base Catalytic Sites in Bifunctional Zr–MOFs. *Dalton Transactions* **2019**, *48* (23), 8044–8048. https://doi.org/10.1039/C9DT00246D.

(70) Vermoortele, F.; Vandichel, M.; Van de Voorde, B.; Ameloot, R.; Waroquier, M.; Van Speybroeck, V.; De Vos, D. E. Electronic Effects of Linker Substitution on Lewis Acid Catalysis with Metal–Organic Frameworks. *Angewandte Chemie International Edition* **2012**, *51* (20), 4887–4890. https://doi.org/https://doi.org/10.1002/anie.201108565.

(71) Hall, J. N.; Bollini, P. Metal–Organic Framework MIL-100 Catalyzed Acetalization of Benzaldehyde with Methanol: Lewis or Brønsted Acid Catalysis? *ACS Catal* **2020**, *10* (6), 3750–3763. https://doi.org/10.1021/acscatal.0c00399.

(72) Yadav, A.; Kanoo, P. Metal-Organic Frameworks as Platform for Lewis-Acid-Catalyzed Organic Transformations. *Chem Asian J* **2019**, *14* (20), 3531–3551. https://doi.org/https://doi.org/10.1002/asia.201900876.

(73) Li, X.; Huang, L.; Kochubei, A.; Huang, J.; Shen, W.; Xu, H.; Li, Q. Evolution of a Metal-Organic Framework into a Brønsted Acid Catalyst for Glycerol Dehydration to Acrolein. *ChemSusChem* **2020**, *13* (18), 5073–5079. https://doi.org/https://doi.org/10.1002/cssc.202001377.

(74) Beletskaya, I. P.; Cheprakov, A. v. Copper in Cross-Coupling Reactions: The Post-Ullmann Chemistry. *Coord Chem Rev* **2004**, *248* (21), 2337–2364. https://doi.org/https://doi.org/10.1016/j.ccr.2004.09.014.

(75) Ullmann, F. Ueber Eine Neue Darstellungsweise von Phenyläthersalicylsäure. *Berichte der deutschen chemischen Gesellschaft* **1904**, *37* (1), 853–854. https://doi.org/https://doi.org/10.1002/cber.190403701141.

(76) Tye, J. W.; Weng, Z.; Giri, R.; Hartwig, J. F. Copper(I) Phenoxide Complexes in the Etherification of Aryl Halides. *Angewandte Chemie International Edition* **2010**, *49* (12), 2185–2189. https://doi.org/https://doi.org/10.1002/anie.200902245.

(77) Platon, M.; Cui, L.; Mom, S.; Richard, P.; Saeys, M.; Hierso, J.-C. Etherification of Functionalized Phenols with Chloroheteroarenes at Low Palladium Loading: Theoretical Assessment of the Role of Triphosphane Ligands in C□O Reductive Elimination. *Adv Synth Catal* **2011**, *353* (18), 3403–3414. https://doi.org/https://doi.org/10.1002/adsc.201100481.

(78) Aranyos, A.; Old, D. W.; Kiyomori, A.; Wolfe, J. P.; Sadighi, J. P.; Buchwald, S. L. Novel Electron-Rich Bulky Phosphine Ligands Facilitate the Palladium-Catalyzed Preparation of Diaryl Ethers. *J Am Chem Soc* **1999**, *121* (18), 4369–4378. https://doi.org/10.1021/ja990324r.

(79) Wolfe, J. P.; Wagaw, S.; Marcoux, J.-F.; Buchwald, S. L. Rational Development of Practical Catalysts for Aromatic Carbon−Nitrogen Bond Formation. *Acc Chem Res* **1998**, *31* (12), 805–818. https://doi.org/10.1021/ar9600650.

(80) Dorel, R.; Grugel, C. P.; Haydl, A. M. The Buchwald–Hartwig Amination After 25 Years. *Angewandte Chemie International Edition* **2019**, *58* (48), 17118–17129. https://doi.org/https://doi.org/10.1002/anie.201904795.

(81) Maity, T.; Saha, D.; Bhunia, S.; Brandão, P.; Das, S.; Koner, S. A Family of Ligand and Anion Dependent Structurally Diverse Cu(Ii) Schiff-Base Complexes and Their Catalytic Efficacy in an O-Arylation Reaction in Ethanolic Media. *RSC Adv* **2015**, *5* (100), 82179–82191. https://doi.org/10.1039/C5RA14758A.

(82) Dhakshinamoorthy, A.; Asiri, A. M.; Garcia, H. Catalysis by Metal–Organic Frameworks in Water. *Chemical Communications* **2014**, *50* (85), 12800–12814. https://doi.org/10.1039/C4CC04387A.

(83) Esrafili, L.; Morsali, A.; Dehghani Firuzabadi, F.; Retailleau, P. Development of Porous Cobalt-/Copper-Doped Carbon Nanohybrids Derived from Functionalized MOFs as Efficient Catalysts for the Ullmann Cross-Coupling Reaction: Insights into the Active Centers. *ACS Appl Mater Interfaces* **2020**, *12* (38), 43115–43124. https://doi.org/10.1021/acsami.0c09912.

(84) Schneemann, A.; Bloch, E. D.; Henke, S.; Llewellyn, P. L.; Long, J. R.; Fischer, R. A. Influence of Solvent-Like Sidechains on the Adsorption of Light Hydrocarbons in Metal–Organic Frameworks. *Chemistry – A European Journal* **2015**, *21* (51), 18764–18769. https://doi.org/https://doi.org/10.1002/chem.201503685.

(85) Bruker, A. P. E. X. , 2007. 2, S. X. B. A. Inc. ,. Madison, Wisconsin, USA. **2007**.

(86) Bruker, S. B. A. Inc. Bruker, SADABS, Bruker AXS Inc. *Madison, Wisconsin, USA* **2001**.

(87) Sheldrick, 3.3.G., SHELXL-97. Program for Crystal-Structure Refinement. **1997**.

(88) Spek, A. L. *Acta Cryst* **2015**, *C71*, 9–18.

(89) Wang, Z.; Quan, Z.; Lin, J. Remarkable Changes in the Optical Properties of CeO2 Nanocrystals Induced by Lanthanide Ions Doping. *Inorg Chem* **2007**, *46* (13), 5237–5242. https://doi.org/10.1021/ic0701256.

(90) Choppin, G. R.; Peterman, D. R. Applications of Lanthanide Luminescence Spectroscopy to Solution Studies of Coordination Chemistry. *Coord Chem Rev* **1998**, *174* (1), 283–299. https://doi.org/https://doi.org/10.1016/S0010-8545(98)00125-8.

(91) Guo, C.; Lu, X. *Reinvestigation on the Catalytic Lsomerisation of Carbon-Carbon Triple Bonds*; 1993; Vol. 1.

(92) Zhang, J.; Morlens, S.; Hubert-Pfalzgraf, L. G.; Luneau, D. Synthesis, Characterization and Molecular Structures of Yttrium Trifluoroacetate Complexes with O- and N-Donors: Complexation vs. Hydrolysis. *Eur J Inorg Chem* **2005**, *2005* (19), 3928–3935. https://doi.org/https://doi.org/10.1002/ejic.200500156.

(93) Thirumurugan, A.; Natarajan, S. Synthesis, Structure and Luminescent Properties of Yttrium Benzene Dicarboxylates with One- and Three-Dimensional Structure. *Dalton Transactions* **2004**, No. 18, 2923–2928. https://doi.org/10.1039/B408403A.

(94) Matuszewski, J.; Kropiwnicka, J.; Znamierowska, T. The Crystal Structure of Lanthanum Metaphosphate LaP3O9. *J Solid State Chem* **1988**, *75* (2), 285–290. https://doi.org/https://doi.org/10.1016/0022-4596(88)90168-5.

(95) Plessius, R.; Kromhout, R.; Ramos , A. L. D.; Ferbinteanu, M.; Mittelmeijer-Hazeleger, M. C.; Krishna, R.; Rothenberg, G.; Tanase, S. Highly Selective Water Adsorption in a Lanthanum Metal–Organic Framework. *Chemistry – A European Journal* **2014**, *20* (26), 7922–7925. https://doi.org/https://doi.org/10.1002/chem.201403241.

(96) Palenik, G. J. Bond Valence Sums in Coordination Chemistry Using Oxidation State Independent R(0) Values. A Simple Calculation of the Oxidation State of Titanium in Complexes Containing Ti-N, Ti-O, and Ti-Cl Bonds. *Inorg Chem* **1997**, *36* (16), 3394–3397. https://doi.org/10.1021/ic970239p.

(97) Sarma, D.; Prabu, M.; Biju, S.; Reddy, M. L. P.; Natarajan, S. Synthesis, Structure and Optical Studies of a Family of Three-Dimensional Rare-Earth Aminoisophthalates [M(M2-OH)(C8H5NO4)] (M = Y3+, La3+, Pr3+, Nd3+, Sm3+, Eu3+, Gd3+, Dy3+, and Er3+). *Eur J Inorg Chem* **2010**, *2010* (24), 3813–3822. https://doi.org/https://doi.org/10.1002/ejic.201000225.

(98) Xia, J.; Zhao, B.; Wang, H.-S.; Shi, W.; Ma, Y.; Song, H.-B.; Cheng, P.; Liao, D.-Z.; Yan, S.-P. Two- and Three-Dimensional Lanthanide Complexes: Synthesis, Crystal Structures, and Properties. *Inorg Chem* **2007**, *46* (9), 3450–3458. https://doi.org/10.1021/ic061620p.

(99) Hasegawa, Y.; Kitagawa, Y. Luminescent Lanthanide Coordination Polymers with Transformative Energy Transfer Processes for Physical and Chemical Sensing Applications. *Journal of Photochemistry and Photobiology C: Photochemistry Reviews* **2022**, *51*, 100485. https://doi.org/https://doi.org/10.1016/j.jphotochemrev.2022.100485.

(100) Monge, Á.; Gándara, F.; Gutiérrez-Puebla, E.; Snejko, N. Lanthanide, Y and Sc MOFs: Where Amazing Crystal Structures Meet Outstanding Material Properties. *CrystEngComm* **2011**, *13* (16), 5031–5044. https://doi.org/10.1039/C0CE00891E.

(101) Chatenever, A. R. K.; Ehlke, B.; le Maguerès, P.; Reinheimer, E. W.; Song, X.; Fei, H.; Oliver, S. R. J. Structural Diversity of Four Lanthanide Metal–Organic Frameworks Based on 2,6-Naphthalenedicarboxylate: Synthesis, Structures and Photoluminescent Properties. *CrystEngComm* **2021**, *23* (6), 1388–1397. https://doi.org/10.1039/D0CE01448F.

(102) Thirumurugan, A.; Natarajan, S. Inorganic−Organic Hybrid Compounds: Synthesis and Structures of New Metal Organic Polymers Synthesized in the Presence of Mixed Dicarboxylates. *Eur J Inorg Chem* **2004**, *2004* (4), 762–770. https://doi.org/https://doi.org/10.1002/ejic.200300594.

(103) Blasse, G.; Grabmaier, B. C. A General Introduction to Luminescent Materials. In *Luminescent Materials*; Blasse, G., Grabmaier, B. C., Eds.; Springer Berlin Heidelberg: Berlin, Heidelberg, 1994; pp 1–9. https://doi.org/10.1007/978-3-642-79017-1_1.

(104) Alpha, B.; Ballardini, R.; Balzani, V.; Lehn, J.-M.; Perathoner, S.; Sabbatini, N. ANTENNA EFFECT IN LUMINESCENT LANTHANIDE CRYPTATES: A PHOTOPHYSICAL STUDY. *Photochem Photobiol* **1990**, *52* (2), 299–306. https://doi.org/https://doi.org/10.1111/j.1751-1097.1990.tb04185.x.

(105) Hao, J.-N.; Yan, B. Amino-Decorated Lanthanide(Iii) Organic Extended Frameworks for Multi-Color Luminescence and Fluorescence Sensing. *J Mater Chem C Mater* **2014**, *2* (33), 6758–6764. https://doi.org/10.1039/C4TC00962B.

(106) Ramya, A. R.; Sharma, D.; Natarajan, S.; Reddy, M. L. P. Highly Luminescent and Thermally Stable Lanthanide Coordination Polymers Designed from 4-(Dipyridin-2-Yl)Aminobenzoate: Efficient Energy Transfer from Tb3+ to Eu3+ in a Mixed Lanthanide Coordination Compound. *Inorg Chem* **2012**, *51* (16), 8818–8826. https://doi.org/10.1021/ic300654e.

(107) Buono-core, G. E.; Li, H.; Marciniak, B. Quenching of Excited States by Lanthanide Ions and Chelates in Solution. *Coord Chem Rev* **1990**, *99*, 55–87. https://doi.org/https://doi.org/10.1016/0010-8545(90)80060-7.

(108) D'Aléo, A.; Picot, A.; Beeby, A.; Gareth Williams, J. A.; le Guennic, B.; Andraud, C.; Maury, O. Efficient Sensitization of Europium, Ytterbium, and Neodymium Functionalized Tris-Dipicolinate Lanthanide Complexes through Tunable Charge-Transfer Excited States. *Inorg Chem* **2008**, *47* (22), 10258–10268. https://doi.org/10.1021/ic8012969.

(109) Rao, X.; Huang, Q.; Yang, X.; Cui, Y.; Yang, Y.; Wu, C.; Chen, B.; Qian, G. Color Tunable and White Light Emitting Tb3+ and Eu3+ Doped Lanthanide Metal–Organic Framework Materials. *J Mater Chem* **2012**, *22* (7), 3210–3214. https://doi.org/10.1039/C2JM14127B.

(110) Aquino, L. E. do N.; Barbosa, G. A.; Ramos, J. de L.; O. K. Giese, S.; Santana, F. S.; Hughes, D. L.; Nunes, G. G.; Fu, L.; Fang, M.; Poneti, G.; Carneiro Neto, A. N.; Moura, R. T.; Ferreira, R. A. S.; Carlos, L. D.; Macedo, A. G.; Soares, J. F. Seven-Coordinate Tb3+ Complexes with 90% Quantum Yields: High-Performance Examples of Combined Singlet- and Triplet-to-Tb3+ Energy-Transfer Pathways. *Inorg Chem* **2021**, *60* (2), 892–907. https://doi.org/10.1021/acs.inorgchem.0c03020.

(111) Ji, G.; Liu, J.; Gao, X.; Sun, W.; Wang, J.; Zhao, S.; Liu, Z. A Luminescent Lanthanide MOF for Selectively and Ultra-High Sensitively Detecting Pb2+ Ions in Aqueous Solution. *J Mater Chem A Mater* **2017**, *5* (21), 10200–10205. https://doi.org/10.1039/C7TA02439H.

(112) Wang, J.; Jiang, M.; Yan, L.; Peng, R.; Huangfu, M.; Guo, X.; Li, Y.; Wu, P. Multifunctional Luminescent Eu(III)-Based Metal–Organic Framework for Sensing Methanol and Detection and Adsorption of Fe(III) Ions in Aqueous Solution. *Inorg Chem* **2016**, *55* (24), 12660–12668. https://doi.org/10.1021/acs.inorgchem.6b01815.

(113) Yu, Y.; Wang, Y.; Yan, H.; Lu, J.; Liu, H.; Li, Y.; Wang, S.; Li, D.; Dou, J.; Yang, L.; Zhou, Z. Multiresponsive Luminescent Sensitivities of a 3D Cd-CP with Visual Turn-on and Ratiometric Sensing toward Al3+ and Cr3+ as Well as Turn-off Sensing toward Fe3+. *Inorg Chem* **2020**, *59* (6), 3828–3837. https://doi.org/10.1021/acs.inorgchem.9b03496.

(114) Zhang, J.-R.; Lee, J.-J.; Su, C.-H.; Tsai, M.-J.; Li, C.-Y.; Wu, J.-Y. From Lamellar Net to Bilayered-Lamella and to Porous Pillared-Bilayer: Reversible Crystal-to-Crystal Transformation, CO2 Adsorption, and Fluorescence Detection of Fe3+, Al3+, Cr3+, MnO4−, and Cr2O72− in Water. *Dalton Transactions* **2020**, *49* (40), 14201–14215. https://doi.org/10.1039/D0DT02606A.

(115) Mohan Das, K.; Pal, A.; Goswami, B.; Adarsh, N. N.; Thakur, A. Strategic Design of a 2,6-Disubstituted Pyridine-Based Probe Having Hard-Soft Centers: Responsive Divergence from One Core. *New Journal of Chemistry* **2022**, *46* (25), 12103–12119. https://doi.org/10.1039/D2NJ02246J.

(116) Xi, L.; Jin, C.-Y.; Song, H.-W.; Wang, X.-T.; Li, L.-C.; Sutter, J.-P. Supramolecular Heptanuclear Ln–Cu Complexes Involving Nitronyl Nitroxide Biradicals: Structure and Magnetic Behavior. *Dalton Transactions* **2022**, *51* (17), 6955–6963. https://doi.org/10.1039/D2DT00220E.

(117) Sutter, J.-P.; Béreau, V.; Jubault, V.; Bretosh, K.; Pichon, C.; Duhayon, C. Magnetic Anisotropy of Transition Metal and Lanthanide Ions in Pentagonal Bipyramidal Geometry. *Chem Soc Rev* **2022**, *51* (8), 3280–3313. https://doi.org/10.1039/D2CS00028H.

(118) Kalita, P.; Ahmed, N.; Bar, A. K.; Dey, S.; Jana, A.; Rajaraman, G.; Sutter, J.-P.; Chandrasekhar, V. Pentagonal Bipyramidal Ln(III) Complexes Containing an Axial Phosphine Oxide Ligand: Field-Induced Single-Ion Magnetism Behavior of the Dy(III) Analogues. *Inorg Chem* **2020**, *59* (9), 6603–6612. https://doi.org/10.1021/acs.inorgchem.0c00751.

(119) Tanase, S.; Mittelmeijer-Hazeleger, M. C.; Rothenberg, G.; Mathonière, C.; Jubera, V.; Smits, J. M. M.; de Gelder, R. A Facile Building-Block Synthesis of Multifunctional Lanthanide MOFs. *J Mater Chem* **2011**, *21* (39), 15544–15551. https://doi.org/10.1039/C1JM12789F.

(120) Castells-Gil, J.; Mañas-Valero, S.; Vitórica-Yrezábal, I. J.; Ananias, D.; Rocha, J.; Santiago, R.; Bromley, S. T.; Baldoví, J. J.; Coronado, E.; Souto, M.; Mínguez Espallargas, G. Electronic, Structural and Functional Versatility in Tetrathiafulvalene-Lanthanide Metal–Organic Frameworks. *Chemistry – A European Journal* **2019**, *25* (54), 12636–12643. https://doi.org/https://doi.org/10.1002/chem.201902855.

(121) Zhang, C.; Ma, X.; Cen, P.; Jin, X.; Yang, J.; Zhang, Y.-Q.; Ferrando-Soria, J.; Pardo, E.; Liu, X. A Series of Lanthanide(Iii) Metal–Organic Frameworks Derived from a Pyridyl-Dicarboxylate Ligand: Single-Molecule Magnet Behaviour and Luminescence Properties. *Dalton Transactions* **2020**, *49* (40), 14123–14132. https://doi.org/10.1039/D0DT02736G.

(122) Kang, Y.-S.; Lu, Y.; Chen, K.; Zhao, Y.; Wang, P.; Sun, W.-Y. Metal–Organic Frameworks with Catalytic Centers: From Synthesis to Catalytic Application. *Coord Chem Rev* **2019**, *378*, 262–280. https://doi.org/https://doi.org/10.1016/j.ccr.2018.02.009.

(123) Chen, Y.; Ma, S. Microporous Lanthanide Metal-Organic Frameworks. *Reviews in Inorganic Chemistry* **2012**, *32* (2–4), 81–100. https://doi.org/doi:10.1515/revic-2012-0003.

(124) D'Vries, R. F.; de la Peña-O'Shea, V. A.; Snejko, N.; Iglesias, M.; Gutiérrez-Puebla, E.; Monge, M. Á. Insight into the Correlation between Net Topology and Ligand Coordination Mode in New Lanthanide MOFs Heterogeneous Catalysts: A Theoretical and Experimental Approach. *Cryst Growth Des* **2012**, *12* (11), 5535–5545. https://doi.org/10.1021/cg301096d.

(125) Zhang, Y.; Liu, S.; Zhao, Z.-S.; Wang, Z.; Zhang, R.; Liu, L.; Han, Z.-B. Recent Progress in Lanthanide Metal–Organic Frameworks and Their Derivatives in Catalytic Applications. *Inorg Chem Front* **2021**, *8* (3), 590–619. https://doi.org/10.1039/D0QI01191F.

(126) Kumar, N.; Paul, A. K. Triggering Lewis Acidic Nature through the Variation of Coordination Environment of Cd-Centers in 2D-Coordination Polymers. *Inorg Chem* **2020**, *59* (2), 1284–1294. https://doi.org/10.1021/acs.inorgchem.9b02997.

(127) Kumar, N.; Rom, T.; Singh, V.; Paul, A. K. Transition Metal Ions Regulated Structural and Catalytic Behaviors of Coordination Polymers. *Cryst Growth Des* **2020**, *20* (8), 5277–5288. https://doi.org/10.1021/acs.cgd.0c00465.

(128) Rom, T.; Paul, A. K. Role of Aromatic vs. Aliphatic Amine for the Variation of Structural, Electrical and Catalytic Behaviors in a Series of Silver Phosphonate Extended Hybrid Solids. *Dalton Transactions* **2020**, *49* (39), 13618–13634. https://doi.org/10.1039/D0DT02796K.

(129) Rom, T.; Agrawal, A.; Sarkar, S.; Mahata, P.; Kumar, A.; Paul, A. K. Organoamine Templated Multifunctional Hybrid Metal Phosphonate Frameworks: Promising Candidates for Tailoring Electrochemical Behaviors and Size-Selective Efficient Heterogeneous Lewis Acid Catalysis. *Inorg Chem* **2022**, *61* (25), 9580–9594. https://doi.org/10.1021/acs.inorgchem.2c00811.

SUPPORTING INFORMATION

Table of Contents:

Table S1: Elemental analysis for all the compounds

	Carbon %		Hydrogen %		Nitrogen %		Oxygen%	
	Expt.	Calc.	Expt.	Calc.	Expt.	Calc.	Expt.	Calc.
1	42.02	45.5	4.00	4.02	-	-	38.57	39.65
2	37.98	38.37	3.89	3.68			35.69	36.51
3	38.67	38.18	3.72	3.66			34.69	36.33
4	38.67	37.83	3.72	3.63			36.7	35.99
5	38.9	37.74	3.67	3.62			35.09	35.91
6	38.81	37.44	3.74	3.59			35.11	35.62
7	39.9	37.35	3.64	3.58			34.7	35.54
8	38.5	37.15	3.73	3.56	-	-	34.46	35.35
9	43.3	44.45	3.9	3.93	3.20	3.7	29.34	28.51
10	43.50	43.49	3.7	3.92	3.56	3.76	30.36	30.04
11	44.57	44.9	3.74	3.2	3.85	3.50	28.58	32.0

Table S2: Selected bond lengths (Å) and bond angles (deg) for **Y** compound, **1-8**

Compound **1**			
Bond length(Å)		**Bond angle (°)**	
Y1-O6	2.338 (17)	O6-Y1-O7	74.36 (6)
Y1-O7	2.379 (14)	O6- Y1-O100	149.79 (6)
Y1-O100	2.357 (4)	O6- Y1-O200	136.06 (7)
Y1-O200	2.332 (3)	O2[a]- Y1-O6	83.33 (6)
Y1-O2[a]	2.427 (3)	O3[a]- Y1-O6	87.83 (6)
Y1-O3[a]	2.372 (2)	O5[c]- Y1-O6	117.72 (6)
Y1-O5[c]	2.547 (2)	O6- Y1-O6[c]	72.61 (5)
Y1-O6[c]	2.471 (2)	O6- Y1-O8[c]	71.76 (5)
Y1-O8[c]	2.498 (2)	O7- Y1-O100	82.61 (6)
		O7- Y1-O200	142.66 (7)
		O2[a]- Y1-O7	74.15 (5)
		O3[a]- Y1-O7	126.59 (6)
		O5[c]- Y1-O7	72.59 (6)
		O6[c]- Y1-O7	81.52 (5)
		O7- Y1-O8[c]	140.14 (6)
		O100- Y1-O200	73.36 (7)
		O2[a]- Y1-O100	71.58 (6)
		O3[a]- Y1-O100	90.51 (7)
		O5[c]- Y1-O100	71.93 (6)
		O6[c]- Y1-O100	123.45 (6)
		O8[c]- Y1-O100	135.93 (6)
		O2[a]-Y1-O200	122.13 (7)
		O3[a]- Y1-O200	82.52 (7)
		O5[c]- Y1-O200	72.98 (7)
		O6[c]- Y1-O200	88.28 (6)
		O8[c]- Y1-O200	64.44 (7)
		O2[a]- Y1-O3[a]	53.70 (6)
		O2[a]- Y1-O5[c]	132.93 (6)
		O2[a]- Y1-O6[c]	149.59 (5)
		O2[a]- Y1-O8[c]	121.18 (6)
		O3[a]- Y1-O5[c]	152.98 (7)
		O3[a] -Y1-O6[c]	140.45 (7)
		O3[a]- Y1-O8[c]	72.50 (6)
		O5[c]- Y1-O6[c]	51.52 (6)
		O5[c]- Y1-O8[c]	105.70 (6)
		O6[c]- Y1-O8[c]	68.85 (5)

Translation of Symmetry Code to Equiv. Pos

a = 1-x,-y,1-z

b = 1-x,1-y,-z

c = 1-x,1-y,1-z

Compound **2**			
Bond length(Å)		**Bond angle (°)**	
Pr1-O6	2.44(2)	O6-Pr1-O7	72.29(7)
Pr1-O7	2.46(2)	O6-Pr1-O100	148.41(9)
Pr1-O100	2.45(4)	O6-Pr1-O200	137.16(10)
Pr1-O200	2.43(3)	O2^{b}-Pr1-O6	82.78(9)
Pr1-O2^{b}	2.51(3)	O3^{b}-Pr1-O6	86.83(9)
Pr1-O3^{b}	2.47(2)	O5^{c}-Pr1-O6	116.72(9)
Pr1-O5^{c}	2.63(2)	O6-Pr1-O6^{c}	73.72(7)
Pr1-O6^{c}	2.56(2)	O6-Pr1-O8^{c}	72.27(7)
Pr1-O8^{c}	2.52(2)	O7-Pr1-O100	83.60(9)
		O7-Pr1-O200	143.50(10)
		O2^{b}-Pr1-O7	75.25(9)
		O3^{b}-Pr1-O7	125.52(9)
		O5^{c}-Pr1-O7	72.10(9)
		O6^{c}-Pr1-O7	80.30(7)
		O7-Pr1-O8^{c}	138.03(8)
		O100-Pr1-O200	73.64(11)
		O2^{b}-Pr1-O100	71.34(10)
		O3^{b}-Pr1-O100	91.08(10)
		O5^{c}-Pr1-O100	72.72(9)
		O6^{c}-Pr1-O100	122.70(7)
		O8^{c}-Pr1-O100	136.95(9)
		O2^{b}-Pr1-O200	121.43(11)
		O3^{b}-Pr1-O200	83.79(10)
		O5^{c}-Pr1-O200	74.05(10)
		O6^{c}-Pr1-O200	88.34(9)
		O8^{c}-Pr1-O200	64.96(10)
		O2^{b}-Pr1-O3^{b}	52.09(10)
		O2^{b}-Pr1-O5^{c}	133.35(10)
		O2^{b}-Pr1-O6^{c}	150.23(9)
		O2^{b}-Pr1-O8^{c}	121.22(9)
		O3^{b}-Pr1-O5^{c}	155.38(10)
		O3^{b}-Pr1-O6^{c}	141.42(10)
		O3^{b}-Pr1-O8^{c}	73.72(9)
		O5^{c}-Pr1-O6^{c}	49.98(9)
		O5^{c}-Pr1-O8^{c}	105.32(9)
		O6^{c}-Pr1-O8^{c}	68.76(7)

Translation of Symmetry Code to Equiv.Pos

b = 1-x,1-y,-z

c = 1-x,1-y,1-z

Compound **3**			
Bond length(Å)		**Bond angle (°)**	
Nd1-O6	2.435(2)	O6-Nd1-O7	72.29(7)
Nd1-O7	2.461(2)	O6-Nd1-O100	148.52(7)
Nd1-O100	2.444(2)	O6-Nd1-O200	137.30(10)
Nd1-O200	2.426(2)	$O2^{b}$-Nd11-O6	82.88(7)
Nd1-$O2^{b}$	2.505(2)	$O3^{b}$-Nd1-O6	86.53(8)
Nd1-$O3^{b}$	2.464(2)	$O5^{a}$-Nd1-O6	116.86(7)
Nd1-$O5^{a}$	2.615(2)	O6-Nd1-$O6^{a}$	73.76(7)
Nd1-$O6^{a}$	2.562(2)	O6-Nd1-$O8^{a}$	72.28(7)
Nd1-$O8^{a}$	2.522(2)	O7-Nd1-O100	83.70(7)
		O7-Nd1-O200	143.62(9)
		$O2^{b}$-Nd1-O7	75.24(7)
		$O3^{b}$-Nd1-O7	125.52(7)
		$O5^{a}$-Nd1-O7	72.20(7)
		$O6^{a}$-Nd1-O7	80.47(7)
		O7-Nd1-$O8^{a}$	138.07(8)
		O100-Nd1-O200	73.34(9)
		$O2^{b}$-Nd1-O100	71.29(8)
		$O3^{b}$-Nd1-O100	91.39(9)
		$O5^{a}$-Nd1-O100	72.60(7)
		$O6^{a}$-Nd1-O100	122.73(7)
		$O8^{a}$-Nd1-O100	136.81(7)
		$O2^{b}$-Nd1-O200	121.02(9)
		$O3^{b}$-Nd1-O200	82.72(7)
		$O5^{a}$-Nd1-O200	74.17(9)
		$O6^{a}$-Nd1-O200	88.55(9)
		$O8^{a}$-Nd1-O200	65.07(9)
		$O2^{b}$-Nd1-$O3^{b}$	52.23(8)
		$O2^{b}$-Nd1-$O5^{a}$	133.25(7)
		$O2^{b}$-Nd1-$O6^{a}$	150.43(7)
		$O2^{b}$-Nd1-$O8^{a}$	121.25(7)
		$O3^{b}$-Nd1-$O5^{a}$	155.50(8)
		$O3^{b}$-Nd1-$O6^{a}$	141.01(9)
		$O3^{b}$-Nd1-$O8^{a}$	73.44(9)
		$O5^{a}$-Nd1-$O6^{a}$	50.13(7)
		$O5^{a}$-Nd1-$O8^{a}$	105.37(7)
		$O6^{a}$-Nd1-$O8^{a}$	68.66(7)

Translation of Symmetry Code to Equiv. Pos

a = 1-x,1-y,1-z

b = 1-x,1-y,2-z

Compound **4**			
Bond length(Å)		**Bond angle (°)**	
Sm1-O6	2.407(2)	O6-Sm1-O7	72.88(7)
Sm1-O7	2.433(2)	O6-Sm1-O100	148.22(7)
Sm1-O100	2.417(4)	O6-Sm1-O200	137.27(8)
Sm1-O200	2.398(3)	$O2^{b}$-Sm1-O6	82.45(7)
Sm1-$O2^{b}$	2.480(3)	$O3^{b}$-Sm1-O6	87.20(8)
Sm1-$O3^{b}$	2.438(2)	$O5^{c}$-Sm1-O6	117.26(7)
Sm1-$O5^{c}$	2.592(2)	O6-Sm1-$O6^{c}$	73.60(7)
Sm1-$O6^{c}$	2.532(2)	O6-Sm1-$O8^{c}$	72.28(7)
Sm1-$O8^{c}$	2.502(2)	O7-Sm1-O100	82.80(7)
		O7-Sm1-O200	142.95(7)
		$O2^{b}$-Sm1-O7	74.70(7)
		$O3^{b}$-Sm1-O7	126.01(7)
		$O5^{c}$-Sm1-O7	72.15(7)
		$O6^{c}$-Sm1-O7	80.82(7)
		O7-Sm1-$O8^{c}$	138.82(7)
		O100-Sm1-O200	73.73(8)
		$O2^{b}$-Sm1-O100	71.42(7)
		$O3^{b}$-Sm1-O100	91.00(9)
		$O5^{c}$-Sm1-O100	72.28(7)
		$O6^{c}$-Sm1-O100	122.95(7)
		$O8^{c}$-Sm1-O100	137.04(7)
		$O2^{b}$-Sm1-O200	121.89(7)
		$O3^{b}$-Sm1-O200	83.35(7)
		$O5^{c}$-Sm1-O200	73.58(7)
		$O6^{c}$-Sm1-O200	88.28(7)
		$O8^{c}$-Sm1-O200	65.08(7)
		$O2^{b}$-Sm1-$O3^{b}$	52.84(8)
		$O2^{b}$-Sm1-$O5^{c}$	133.06(7)
		$O2^{b}$-Sm1-$O6^{c}$	149.83(7)
		$O2^{b}$-Sm1-$O8^{c}$	121.06(7)
		$O3^{b}$-Sm1-$O5^{c}$	154.42(8)
		$O3^{b}$-Sm1-$O6^{c}$	141.02(9)
		$O3^{b}$-Sm1-$O8^{c}$	73.14(9)
		$O5^{c}$-Sm1-$O6^{c}$	50.67(7)
		$O5^{c}$-Sm1-$O8^{c}$	105.77(7)
		$O6^{c}$-Sm1-$O8^{c}$	68.83(7)

Translation of Symmetry Code to Equiv.Pos

b = 1-x,1-y,1-z

c = 1-x,1-y,2-z

Compound **5**			
Bond length(Å)		**Bond angle (°)**	
Eu1-O6	2.394(2)	O6-Eu1-O7	73.20(9)
Eu1-O7	2.419(2)	O6-Eu1-O100	148.32(9)
Eu1-O100	2.401 (4)	O6-Eu1-O200	137.15(10)
Eu1-O200	2.384(3)	$O2^{b}$-Eu1-O6	82.29(10)
Eu1-$O2^{b}$	2.472(3)	$O3^{b}$-Eu1-O6	87.44(9)
Eu1-$O3^{b}$	2.428(2)	$O5^{c}$-Eu1-O6	117.42(9)
Eu1-$O5^{c}$	2.585(2)	O6-Eu1-$O6^{c}$	73.42(7)
Eu1-$O6^{c}$	2.519(2)	O6-Eu1-$O8^{c}$	72.22(8)
Eu1-$O8^{c}$	2.493(3)	O7-Eu1-O100	82.66(11)
		O7-Eu1-O200	142.42(10)
		$O2^{b}$-Eu1-O7	74.59(9)
		$O3^{b}$-Eu1-O7	126.32(9)
		$O5^{c}$-Eu1-O7	72.07(9)
		$O6^{c}$-Eu1-O7	80.73(8)
		O7-Eu1-$O8^{c}$	139.11(10)
		O100-Eu1-O200	73.72(11)
		$O2^{b}$-Eu1-O100	71.55(11)
		$O3^{b}$-Eu1-O100	90.76(11)
		$O5^{c}$-Eu1-O100	72.23(11)
		$O6^{c}$-Eu1-O100	123.10(10)
		$O8^{c}$-Eu1-O100	137.04(7)
		$O2^{b}$-Eu1-O200	122.06(11)
		$O3^{b}$-Eu1-O200	82.99(11)
		$O5^{c}$-Eu1-O200	73.55(11)
		$O6^{c}$-Eu1-O200	88.50(10)
		$O8^{c}$-Eu1-O200	65.03(10)
		$O2^{b}$-Eu1-$O3^{b}$	53.11(10)
		$O2^{b}$-Eu1-$O5^{c}$	133.05(10)
		$O2^{b}$-Eu1-$O6^{c}$	149.43(9)
		$O2^{b}$-Eu1-$O8^{c}$	120.90(9)
		$O3^{b}$-Eu1-$O5^{c}$	153.99(10)
		$O3^{b}$-Eu1-$O6^{c}$	141.06(10)
		$O3^{b}$-Eu1-$O8^{c}$	72.93(10)
		$O5^{c}$-Eu1-$O6^{c}$	50.88(9)
		$O5^{c}$-Eu1-$O8^{c}$	105.93(9)
		$O6^{c}$-Eu1-$O8^{c}$	69.05(7)

Translation of Symmetry Code to Equiv.Pos

b = 1-x,1-y,1-z

c = 1-x,1-y,2-z

Compound **6**			
Bond length(Å)		**Bond angle (°)**	
Gd1-O6	2.3582(2)	O6-Gd1-O7	73.38(7)
Gd1-O7	2.4105 (19)	O6-Gd1-O100	148.39(7)
Gd1-O100	2.389 (2)	O6-Gd1-O200	137.09(8)
Gd1-O200	2.374 (2)	$O2^{b}$-Gd11-O6	82.31(7)
Gd1-$O2^{b}$	2.463 (2)	$O3^{b}$-Gd1-O6	87.79(8)
Gd1-$O3^{b}$	2.417 (2)	$O5^{a}$-Gd1-O6	117.43(7)
Gd1-$O5^{a}$	2.576 (2)	O6-Gd1-$O6^{a}$	73.23(7)
Gd1-$O6^{a}$	2.507(2)	O6-Gd1-$O8^{a}$	72.22(7)
Gd1-$O8^{a}$	2.488 (2)	O7-Gd1-O100	82.56(7)
		O7-Gd1-O200	142.74(7)
		$O2^{b}$-Gd1-O7	74.42(7)
		$O3^{b}$-Gd1-O7	126.43(7)
		$O5^{a}$-Gd1-O7	72.14(7)
		$O6^{a}$-Gd1-O7	80.89(7)
		O7-Gd1-$O8^{a}$	139.34(7)
		O100-Gd1-O200	73.70(8)
		$O2^{b}$-Gd1-O100	71.52(7)
		$O3^{b}$-Gd1-O100	90.40(9)
		$O5^{a}$-Gd1-O100	72.32(7)
		$O6^{a}$-Gd1-O100	123.34(7)
		$O8^{a}$-Gd1-O100	136.81(7)
		$O2^{b}$-Gd1-O200	122.14(7)
		$O3^{b}$-Gd1-O200	82.72(7)
		$O5^{a}$-Gd1-O200	73.48(7)
		$O6^{a}$-Gd1-O200	88.56(7)
		$O8^{a}$-Gd1-O200	64.96(7)
		$O2^{b}$-Gd1-$O3^{b}$	53.26(8)
		$O2^{b}$-Gd1-$O5^{a}$	133.07(7)
		$O2^{b}$-Gd1-$O6^{a}$	149.30(7)
		$O2^{b}$-Gd1-$O8^{a}$	120.99(7)
		$O3^{b}$-Gd1-$O5^{a}$	153.61(8)
		$O3^{b}$-Gd1-$O6^{a}$	141.07(9)
		$O3^{b}$-Gd1-$O8^{a}$	73.01(9)
		$O5^{a}$-Gd1-$O6^{a}$	51.02(7)
		$O5^{a}$-Gd1-$O8^{a}$	105.83(7)
		$O6^{a}$-Gd1-$O8^{a}$	68.95(7)

Translation of Symmetry Code to Equiv. Pos

a = 1-x,1-y,-z

b = 1-x,1-y,1-z

Compound 7			
Bond length(Å)		**Bond angle (°)**	
Tb1-O6	2.372(2)	O6-Tb1-O7	73.42(8)
Tb1-O7	2.396(2)	O6-Tb1-O100	148.32(7)
Tb1-O100	2.376(2)	O6-Tb1-O200	137.15(10)
Tb1-O200	2.357(2)	$O2^{b}$-Tb1-O6	82.25(7)
Tb1-$O2^{b}$	2.448(2)	$O3^{b}$-Tb1-O6	88.22(9)
Tb1-$O3^{b}$	2.402(2)	$O5^{a}$-Tb1-O6	117.46(7)
Tb1-$O5^{a}$	2.569(2)	O6-Tb1-$O6^{a}$	73.16(7)
Tb1-$O6^{a}$	2.494(2)	O6-Tb1-$O8^{a}$	72.26(7)
Tb1-$O8^{a}$	2.481(2)	O7-Tb1-O100	82.37(8)
		O7-Tb1-O200	142.60(10)
		$O2^{b}$-Tb1-O7	74.21(7)
		$O3^{b}$-Tb1-O7	126.61(8)
		$O5^{a}$-Tb1-O7	72.06(7)
		$O6^{a}$-Tb1-O7	81.09(7)
		O7-Tb1-$O8^{a}$	139.52(8)
		O100-Tb1-O200	73.75(10)
		$O2^{b}$-Tb1-O100	71.55(8)
		$O3^{b}$-Tb1-O100	90.19(10)
		$O5^{a}$-Tb1-O100	73.41(9)
		$O6^{a}$-Tb1-O100	123.40(8)
		$O8^{a}$-Tb1-O100	136.85(7)
		$O2^{b}$-Tb1-O200	122.38(10)
		$O3^{b}$-Tb1-O200	82.50(9)
		$O5^{a}$-Tb1-O200	73.41(9)
		$O6^{a}$-Tb1-O200	88.42(9)
		$O8^{a}$-Tb1-O200	65.01(10)
		$O2^{b}$-Tb1-$O3^{b}$	53.54(8)
		$O2^{b}$-Tb1-$O5^{a}$	132.83(7)
		$O2^{b}$-Tb1-$O6^{a}$	149.20(7)
		$O2^{b}$-Tb1-$O8^{a}$	120.93(7)
		$O3^{b}$-Tb1-$O5^{a}$	153.19(8)
		$O3^{b}$-Tb1-$O6^{a}$	141.06(9)
		$O3^{b}$-Tb1-$O8^{a}$	72.89(9)
		$O5^{a}$-Tb1-$O6^{a}$	51.27(7)
		$O5^{a}$-Tb1-$O8^{a}$	106.13(7)
		$O6^{a}$-Tb1-$O8^{a}$	68.97(7)

Translation of Symmetry Code to Equiv.Pos

a = 1-x,1-y,-z

b = 1-x,1-y,1-z

Compound **8**			
Bond length(Å)		**Bond angle (°)**	
Dy1-O6	2.358 (2)	O6-Dy1-O7	74.14 (7)
Dy1-O7	2.388 (19)	O6-Dy1-O100	149.29 (7)
Dy1-O100	2.373 (2)	O6-Dy1-O200	136.67 (10)
Dy1-O200	2.352 (2)	O2^{a}-Dy1-O6	83.33 (6)
Dy1-O2^{c}	2.439 (2)	O3^{a}-Dy1-O6	87.83 (6)
Dy1-O3^{c}	2.492 (2)	O5^{a}-Dy1-O6	118.10(8)
Dy1-O5^{a}	2.555 (2)	O6-Dy1-O6^{a}	73.02(7)
Dy1-O6^{a}	2.484 (2)	O6-Dy1-O8^{a}	72.04(7)
Dy1-O8^{a}	2.484 (2)	O7-Dy1-O100	82.60 (8)
		O7-Dy1-O200	142.69 (10)
		O2^{c}-Dy1-O7	74.40 (7)
		O3^{c}-Dy1-O7	126.57 (7)
		O5^{a}-Dy1-O7	72.63(9)
		O6^{a}-Dy1-O7	80.67(7)
		O7-Dy1-O8^{a}	139.78(8)
		O100-Dy1-O200	73.14(10)
		O2^{c}-Dy1-O100	71.49(9)
		O3^{c}-Dy1-O100	90.62 (10)
		O5^{a}-Dy1-O100	71.86 (8)
		O6^{a}-Dy1-O100	123.08(7)
		O8^{a}-Dy1-O100	136.17(7)
		O2^{c}-Dy1-O200	121.56(10)
		O3^{c}-Dy1-O200	82.37(9)
		O5^{a}-Dy1-O200	73.08(10)
		O6^{a}-Dy1-O200	89.18(9)
		O8^{a}-Dy1-O200	64.69 (10)
		O2^{c}-Dy1-O3^{c}	53.49 (8)
		O2^{c}-Dy1-O5^{a}	133.00(9)
		O2^{c}-Dy1-O6^{a}	149.26(7)
		O2^{c}-Dy1-O8^{a}	121.54(8)
		O3^{c}-Dy1-O5^{a}	153.00(9)
		O3^{c}-Dy1-O6^{a}	141.12(9)
		O3^{c}-Dy1-O8^{a}	73.00(9)
		O5^{a}-Dy1-O6^{a}	51.22(8)
		O5^{a}-Dy1-O8^{a}	105.25(8)
		O6^{a}-Dy1-O8^{a}	69.12(7)

Translation of Symmetry Code to Equiv. Pos

a = 1-x,1-y,-z

c = 1-x,2-y,-z

Table S3. Hydrogen bonding for compounds **1-8**

D-H···A (Å)	d(D-H) (Å)	d(H-A) (Å)	d(D···A) (Å)	∠DHA (°)	Symmetry transform
Compound **1**					
O200–H20A···O9	0.93	1.910	2.822 (3)	168.00	-x, 1-y, 1-z
O300–H30B···O5	0.85	2.020	2.866 (3)	173.00	-1+x, y, z
O400–H40B···O7	0.850	2.070	2.882 (3)	159.00	-x, 1-y, 1-z
O500–H50A···O400	0.85	1.960	2.776(2)	162.00	
O500–H50B···O600	0.85	1.800	2.647(2)	178.00	
O600–H60B···O8	0.85	2.07	2.846(2)	152.00	-1+x, y, 1+z
C1-H1···O5	0.93	2.440	3.341(5)	164.00	2-x,-y,1-z
Compound **2**					
O200–H20A···O9	0.93	1.93	2.835(5)	165.00	1+x, -1+y, z
O300–H30B···O5	0.85	2.00	2.83(5)	165.00	-1+x, y, z
O400–H40B···O7	0.85	2.02	2.84(4)	162.00	-x, 1-y, 1-z
O500–H50A···O600	0.85	1.82	2.65(4)	168.00	
O500–H50B···O400	0.85	1.99	2.78(5)	154	
O600–H60A···O4	0.85	2.09	2.87(5)	152	x, -1+y,1+z
O600–H60B···O8	0.85	2.01	2.84(4)	165.00	x, -1+y,z
O600–H60A···O3	0.93	2.38	3.28(7)	163.00	x, -1+y,1+z
Compound **3**					
O200–H20A···O9	0.87	1.98	2.835(4)	164.00	-1+x,1+y,z
O200–H20B···O500	0.87	1.80	2.598(6)	150.00	
O300–H30B···O5	0.85	1.99	2.827(4)	169.00	1+x,y,z
O600–H60A···O8	0.85	2.05	2.837(4)	153	x,1+y,z
C1-H1···O5	0.93	2.380	3.284(6)	163.00	-x,1-y,2-z

Compound **4**					
O200–H20A···O9	0.86	1.99	2.826(3)	163.00	1-x,1-y,2-z
O100–H10B···O300	0.87	1.91	2.710(4)	151	
O200–H20A···O9	0.86	1.99	2.826(3)	163.00	1-x,1-y,2-z
O300–H30B···O5	0.85	2.00	2.834(4)	166.00	-1+x,y,z
O400–H40A···O7	0.85	2.02	2.8431(3)	163.00	-x,1-y,2-z
O500–H50A···O400	0.85	1.99	2.774(3)	154.00	
O500–H50B···O600	0.85	1.81	2.656(4)	171.00	
C1-H1···O5	0.93	2.380	3.281(6)	163.00	2-x,1-y,1-z
Compound **5**					
O200–H20A···O9	0.93	1.91	2.825(5)	166.00	1-x,1-y,2-z
O100–H10A···O400	0.86(6)	1.96(6)	2.791(5)	162(6)	
O100–H10B···O300	0.82(6)	1.89(6)	2.708(5)	174(7)	
O300–H30B···O5	0.85	2.01	2.839(5)	163.00	-1+x,y,z
O400–H40B···O7	0.85	2.02	2.842(6)	162.00	-x,1-y,2-z
O500–H50A···O600	0.85	1.80	2.646(6)	176.00	
O500–H50B···O400	0.85	1.97	2.77(6)	156.00	
O600–H60B···O8	0.85	2.02	2.827(4)	159.00	x,-1+y,z
C1-H1···O5	0.93	2.380	3.281(7)	164.00	2-x,1-y,1-z
Compound **6**					
O200–H20A···O9	0.93	1.91	2.822(3)	166.00	1-x,1-y,-z

O300–H30B···O5	0.85	2.00	2.843(4)	170.00	1+x,y,z
O400–H40B···O7	0.85	2.02	2.841(3)	163.00	2-x, 1-y, -z
O500–H50A···O400	0.85	1.96	2.773(3)	159.00	
O500–H50B···O600	0.85	1.82	2.656(3)	168.00	
O600–H60A···O8	0.85	2.01	2.824(3)	159.00	x, 1+y, z
C1-H1···O5	0.93	2.380	3.283(6)	164.00	-x,1-y,1-z
Compound **7**					
O200–H20A···O9	0.93	1.91	2.817(3)	167.00	2_665; 1-x,1-y,-z
O400–H40A···O7	0.85	2.04	2.846(3)	159.00	
O600–H60B···O5	0.85	2.01	2.841(4)	166.00	
C1-H1···O5	0.93	2.380	3.281(6)	164.00	2_566; -x,1-y,1-z
Compound **8**					
O200–H20A···O9	0.93	1.93	2.840(4)	165.00	x, y,-1+z
C1-H1···O5	0.93	2.460	3.366(6)	164.00	-x,2-y,-z

Table S4: Selected bond lengths (Å) and bond angles (deg) for **9-11**

Compound **9**			
Bond length(Å)		**Bond angle (°)**	
La1-ODMF	2.553(7)	ODMF-La1-O2	119.94 (15)
La1-O2	2.647(4)	ODMF-La1-O3	74.27 (16)
La1-O3	2.554 (4)	ODMF-La1-O6	77.84 (15)
La1-O6	2.461 (4)	ODMF-La1-O7	129.37 (19)
La1-O7	2.444 (4)	ODMF-La1-O100	74.2 (2)
La1-O100	2.570 (7)	ODMF-La1-O5^{b}	141.17 (18)
La1-O5^{b}	2.633 (3)	ODMF-La1-O6^{b}	135.63 (15)
La1-O6^{b}	2.641 (4)	ODMF-La1-O8^{b}	72.91 (19)
La1-O8^{b}	2.510 (5)	O2-La1-O3	49.31(13)
		O2-La1-O6	147.09 (14)
		O2-La1-O7	72.68 (13)
		O2-La1-O100	76.43 (19)
		O2-La1-O5^{b}	68.63 (14)
		O2-La1-O6^{b}	103.89 (13)
		O2-La1-O8^{b}	139.01 (15)
		O3-La1-O6	123.92 (13)
		O3-La1-O7	86.90 (14)
		O3-La1-O100	79.12(19)
		O3-La1-O5^{b}	115.85 (13)
		O3-La1- O6^{b}	149.09 (14)
		O3-La1- O8^{b}	139.84 (15)
		O6-La1-O7	74.86 (14))
		O6-La1-O100	136.5 (2)
		O5^{b}-La1-O6	116.45 (12)
		O6-La1-O6^{b}	68.02(11)
		O6-La1-O8^{b}	70.09 (15)
		O7-La1-O100	148.0 (2)
		O5^{b}-La1-O7	89.39 (17)
		O6^{b}-La1-O7	67.97 (15)
		O7-La1-O8^{b}	132.28 (13)
		O5^{b}-La1-O100	71.6 (2)
		O6^{b}-La1-O100	112.7 (2)
		O8^{b}-La1-O100	70.18 (19)
		O5^{b}-La1-O6^{b}	49.32 (12)
		O5^{b} -La1-O8^{b}	78.62 (18)
		O6^{b} -La1-O8^{b}	69.41 (15)

Translation of Symmetry Code to Equiv.Pos

b = 2-x,1-y,1-z

Compound **10**			
Bond length(Å)		**Bond angle (°)**	
Ce1-ODMF	2.516(6)	ODMF-Ce1-O2	117.71(13)
Ce1-O2	2.612(4)	ODMF-Ce1-O3	72.62(15)
Ce1-O3	2.522(4)	ODMF-Ce1-O6	78.03(12)
Ce1-O6	2.424(3)	ODMF-Ce1-O8	128.74(16)
Ce1-O8	2.426(4)	ODMF-Ce1-O100	73.1(2)
Ce1-O100	2.528(6)	ODMF-Ce1-O5^{c}	142.72(16)
Ce1-O5^{c}	2.597(3)	ODMF-Ce1-O6^{c}	135.65(12)
Ce1-O6^{c}	2.615(3)	ODMF-Ce1-O7^{c}	73.93(18)
Ce1-O7^{c}	2.483(4)	O2-Ce1-O3	49.41(12)
		O2-Ce1-O6	147.80(12)
		O2-Ce1-O8	73.64(13)
		O2-Ce1-O100	76.32(17)
		O2-Ce1-O5^{c}	68.81(11)
		O2-Ce1-O6^{c}	106.18(10)
		O2-Ce1-O7^{c}	138.53(15)
		O3-Ce1-O6	121.80(12)
		O3-Ce1-O8	86.07(14)
		O3-Ce1-O100	80.29(18)
		O3-Ce1-O5^{c}	116.87(12)
		O3-Ce1-O6^{c}	150.08(12)
		O3-Ce1-O7^{c}	139.97(15)
		O6-Ce1-O8	74.87(12)
		O6-Ce1-O100	135.75(17)
		O5^{c}-Ce1-O6	116.97(9)
		O6-Ce1-O6^{c}	67.53(10)
		O6-Ce1-O7^{c}	70.78(13)
		O8-Ce1-O100	148.95(18)
		O5^{c}-Ce1-O8	88.53(14)
		O6^{c}-Ce1-O8	68.37(12)
		O7^{c}-Ce1-O8	132.72(13)
		O5^{c}-Ce1-O100	73.4(2)
		O6^{c}-Ce1-O100	113.70(19)
		O7^{c}-Ce1-O100	69.42(17)
		O5^{c}-Ce1-O6^{c}	50.03(9)
		O5^{c}-Ce1-O7^{c}	79.36(17)
		O6^{c}-Ce1-O7^{c}	68.99(14)

Translation of Symmetry Code to Equiv.Pos

c = -x,1-y,1-z

Compound **11**			
Bond length(Å)		**Bond angle (°)**	
Pr1-ODMF	2.515(4)	ODMF-Pr1-O2	119.26(9)
Pr1-O2	2.602(3)	ODMF-Pr1-O3	73.18(10)
Pr1-O3	2.497(3)	ODMF-Pr1-O6	77.54(8)
Pr1-O6	2.418(2)	ODMF-Pr1-O7	128.53(11)
Pr1-O7	2.398(2)	ODMF-Pr1-O100	73.64(14)
Pr1-O100	2.509(5)	ODMF-Pr1-O5^{c}	141.25(11)
Pr1-O5^{c}	2.584(2)	ODMF-Pr1-O6^{c}	136.01(8)
Pr1-O6^{c}	2.612(2)	ODMF-Pr1-O8^{c}	73.76(12)
Pr1-O8^{c}	2.458(2)	O2-Pr1-O3	50.40(9)
		O2-Pr1-O6	147.15(9)
		O2-Pr1-O8	72.96(9)
		O2-Pr1-O100	76.25(13)
		O2-Pr1-O5^{c}	68.51(9)
		O2-Pr1-O6^{c}	104.27(8)
		O2-Pr1-O8^{c}	138.43(11)
		O3-Pr1-O6	121.24(8)
		O3-Pr1-O7	85.51(10)
		O3-Pr1-O100	80.25(13)
		O3-Pr1-O5^{c}	117.19(8)
		O3-Pr1-O6^{c}	149.14(9)
		O3-Pr1-O8^{c}	140.48(10)
		O6-Pr1-O7	74.73(8)
		O6-Pr1-O100	136.52(13)
		O5^{c}-Pr1-O6	117.59(7)
		O6-Pr1-O6^{c}	68.42(7)
		O6-Pr1-O8^{c}	70.97(9)
		O7-Pr1-O100	148.42(14)
		O5^{c}-Pr1-O7	90.19(10)
		O6^{c}-Pr1-O7	68.22(8)
		O7-Pr1-O8^{c}	132.72(9)
		O5^{c}-Pr1-O100	71.96(13)
		O6^{c}-Pr1-O100	113.79(13)
		O8^{c}-Pr1-O100	70.12(13)
		O5^{c}-Pr1-O6^{c}	50.08(7)
		O5^{c}-Pr1-O8^{c}	78.20(12)
		O6^{c}-Pr1-O8^{c}	69.42(9)

Translation of Symmetry Code to Equiv.Pos

c 1-x,1-y,1-z

Table S5. Hydrogen bonding for compounds **9-11**

D-H···A (Å)	d(D-H) (Å)	d(H-A) (Å)	d(D···A) (Å)	∠DHA (°)	Symmetry transform
Compound **9**					
C9–H9···O2	0.930	2.430	2.766 (7)	101.00	
C14–H14···O2	0.930	2.390	3.192 (8)	144.00	-1+x, y, z
C15–H15···O8	0.930	2.490	3.10 (2)	123.00	2-x,1-y,1-z
C22–H22A···O4	0.970	2.530	3.521 (9)	131.00	1-x,1-y,1-z
Compound **10**					
C14–H14···O5	0.930	2.55	3.331(6)	142.00	1-x,1-y,1-z
C14–H14···O2	0.930	2.380	3.175 (6)	144.00	1+x,y,z
C15–H15···O8	0.930	2.490	3.10 (2)	123.00	2-x,1-y,1-z
C22–H22B···O4	0.970	2.580	3.244 (9)	126.00	1-x,1-y,1-z
Compound **11**					
C1–H1···O2	0.930	2.38	3.191(6)	146.00	1+x,y,z
C5–H5···O2	0.98(5)	2.31(5)	2.735(4)	105(4)	1-x,-y,2-z
C12–H12B···O1	0.9700	2.5100	3.220(6)	130.00	
C15–H15···O8	0.9300	2.4500	3.077(13)	125.00	1-x,1-y,1-z

Table S6: UV-Vis investigations

Sl No:	Compound	Wavelength (nm)	Optical transition
UV-Vis			
1	Ligand	278 340	π-π* n-π*
2	Compound **1-11**	~280 320-350	π-π* n-π*
3	Compound **2,3** Compound **2** Compound **3**	~270 330-350 448, 473, 486, 592, 735, 743, 751, 796 512, 523, 576, 583, 680, 692, 733, 742, 752, 795	π-π* n-π* *f-f* transitions *f-f* transitions

Table S7: List of important IR bands observed in **1-10**

Compound	ν(≡C–H) (cm^{-1})	ν(C≡C) (cm^{-1})	ν(COO) (cm^{-1})	$\nu(O–H)_{str}$ coordinated H_2O (cm^{-1})	ν(C=O) DMF
2,5 BPTA	~3261	~2126	~1693	-	
Compound **1-8**	~3277	~2119	~1577	~3400-3500	
Compound **9-11**	~3280	~2119	~1554	~3434-3480	~1650

Table S8: CIE chromaticity coordinates (x, y) for $Y_{0,98-x}Tb_{0.02}Eu_x$– MOF material samples with different Eu3+ concentrations ($0 < x < 4.0$)

Sample code	CIE X	CIE Y	CCT(K)
A_Y1 (0% Eu)	**0.306**	**0.412**	**6354**
A_Y2 (0.5 % Eu)	**0.319**	**0.373**	**6011**
A_Y3 (1.0 % Eu)	**0.329**	**0.361**	**5636**
A_Y4 (2.0 % Eu)	**0.334**	**0.346**	**5432**
A_Y5 (3.0 % Eu)	**0.361**	**0.335**	**4316**
A_Y6 (4.0 % Eu)	**0.42**	**0.326**	**2521**

LOD calculation:

The luminescence intensity of the compound was plotted as a function of cation concentration. The limit of detection (LOD) is given by: LOD = 3σ/m, where σ is the standard deviation of the blank measurements without adding the anion and m is the slope of the linear plot.

Table **S9**. Standard deviation and detection limit calculation for Cr^{3+} and Fe^{3+}

Blank readings of **7** (without analyte)	Luminescence intensity	Standard deviation (σ)	Slope from the graph (m)	Detection limit (3σ/m)	Limit of detection (LOD) (ppm)
Cr^{3+}					
Reading 1	1165687	2245.78	4.11×10^{6} mM^{-1}	1.78×10^{-3} mM	0.41
Reading 2	1168213				
Reading 3	1161425				
Reading 4	1165224				
Reading 5	1167680				
Fe^{3+}					
Reading 1	1188582	2327	1.9×10^{5} mM^{-1}	0.036 mM	8.6
Reading 2	1186724				
Reading 3	1182143				
Reading 4	1183462				
Reading 5	1184128				

Table S10

Variation of bases at different temperatures for O Arylation reaction[a]:

[a]**Reaction Conditions:** methyl 4-bromobenzoate (1 mmol), Phenol (1 mmol), Base (1.5 mmol), catalyst (0.007 mol%), DMF (2 mL) 5h, yield based on column chromatography

Entry	Base	Temperature	% Yield
1	CH_3COONa	80	trace
2	^tBuOK	80	35
3	DABCO	80	25
4	Na_2CO_3	80	84
5	K_2CO_3	80	87
6	**Cs_2CO_3**	**80**	**95**
7	Cs_2CO_3	50	27
8	Cs_2CO_3	60	49
9	Cs_2CO_3	70	69

Table S11: Solvent Optimisation for O Arylation reaction[a]

[a]**Reaction Conditions:** methyl 4-bromobenzoate (1 mmol), Phenol (1 mmol), Base (1.5 mmol), catalyst (5 mg, 0.007 mol%), Solvent (2 mL) 80 deg yield based on column chromatography

Entry	Solvent	Time (h)	% Yield
1	Methanol	12	54
2	Ethanol	12	39
3	DMSO	12	79
4	Toluene	12	18
5	**DMF**	**5**	**95**
6	Dioxane	12	42
7	Water	12	~10

Table S12: Catalyst Optimisation for O Arylation reaction[a]

Catalyst stabilization:

Catalyst (5mg)	Yield (%)
$Tb(NO_3)_3.xH_2O$	25
$Ce(NO_3)_3.xH_2O$	21
Tb-MOF	95
Ce-MOF	89

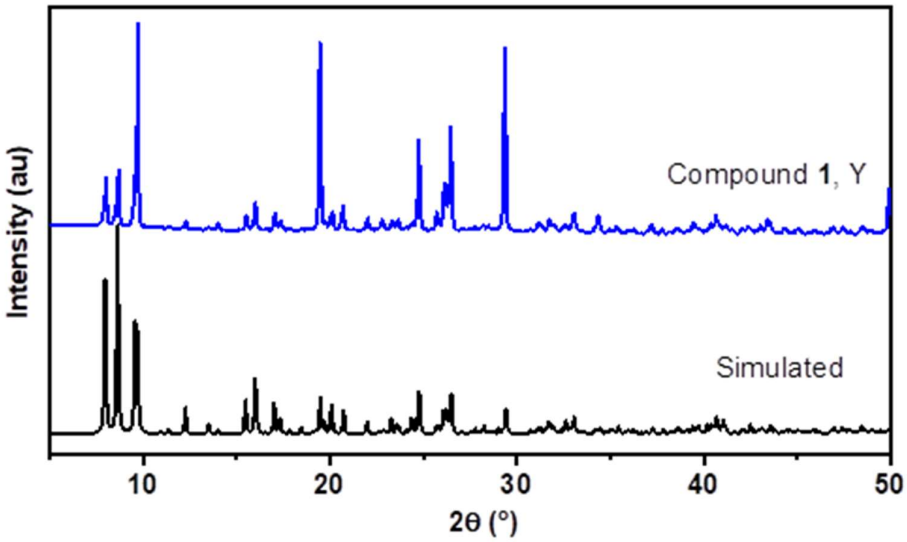
Intensity (au)
Compound 1, Y
Simulated
10
20
30
40
50
2θ (°)

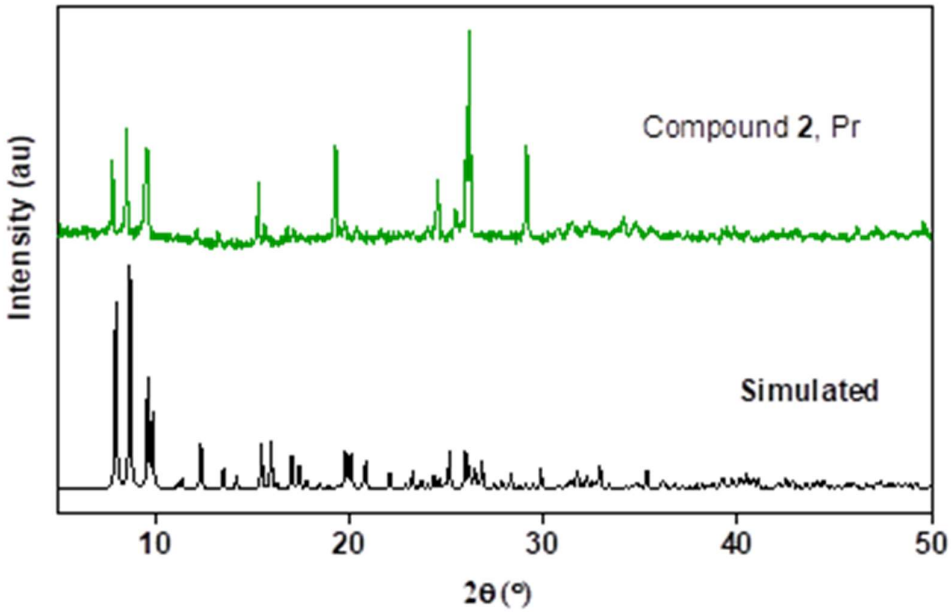
Intensity (au)
Compound 2, Pr
Simulated
10
20
30
40
50
2θ (°)

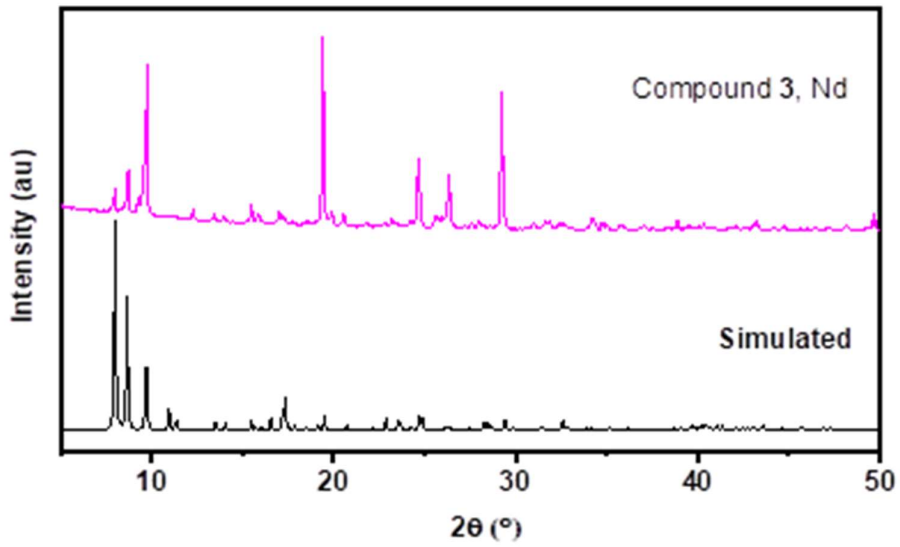
Compound 3, Nd
Simulated
Intensity (au)
10
20
30
40
50
2θ (°)

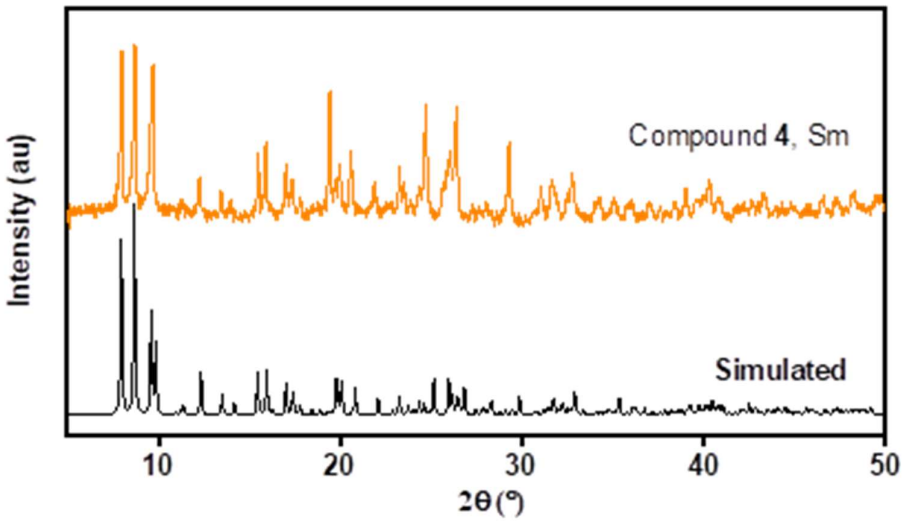
Compound 4, Sm
Simulated
Intensity (au)
10
20
30
40
50
2θ (°)

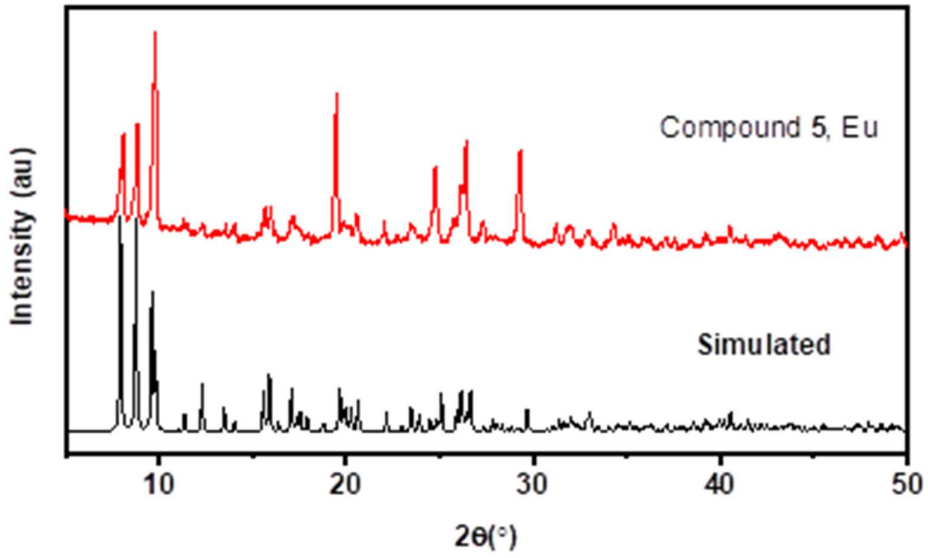
Compound 5, Eu
Simulated
Intensity (au)
10
20
30
40
50
2θ(°)

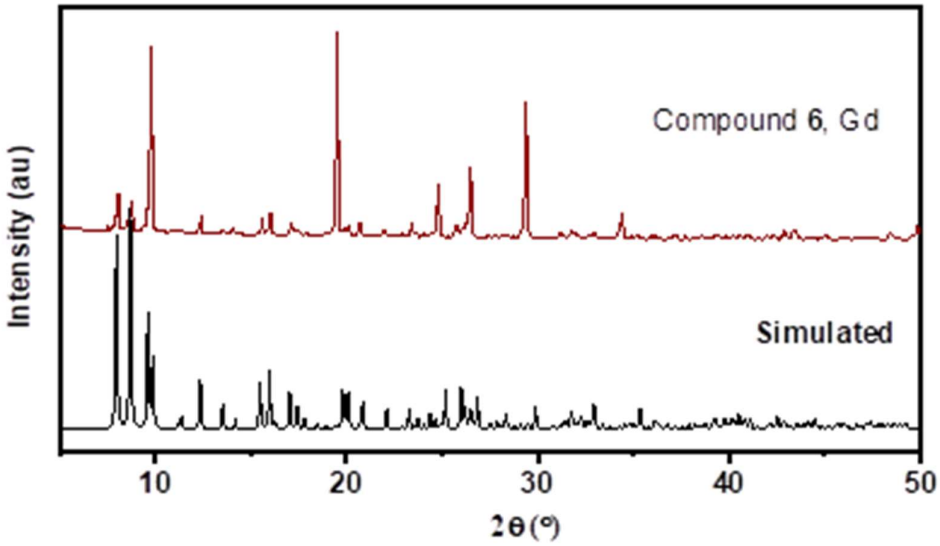
Compound 6, Gd
Simulated
Intensity (au)
10
20
30
40
50
2θ(°)

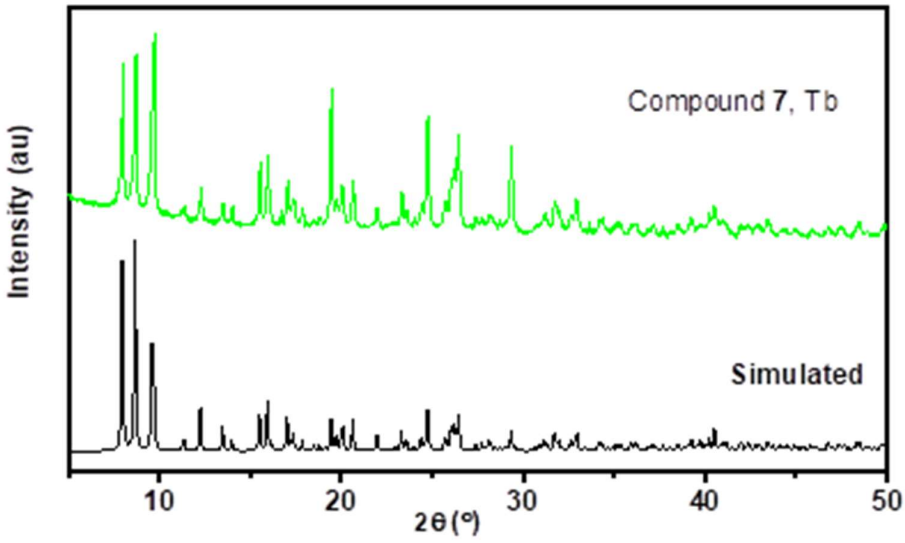
Compound 7, Tb
Simulated
Intensity (au)
10
20
30
40
50
2θ (°)

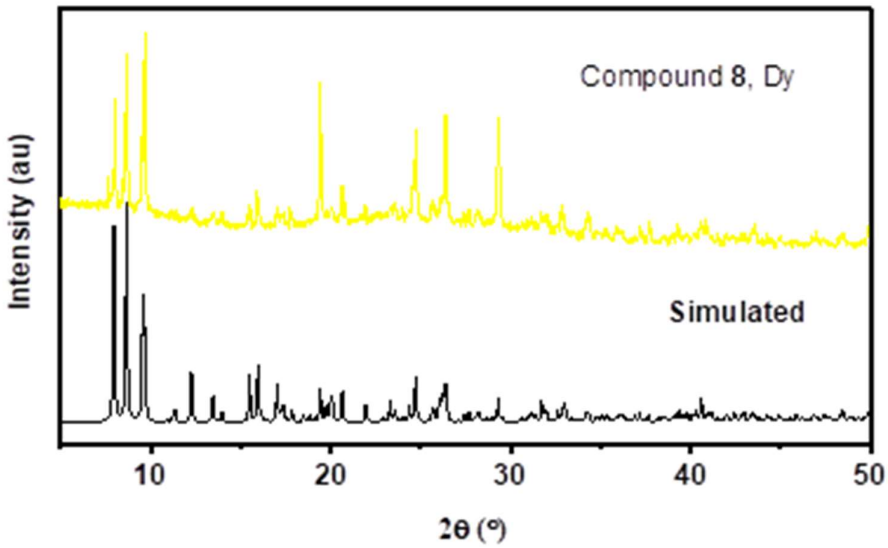
Compound 8, Dy
Simulated
Intensity (au)
10
20
30
40
50
2θ (°)

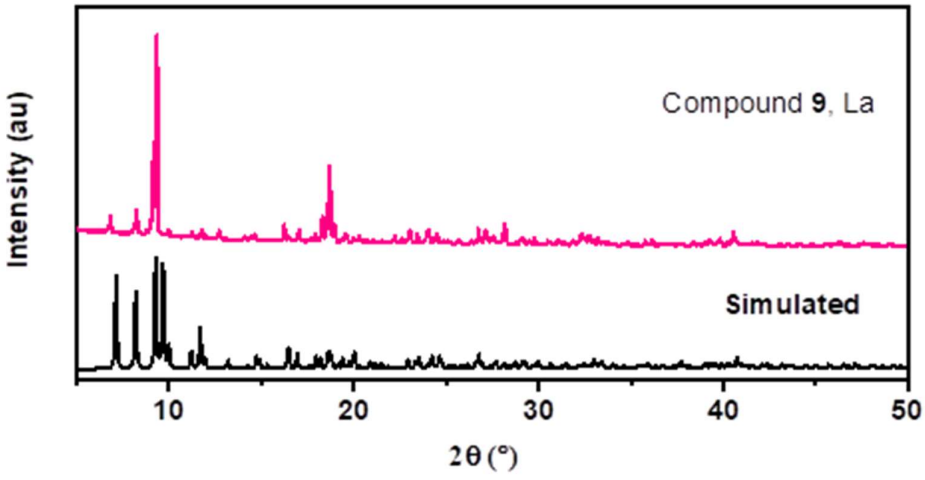
Compound 9, La
Simulated
Intensity (au)
10
20
30
40
50
2θ (°)

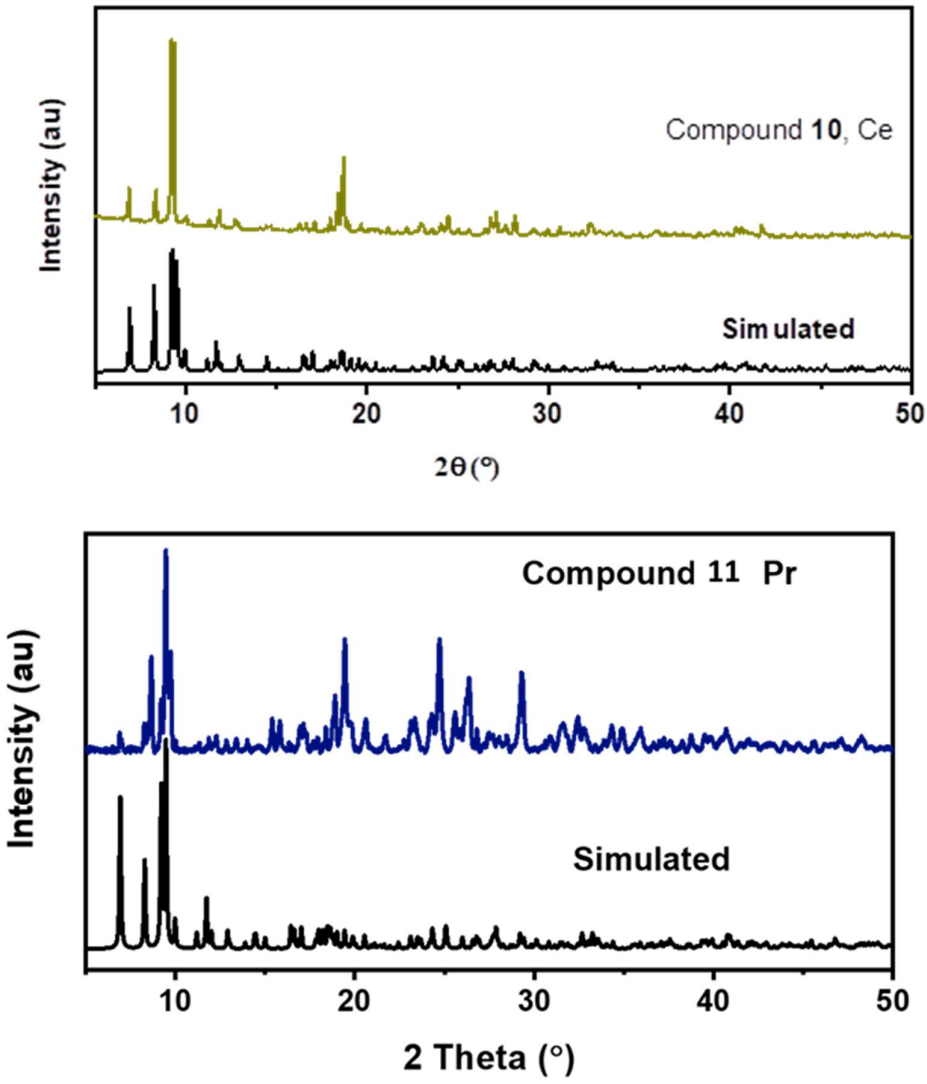

Figure S1. Experimental and simulated PXRD patterns of Compound **1-10**

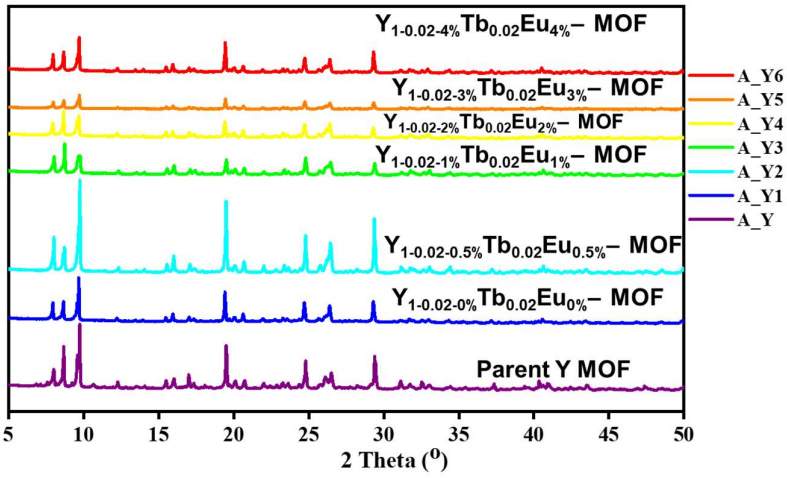

Figure S2: PXRD patterns of $Y_{0.98-x\%}Tb_{0.02}Eu_{x\%}$– MOF samples, confirming the structural integrity

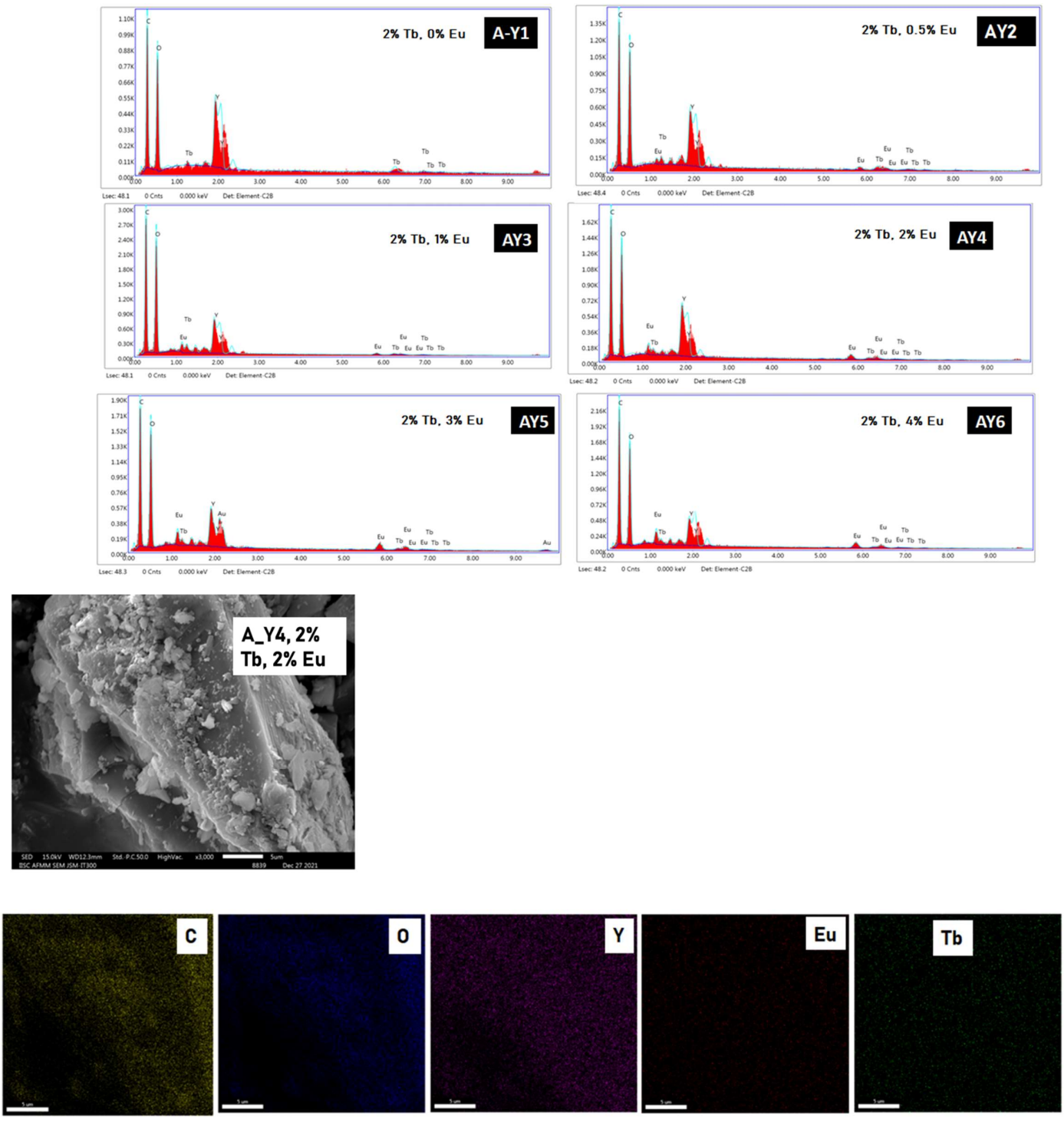

Figure S3: EDX mapping of all dopped Y MOFs, SEM image of 2%Tb, 2% Eu, Y MOF and corresponding elemental mapping.

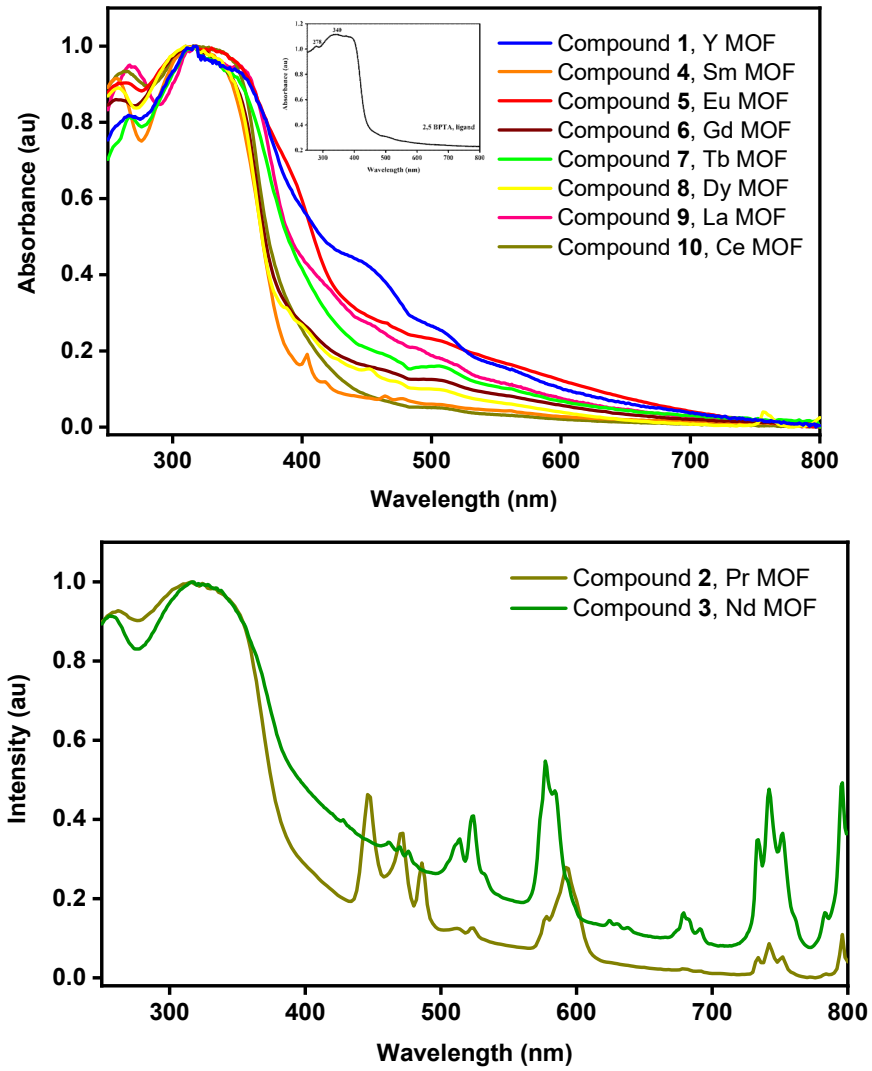

Figure S4. The solid-state UV−Vis absorption spectrum of compound 1-10.

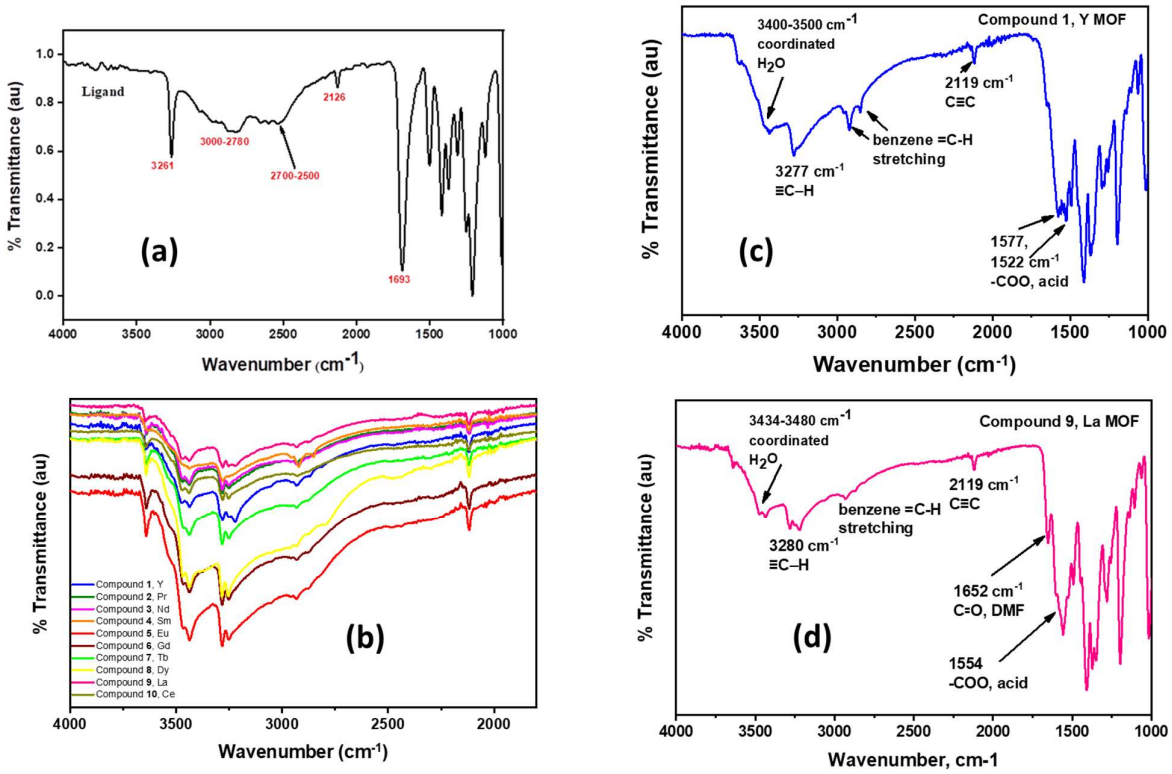

Figure S5: (a) Infrared spectra of 2,5 BPTA, (b) Infrared Spectra of Compound **1-10 (c)** Infrared spectra of compound **1 (d)** Infrared spectra of compound **2**.

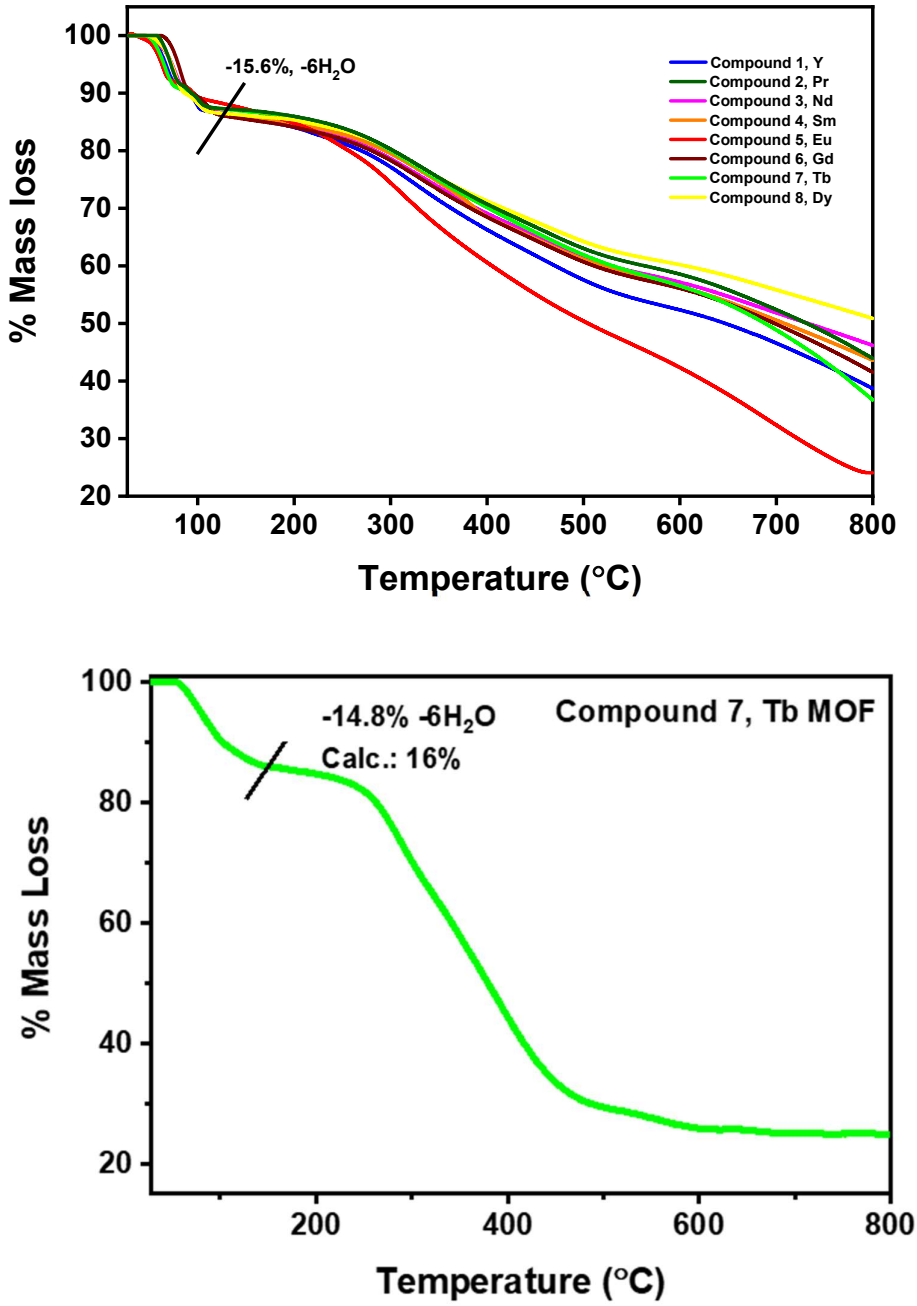

Figure S6. TGA plot of 2D compounds, Compounds **1 -8**

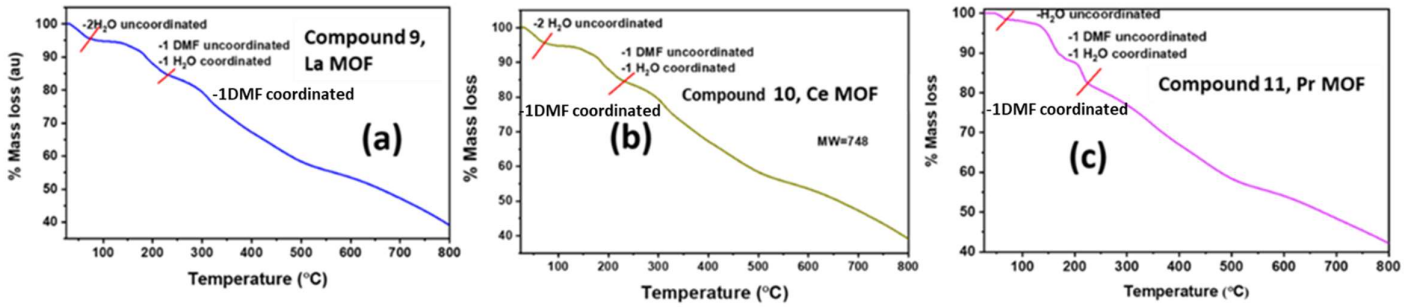

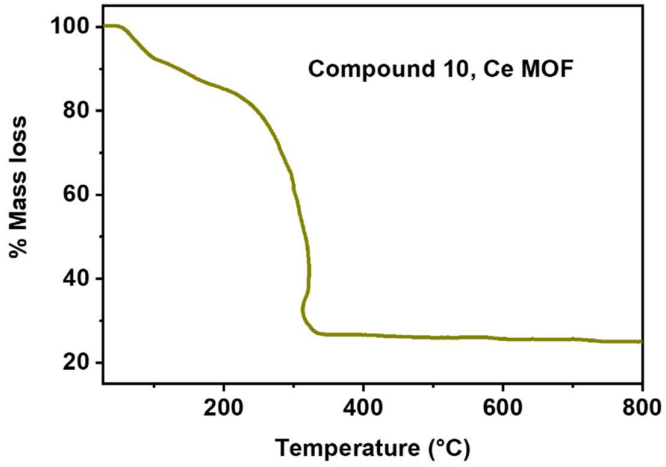

Figure S7. TGA plot of 3D Compound **9-11 (a), (b)** and **(c).**

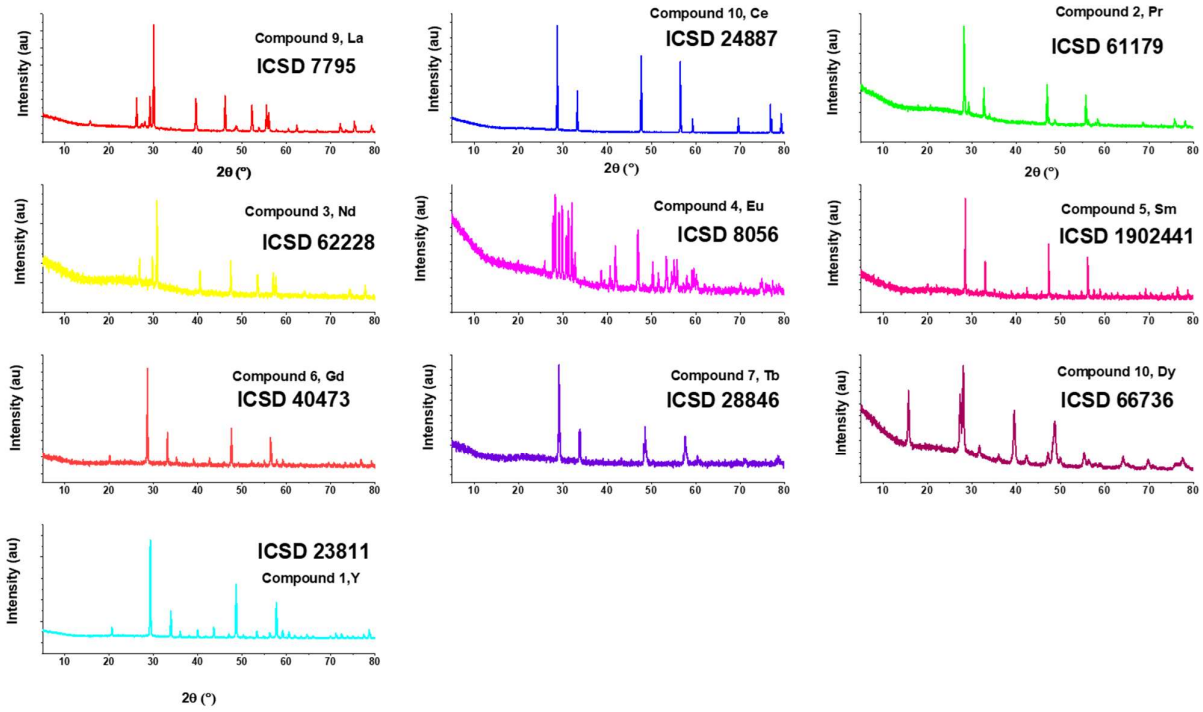

Figure S8: PXRD of all MOF after TGA analysis

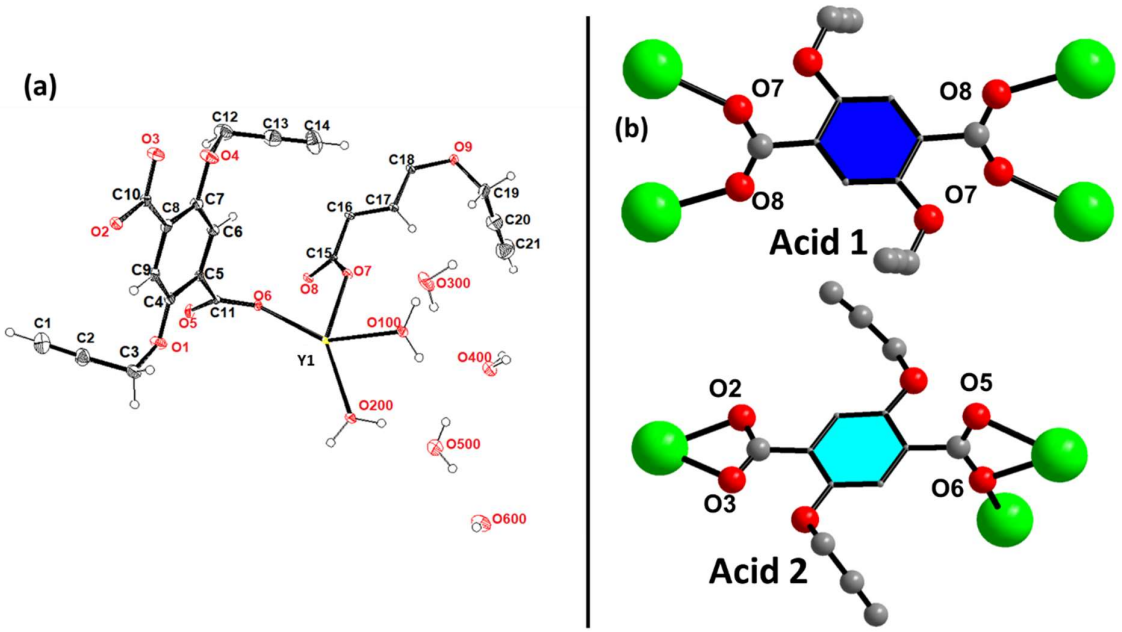

Figure S9: (a) Asymmetric unit of **Y** (Thermal ellipsoid with 50% probability); (b) The various coordination modes of the 2, 5 BPTA anions in Y MOF, acid 1 and acid 2

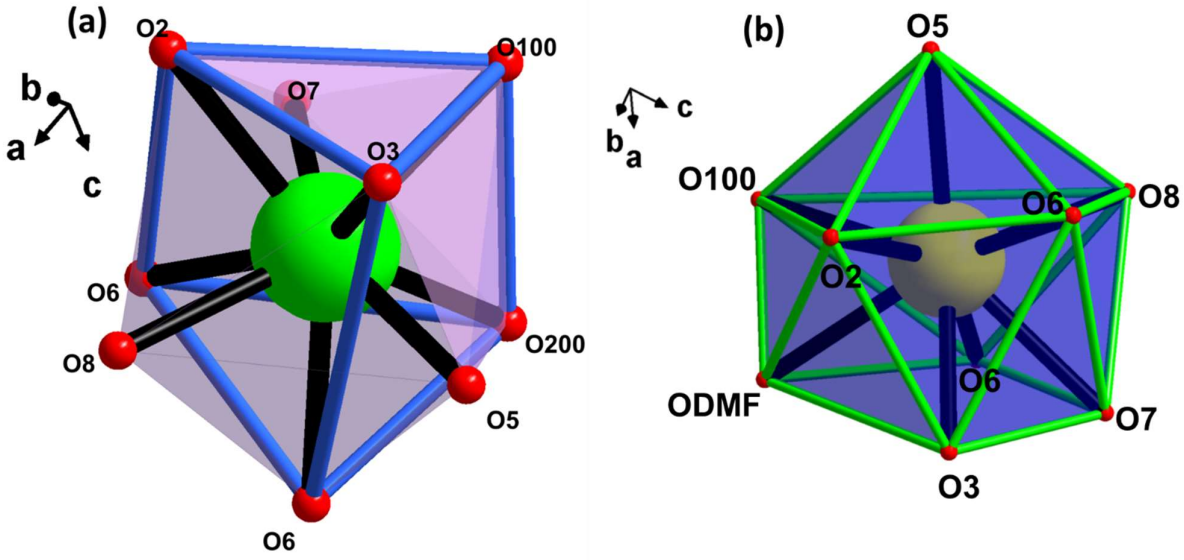

Figure S10: Metal coordination of **Y MOF** $[Y(C_{14}H_8O_6)(C_7O_3H_4)\cdot 2H_2O]\cdot 4(H_2O)$ tricapped trigonal prismatic **(a)** and **La MOF** $[La(C_7O_3H_4)_3.(C_3H_7ON).(H_2O)]\cdot 2(H_2O)(C_3H_7NO)$ capped square antiprismatic **(b)**

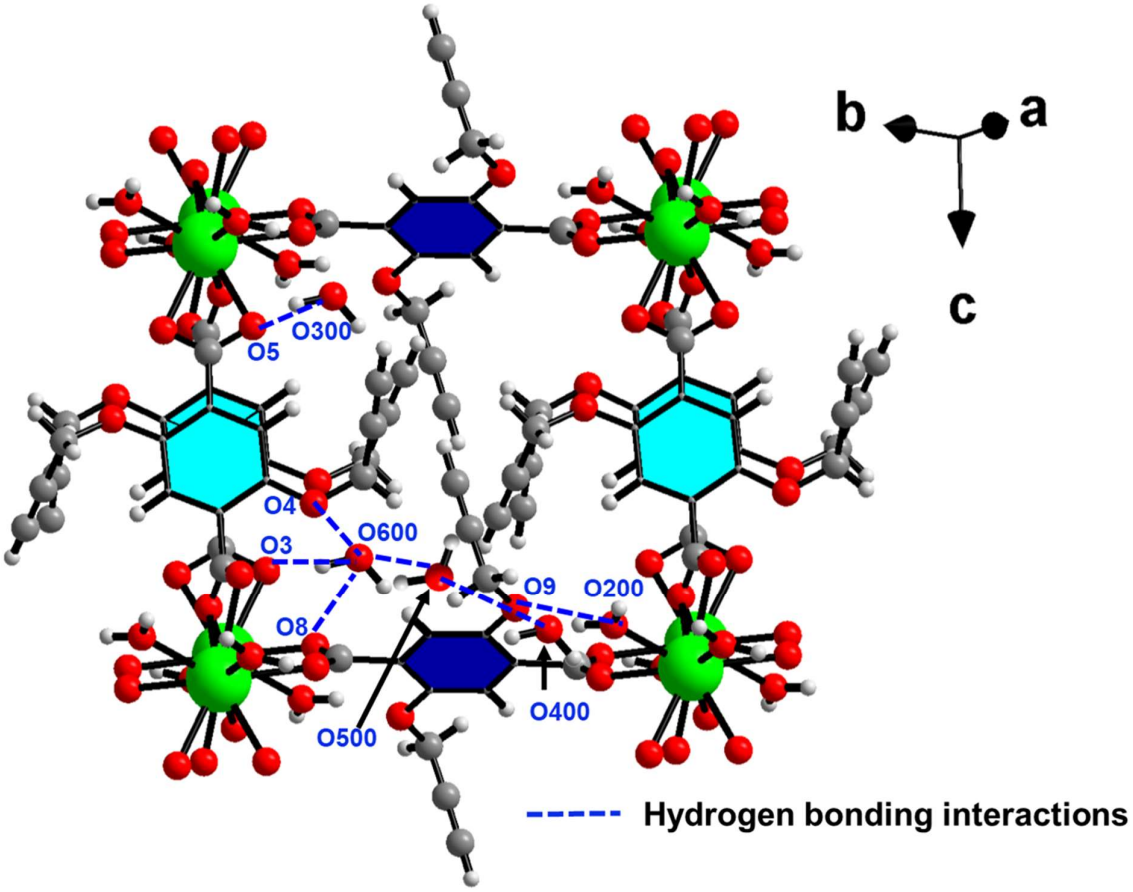

Figure S11: The coordinated and lattice water molecule interactions with layers.

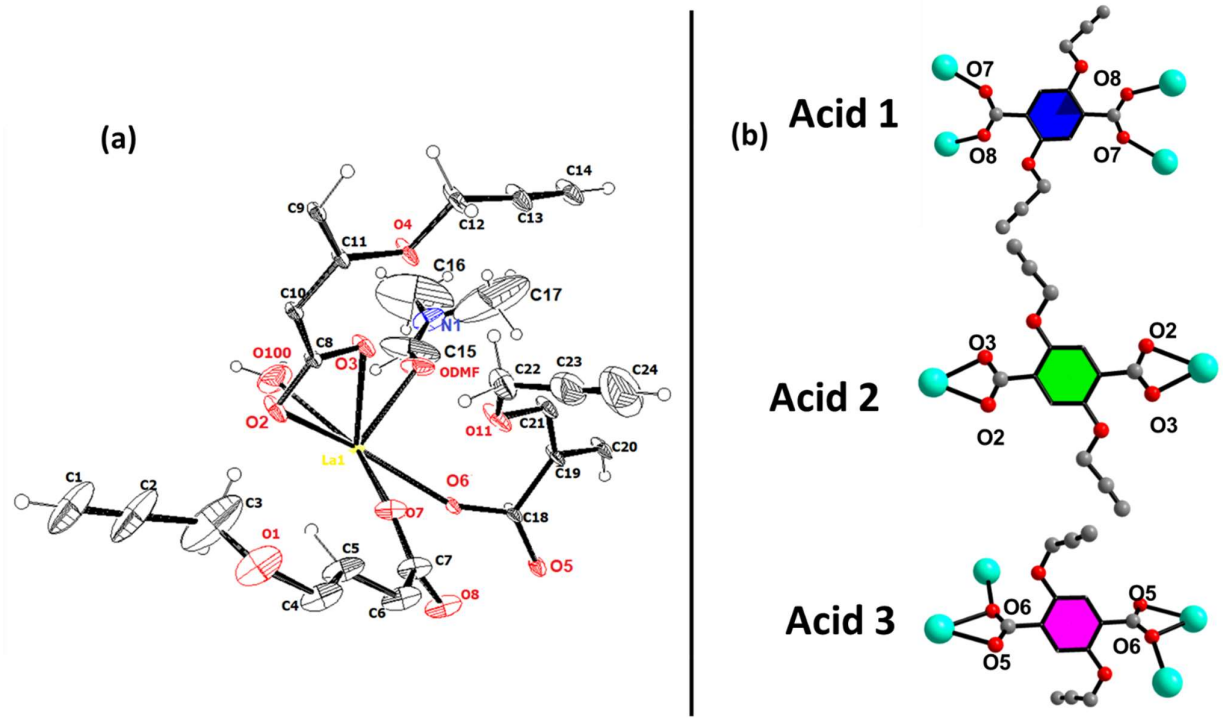

Figure S12: (a) Asymmetric unit of **La** (Thermal ellipsoid with 50% probability); (b) The various coordination modes of the 2, 5 BPTA anions in La MOF, acid 1, acid 2 and acid 3

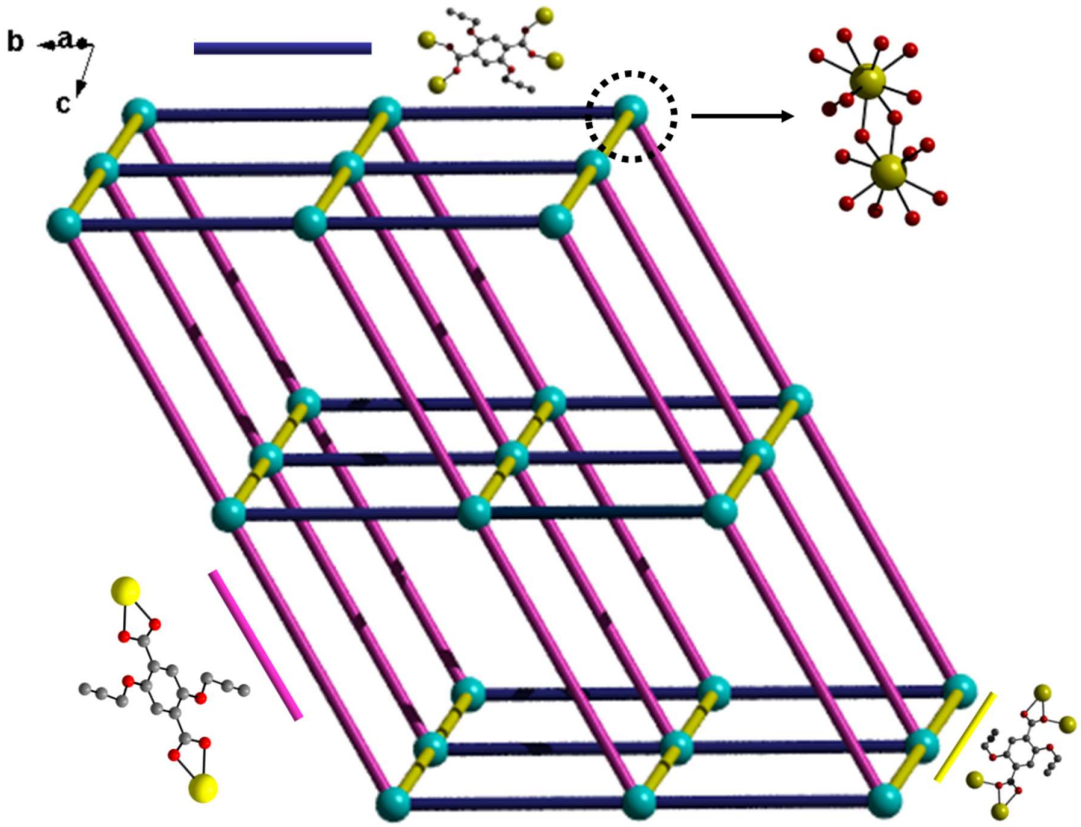

Figure S13: Simplified structure of **9**, La MOF

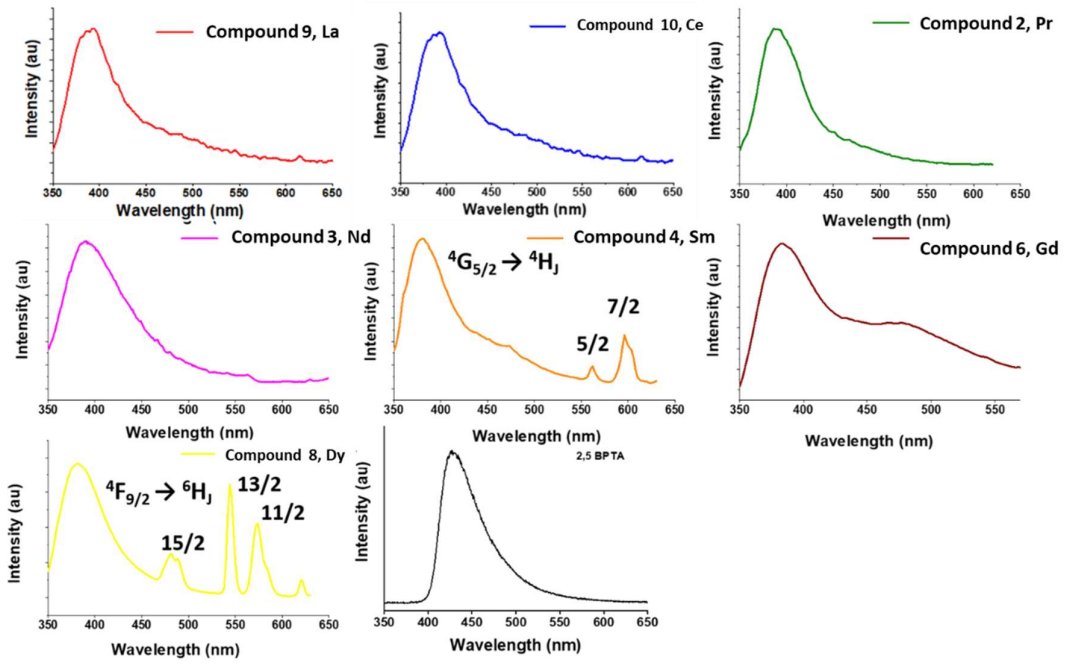

Figure S14: Room-temperature photoluminescence spectra for 2, 3, 4, 6, 8, 9, 10 and 2, 5 BPTA

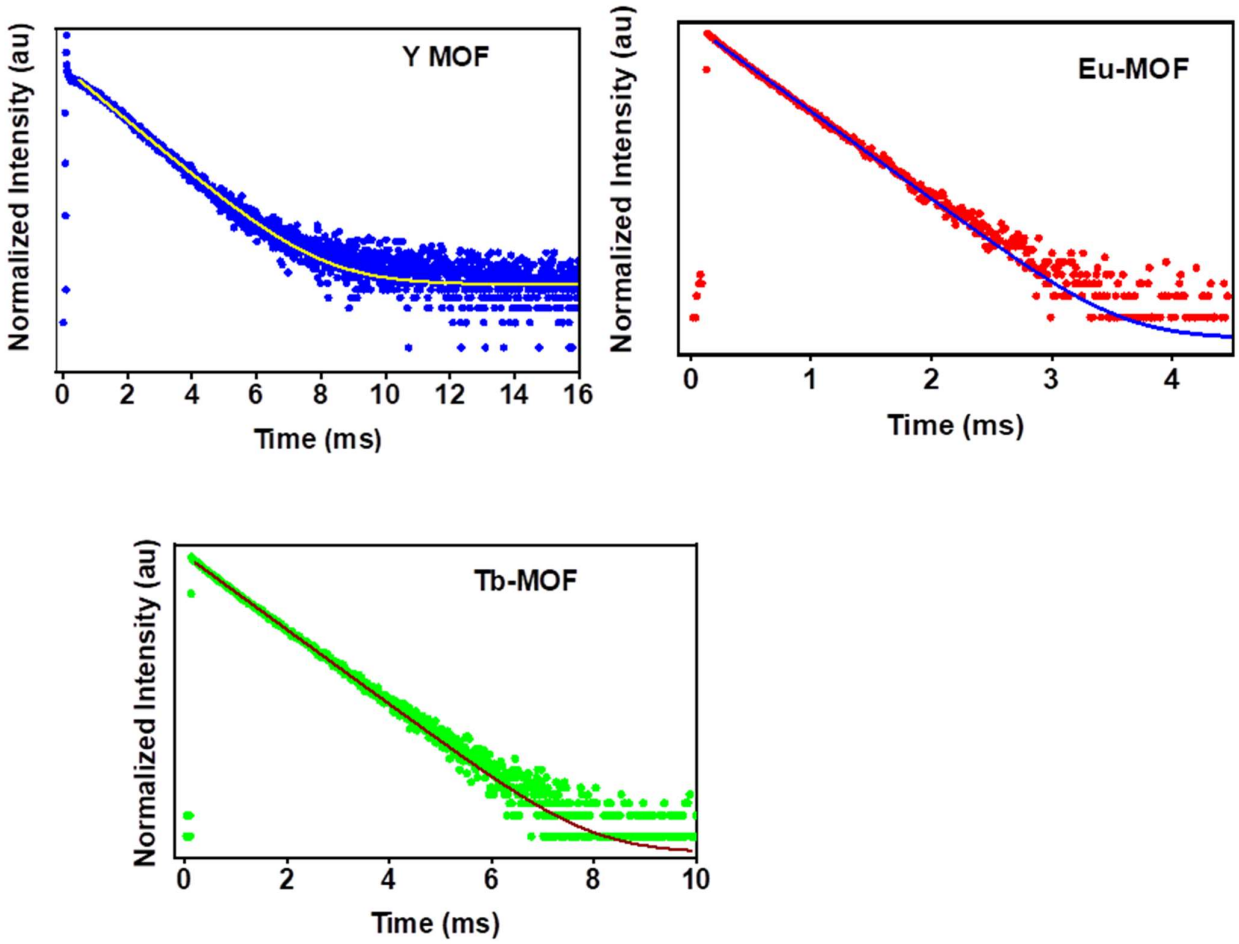

Figure S15: Luminescence decay profiles (298K) for Y , Eu and Tb MOFs.

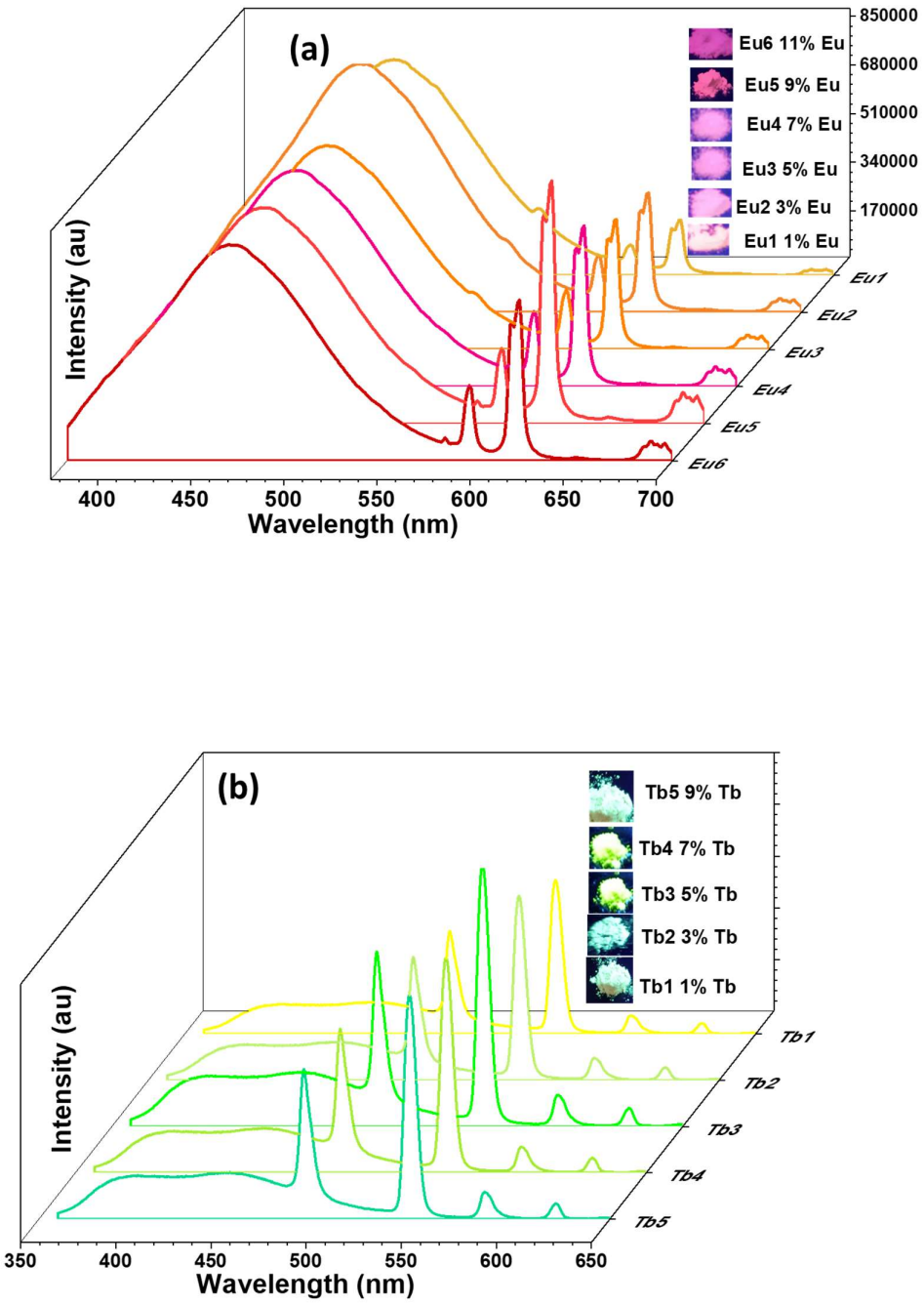

Figure S16: Different substitution of Eu^{3+} **(a)** and Tb^{3+} **(b)** in Y-MOF

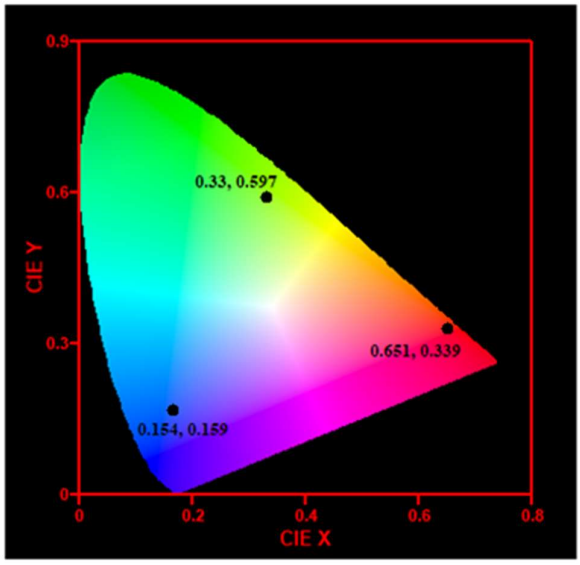

Figure S17: CIE color coordinate diagram of Y MOF doped with 5% Tb^{3+}, and 9% Eu^{3+} and Y MOF.

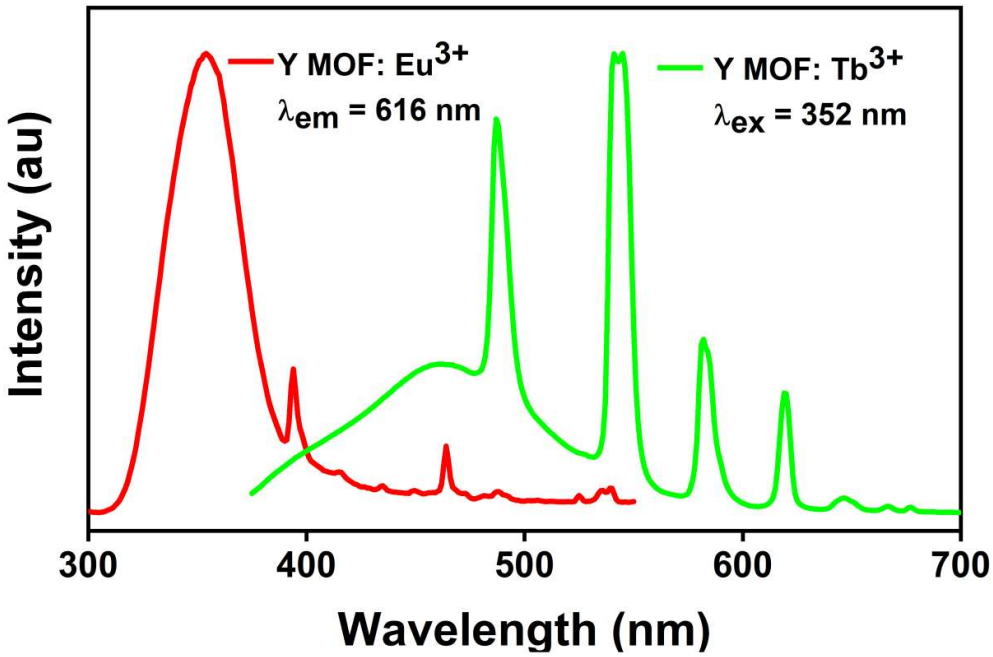

Figure S18: The spectral overlap between the PLE spectrum of Y-MOF: Eu^{3+} and PL spectrum of Y-MOF:Tb^{3+} materials.

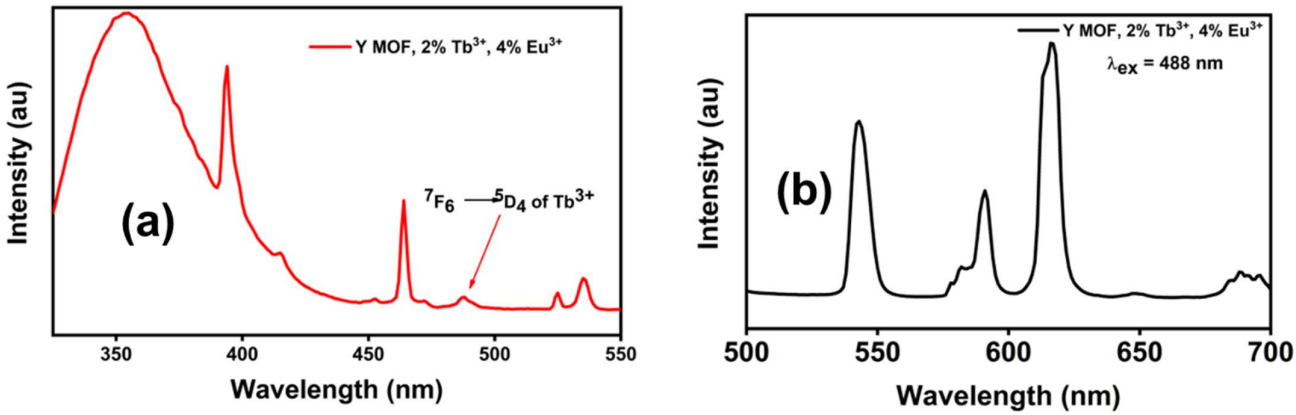

Figure S19: a) The excitation spectrum of Y-MOF, 2% Tb^{3+}, 4% Eu^{3+} sample monitored at 619 nm; b) The emission spectrum of the sample at the excitation of 488nm

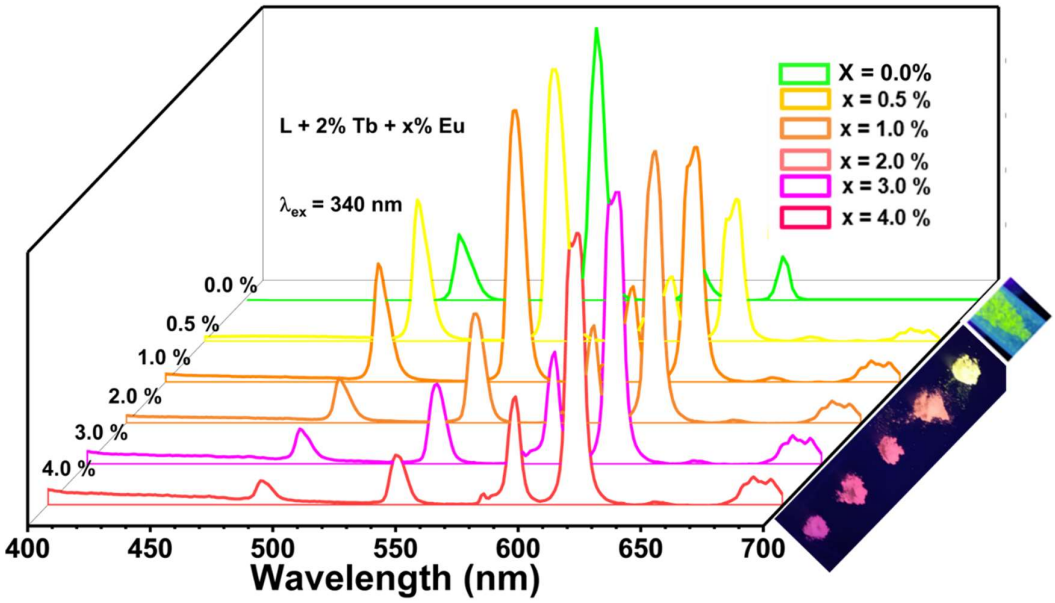

Figure S20: PL emission spectra (λ_{ex} = 340 nm) of 2,5 BPTA + 2% Tb^{3+} + x% Eu^{3+} samples with different Eu^{3+} concentrations (0 < x < 4.0).

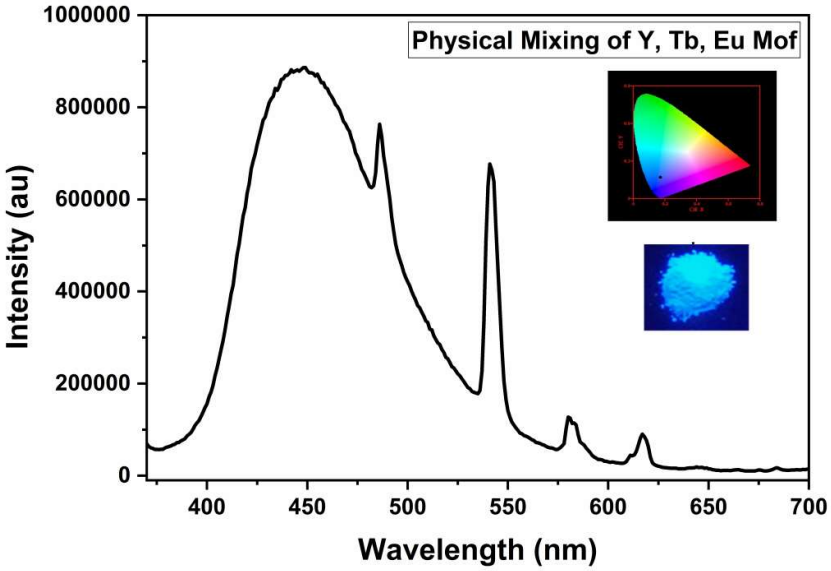

Figure S21: The PL spectra of the Physical mixing of Y MOF, 2% Tb MOF and 2% Eu MOF. (Inset showing the dominating blue colour under the 365 nm UV radiation and corresponding CIE diagram)

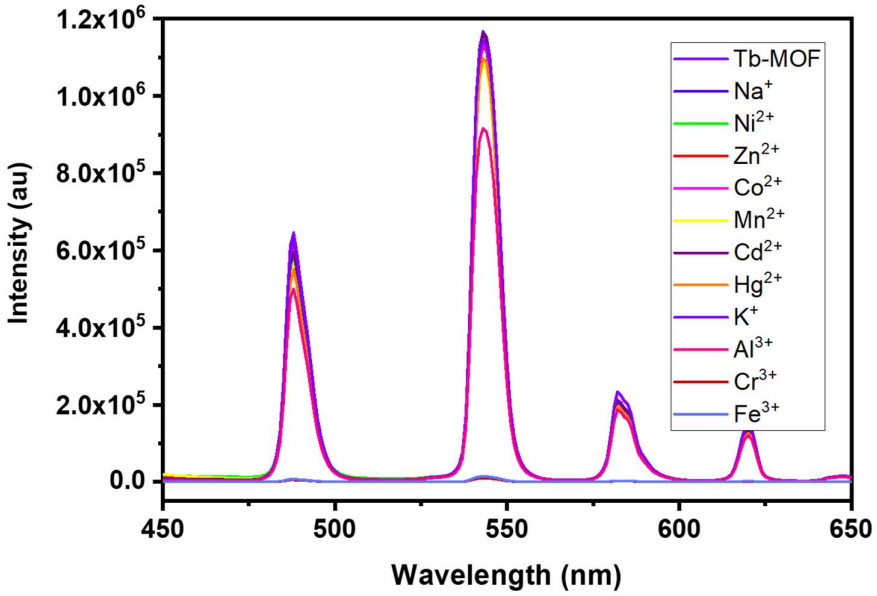

Figure S22: The luminescence intensity of Tb-MOF in presence of different cations (5×10^{-4} M)

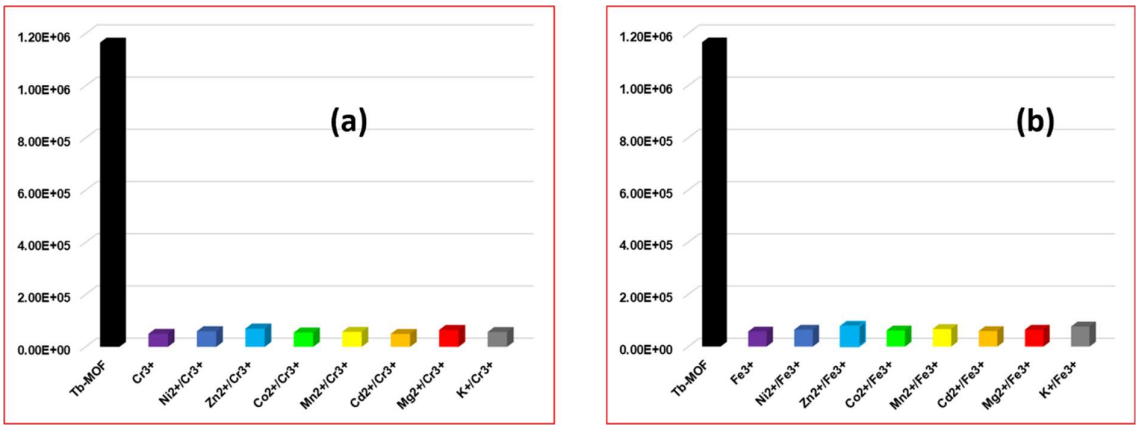

Figure S23. Comparison of the luminescence quenching effect of (a) Cr^{3+} and (b) Fe^{3+} ion Tb-MOF is presence of other competitive cations (5 x 10^{-4} M).

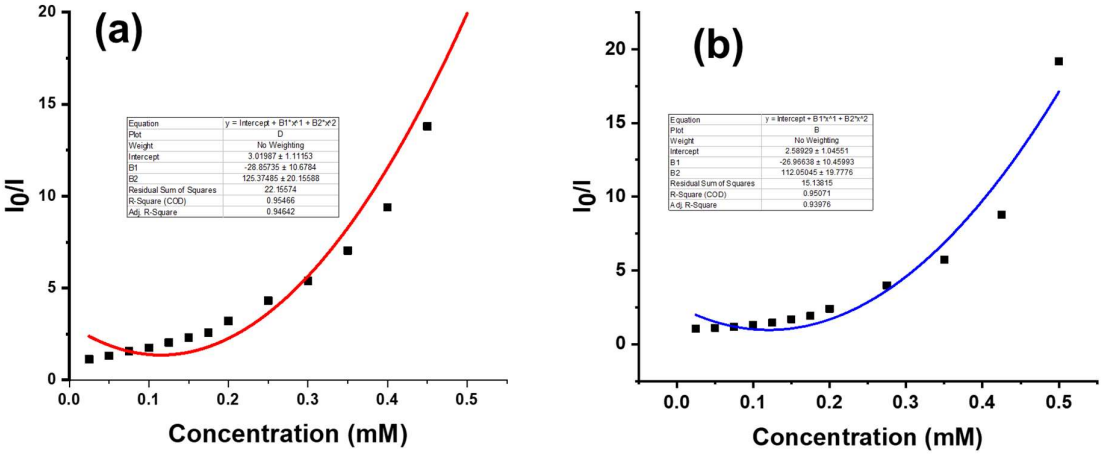

Figure. S24. Stern-Volmer plots for **7** at high concentration of (a) $Cr^{3+}$and (b) Fe^{3+}

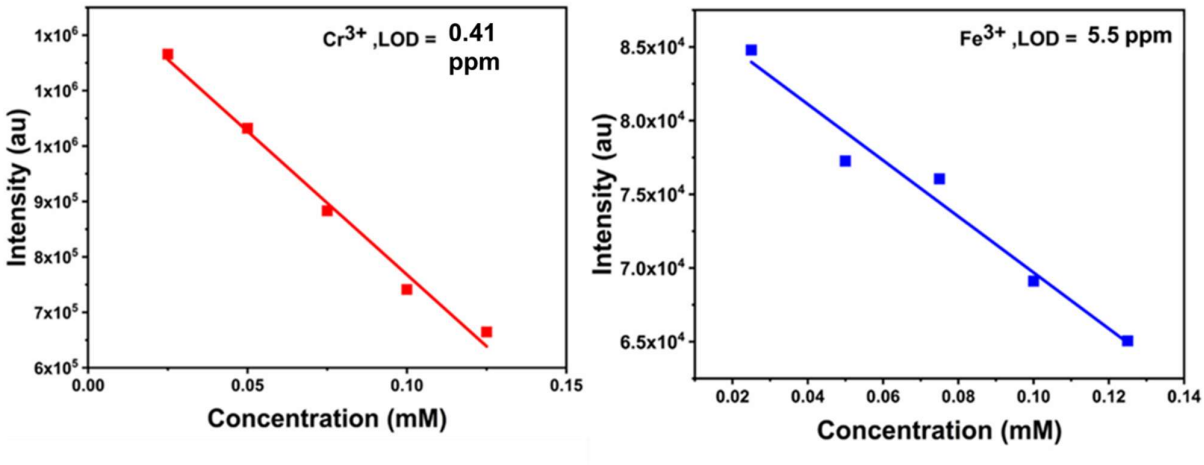

Figure S25: The LOD calculation graph for Cr^{3+} and Fe^{3+}

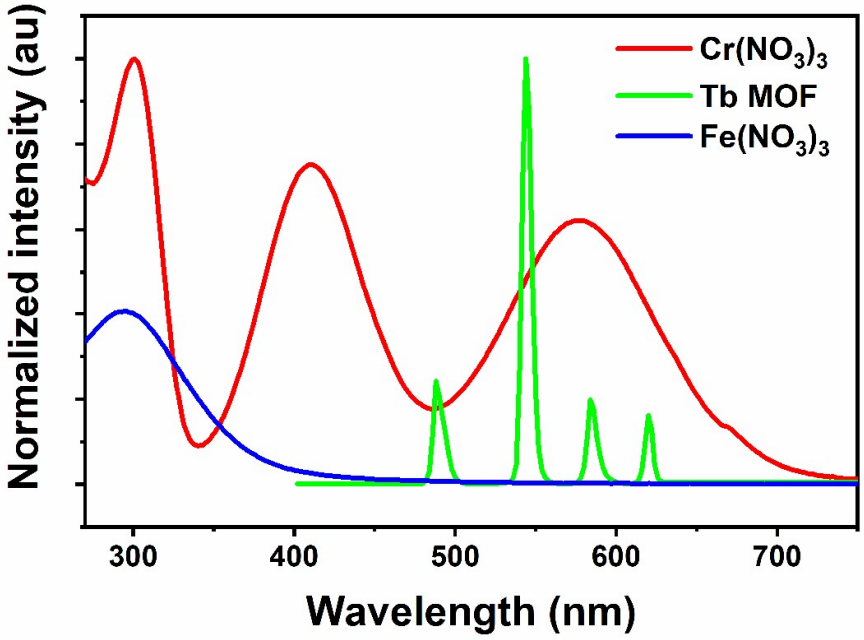

Figure S26: The absorption bands of analytes along with the emission spectra of Tb MOF. Note the considerable overlap (see text).

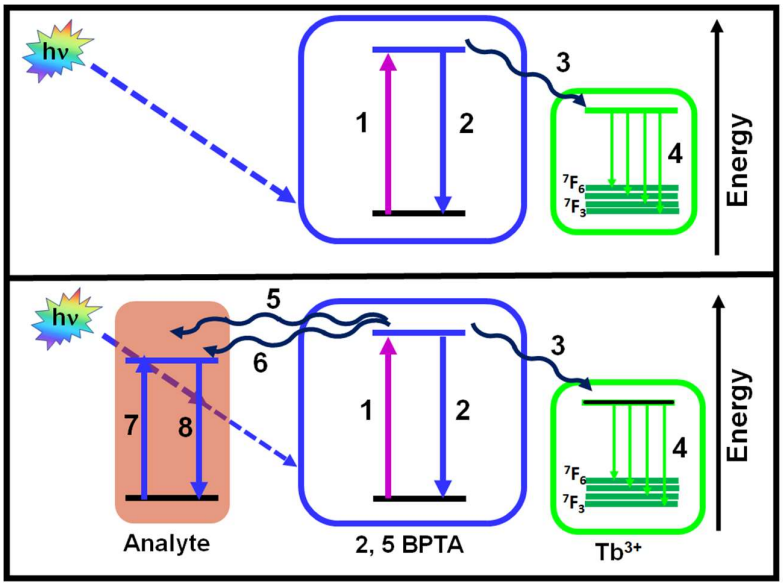

Figure S27: Schematic of various energy/electron transfer processes in the absence of analyte (upper panel) and in the presence of analyte (lower panel): (1) UV light excited ligand centre; (2) ligand based luminescence; (3) energy transfer from ligand to Tb^{3+} ions; (4) emission from Tb^{3+} ions; (5) energy transfer from ligand to analyte; (6) electron transfer from ligand to analytes; (7) absorption of UV light by the analyte; (8) analyte based luminescence. Presence of analyte absorbs a part of *hv*, as well as reduces (due to (5) and (6)) the flow of energy from the ligand centre to the metal centre, resulting in a large quenching of luminescence.

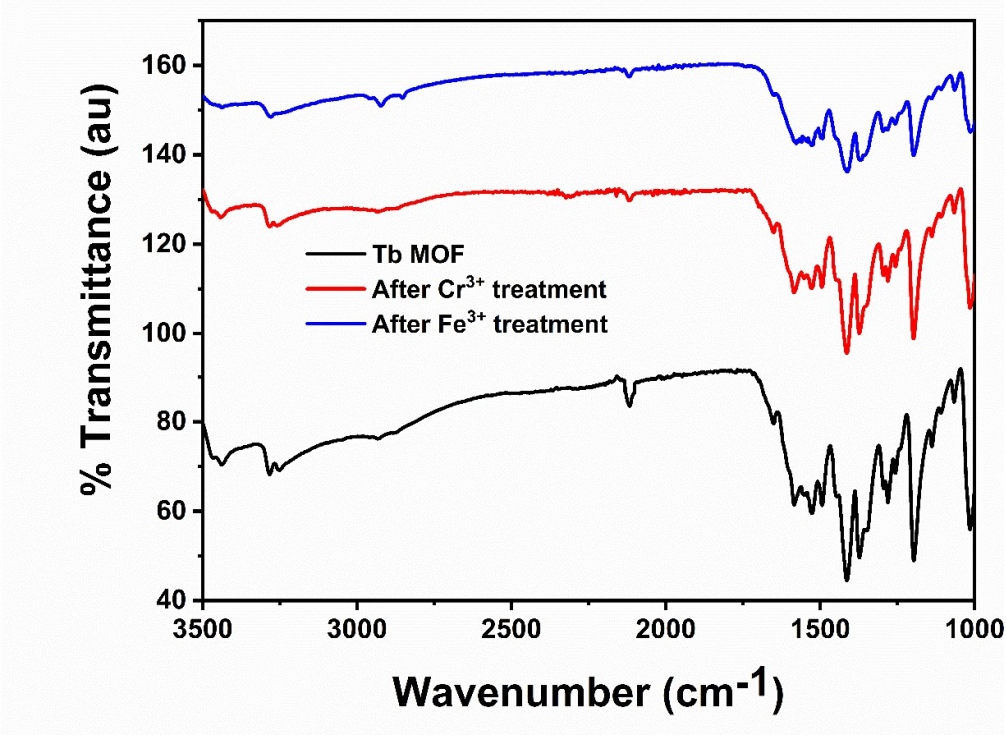

Figure S28: IR titration of compound **7** upon the gradual addition of Cr^{3+} and Fe^{3+} up to 0.5 mM, respectively.

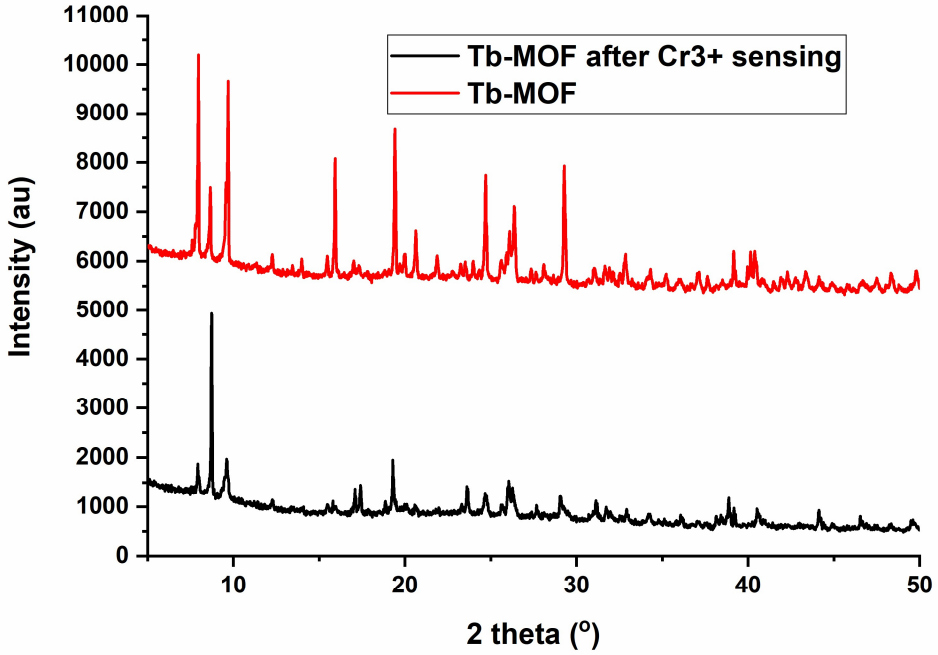

Figure S29: The PXRD study was carried out after the sensing studies, which indicated the structural integrity of compound **7**

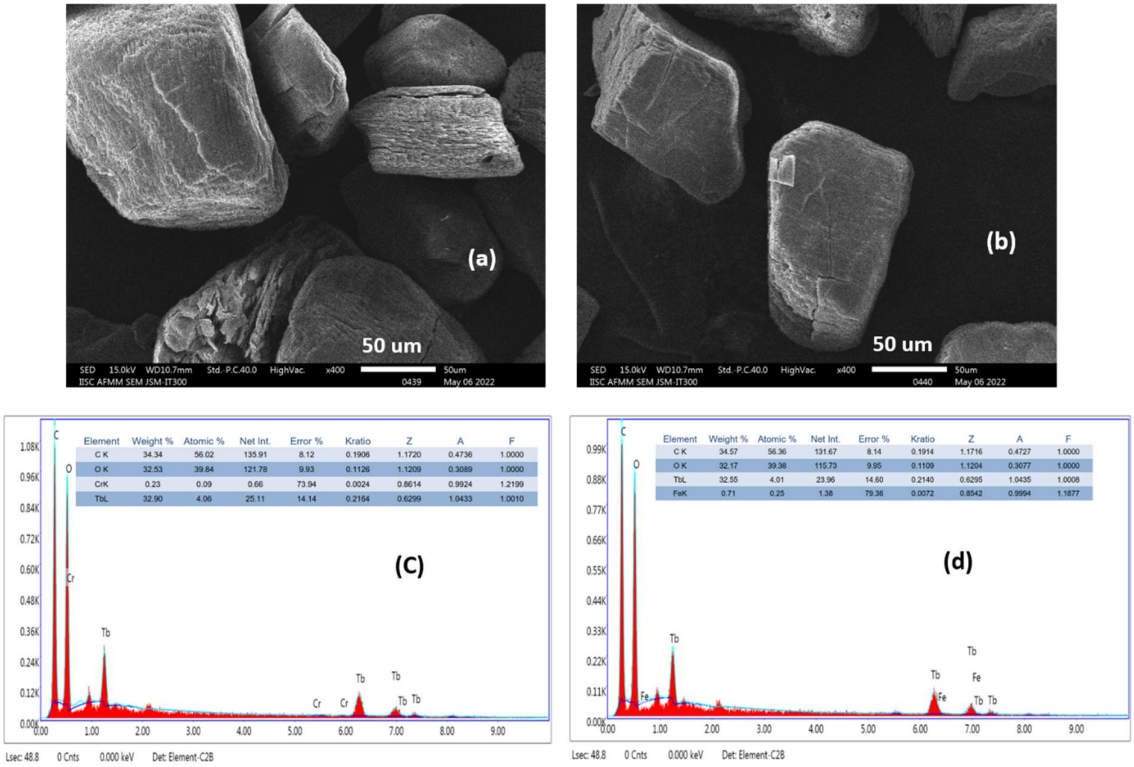

Figure S30: The SEM-EDX images after the sensing studies of Cr^{3+} (a and c) and Fe^{3+} (b and d)which indicated the structural integrity of compound **7**

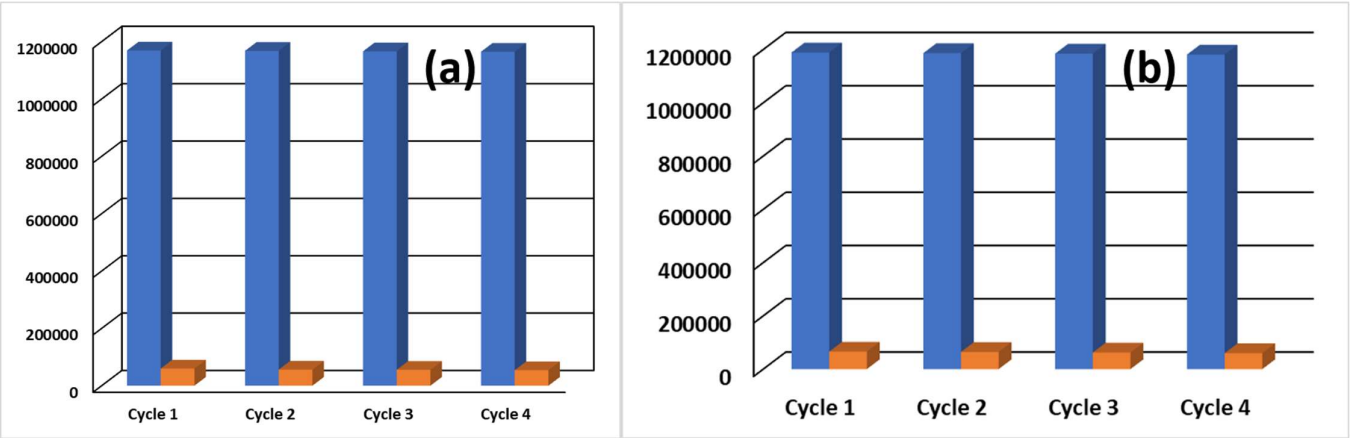

Figure S31: Recyclability of compound **7** as a sensor with Cr^{3+}(a) and Fe^{3+} (b). The intensity is measured at 543 nm (λex = 360 nm) for **7** and in presence of 5 x 10^{-4} M cation solutions

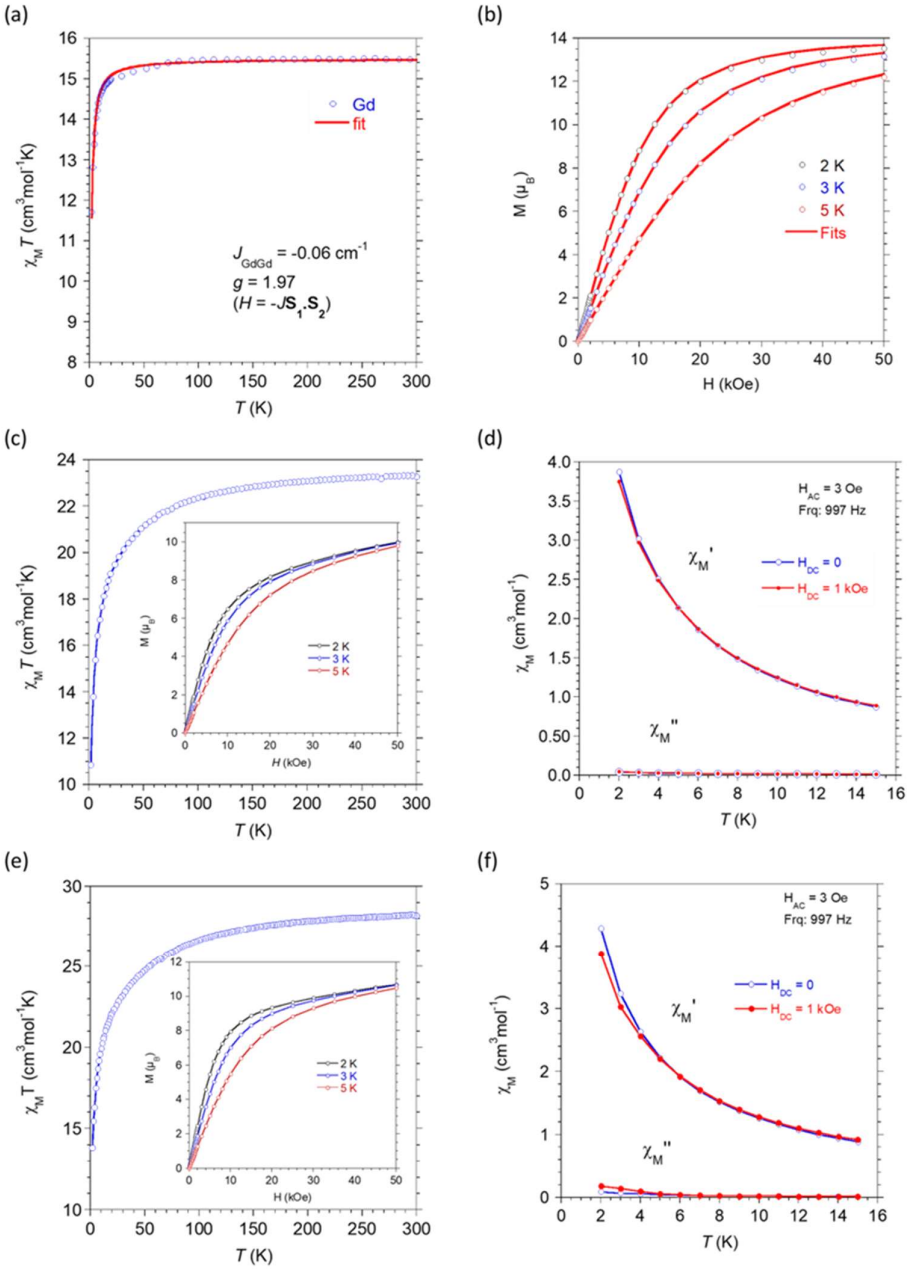

Figure S32: (a, b) Gd derivative **6**: $\chi_M T$ = f(T) and M =*f*(H) behaviors, the red full-lines are the best-fit modeling for. (c, d) Tb derivative **7**: $\chi_M T$ = f(T) and M =*f*(H) behaviors (inset), AC susceptibility in absence and with an applied field of 1 kOe. (e,f) Dy derivative **8**: $\chi_M T$ = f(T), M =*f*(H) (inset), and AC susceptibility in absence and with an applied field of 1 kOe.

Procedure of O-Arylation Reaction:

The O-Arylation reaction between Phenol (1 mmol, 0.094 g) (or β Naphthol, 0.144 g) and different Bromobenzene derivatives (1 mmol) was carried out in the presence of 1.5 mmol (0.487 g) of Cs_2CO_3, Tb-MOF catalyst (5 mg, 0.007 mol%) and 2 mL of DMF at 80 °C. The reaction mixture was allowed to react at 80 °C for 5 h. The progress of the reaction was monitored employing the thin layer chromatography employing ethyl acetate/*n*-hexane (10 % Ethyl acetate). After the reaction was completed, the reaction was cooled to ambient conditions, and the solid catalyst was separated by centrifuging from the reaction mixture. The catalyst was washed several times with fresh DMF and dried at 70 °C in an oven for 2 h, before using it again for the recycle studies under identical reaction conditions. The reaction mixture without the catalyst was extracted several times with ethyl acetate, concentrated and purified by column chromatography.

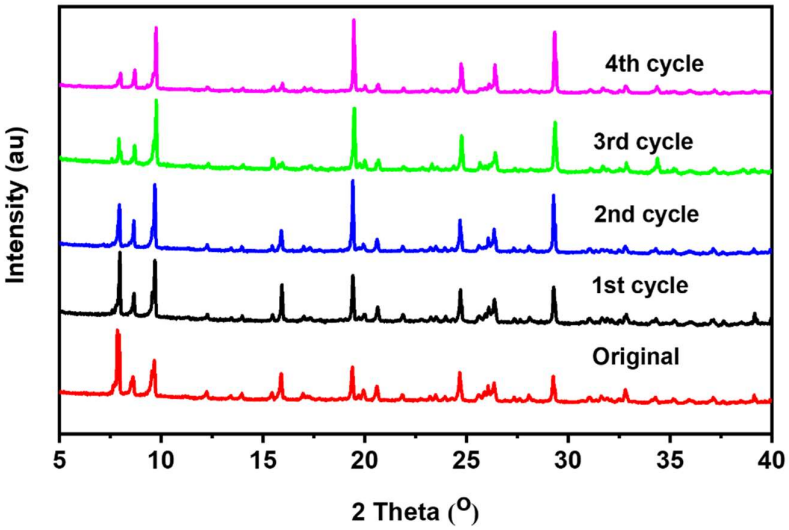

Figure S33: PXRD pattern of the catalyst during O-Arylation reaction in different cycle

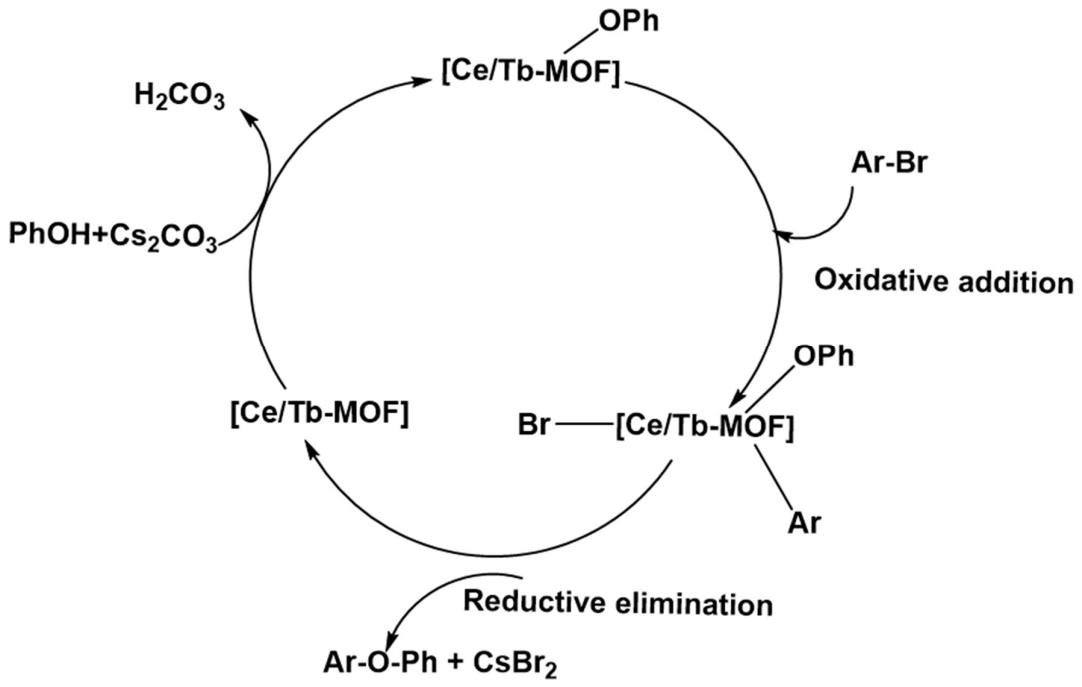

Figure S34: Plausible mechanism for the O-Arylation reaction.

^{1}H NMR Spectra for all the catalytic products: (Figure S35-S42)

^{1}H NMR (400 MHz, CDCl3) δ 7.83 – 7.08 (m, 8H), 6.99 (d, *J* = 8.8 Hz, 2H).

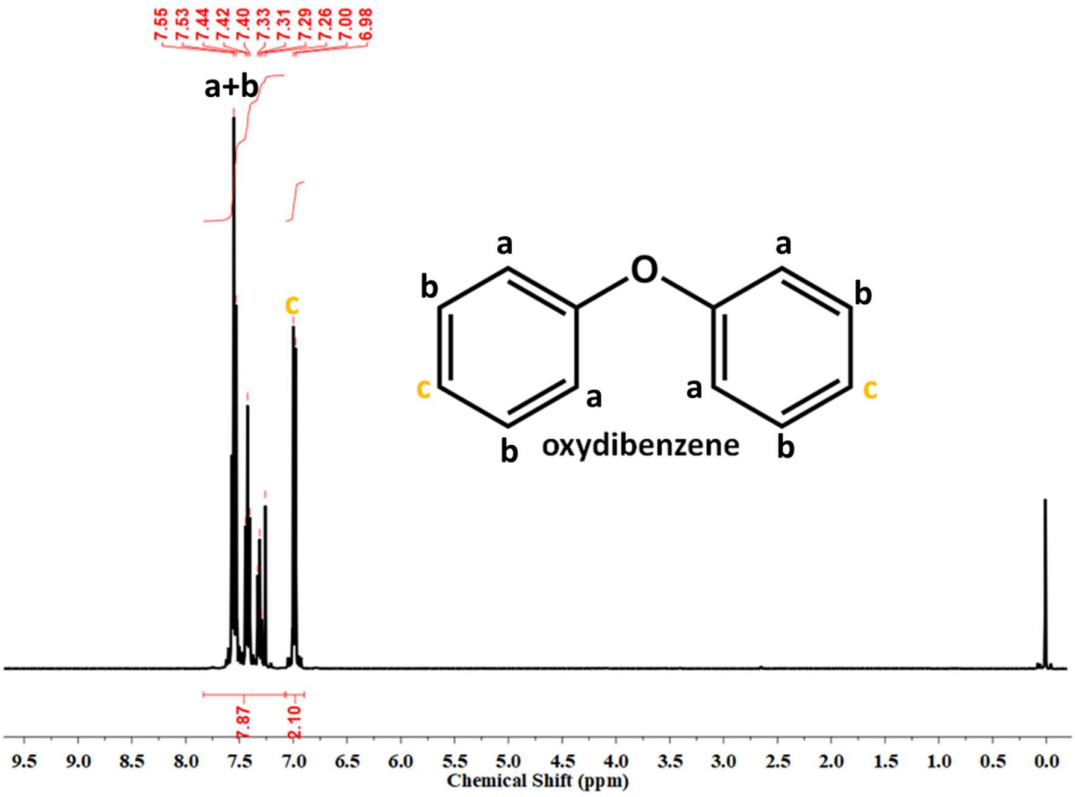

^{1}H NMR (400 MHz, $CDCl_3$) δ 10.11 (s, 1H), 8.03 (d, *J* = 8.6 Hz, 2H), 7.60 (t, *J* = 7.5 Hz, 3H), 7.44 (d, *J* = 7.2 Hz, 2H), 7.29 (s, 2H).

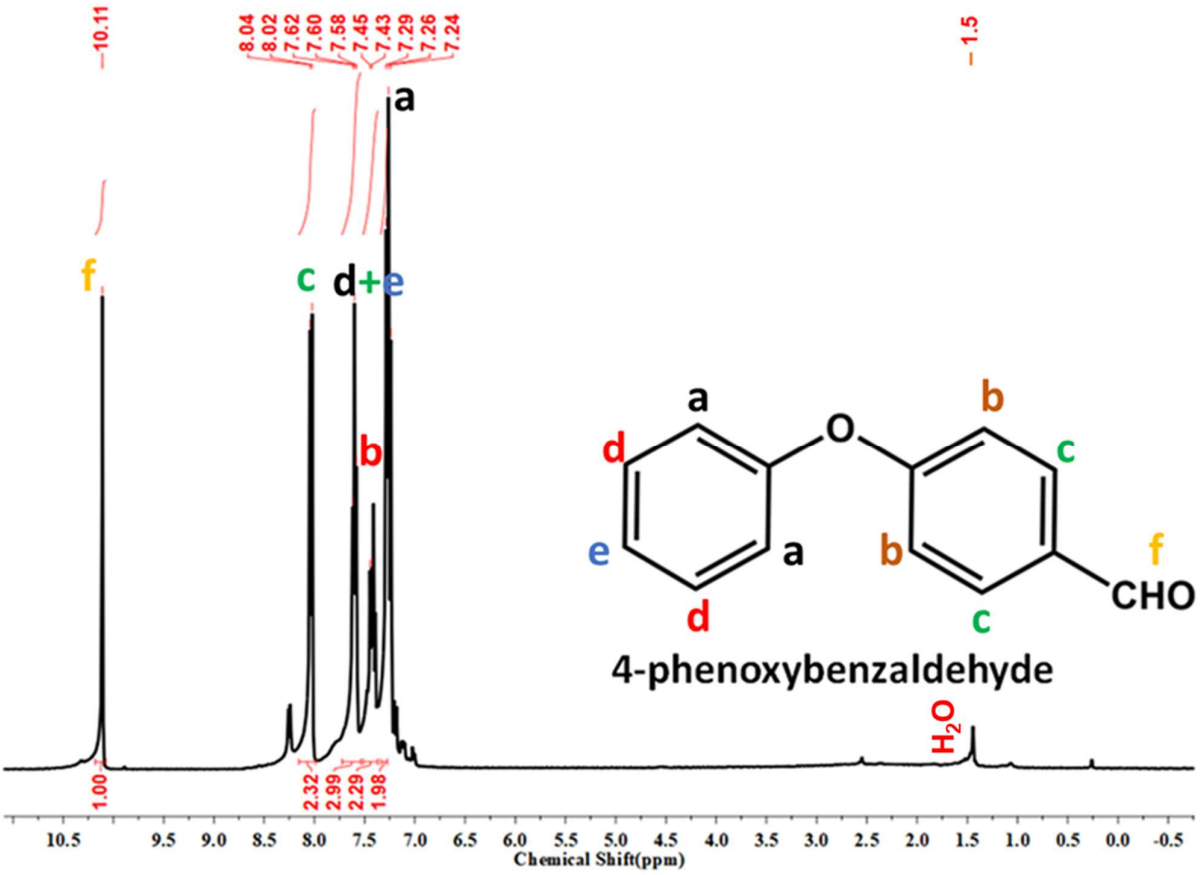

^{1}H NMR (400 MHz, $CDCl_3$) δ 7.59 (d, *J* = 8.9 Hz, 2H), 7.29 (d, *J* = 7.8 Hz, 2H), 7.02 (dd, *J* = 17.1, 8.3 Hz, 3H), 6.86 (d, *J* = 8.9 Hz, 2H).

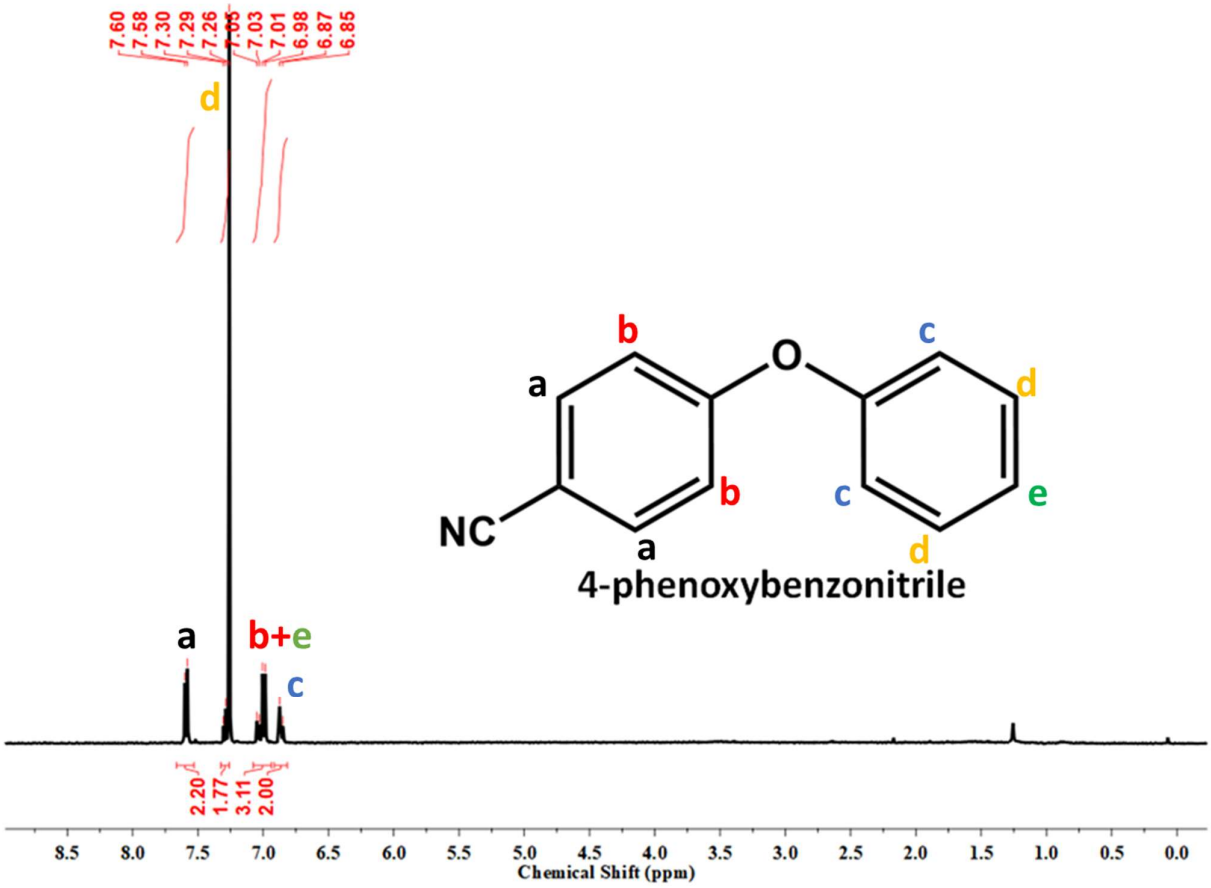

^{1}H NMR (400 MHz, $CDCl_3$) δ 8.17 (d, *J* = 8.8 Hz, 2H), 7.15 – 6.80 (m, 7H), 3.83 (s,3H).

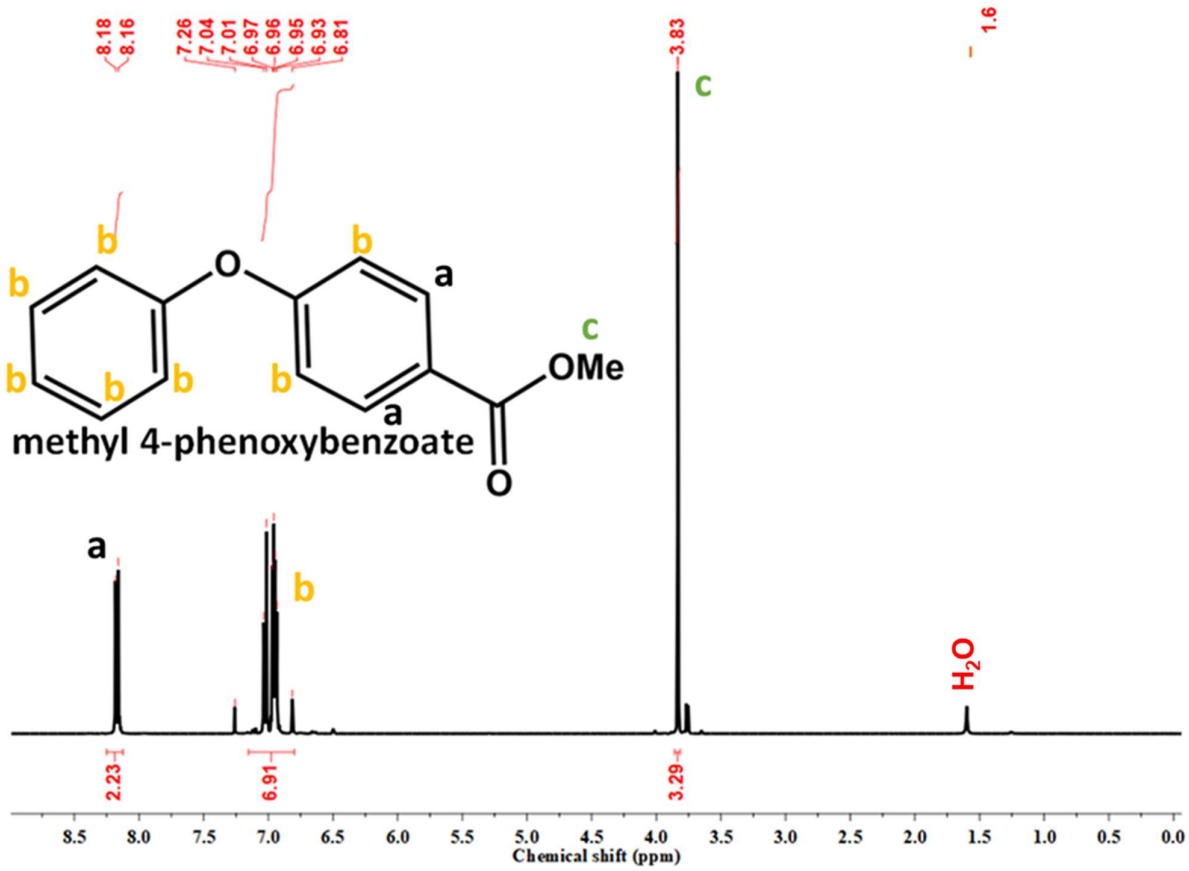

^{1}H NMR (400 MHz, $CDCl_3$) δ 7.83 (d, *J* = 8.8 Hz, 2H), 7.52 – 6.57 (m, 7H), 2.37 (s, 3H).

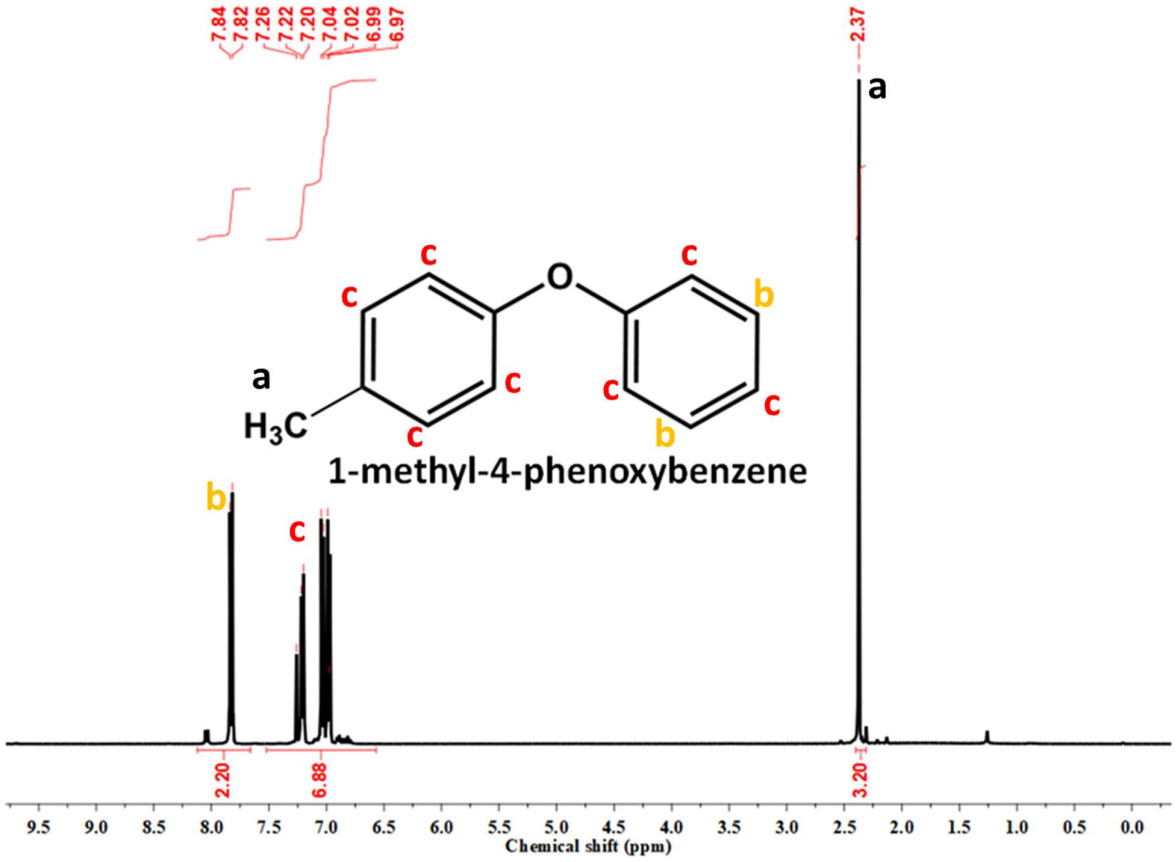

^{1}H NMR (400 MHz, $CDCl_3$) δ 8.24 – 8.12 (m, 2H), 7.24 – 6.47 (m, 7H).

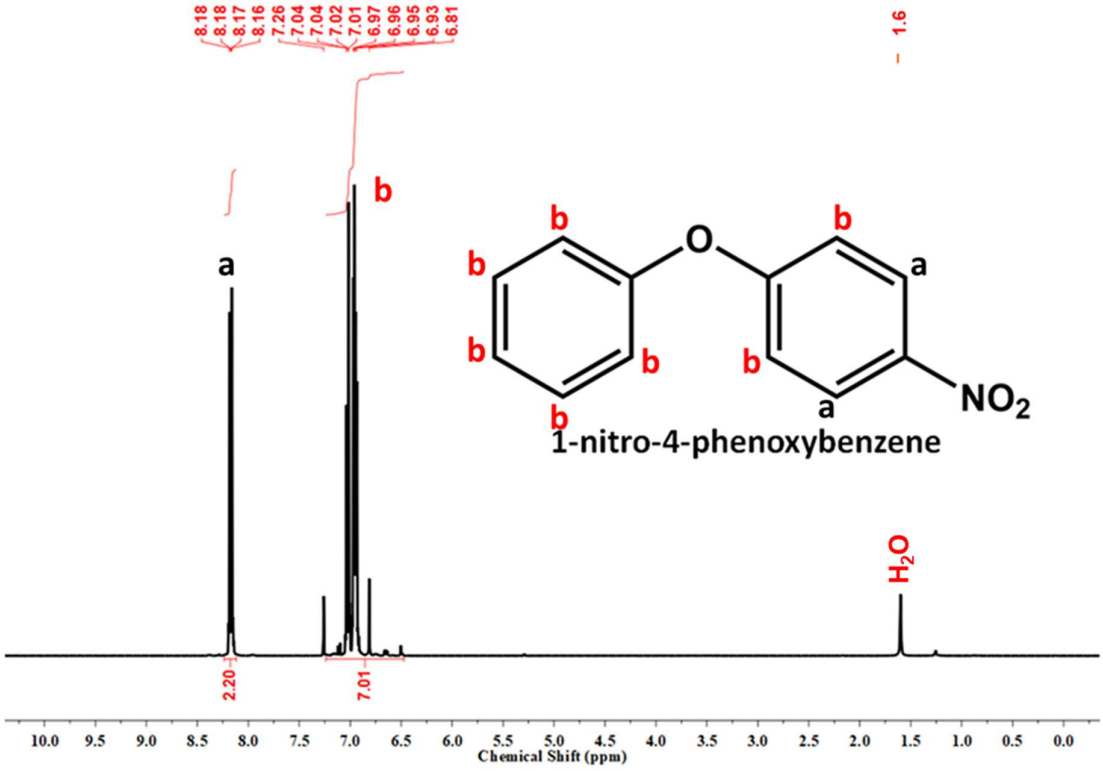

^{1}H NMR (400 MHz, $CDCl_3$) δ 7.59 (d, *J* = 7.8 Hz, 2H), 7.42 – 7.17 (m, 2H), 7.02 (dd, *J* = 18.8, 7.7 Hz, 3H), 6.86 (d, *J* = 10.4 Hz, 2H).

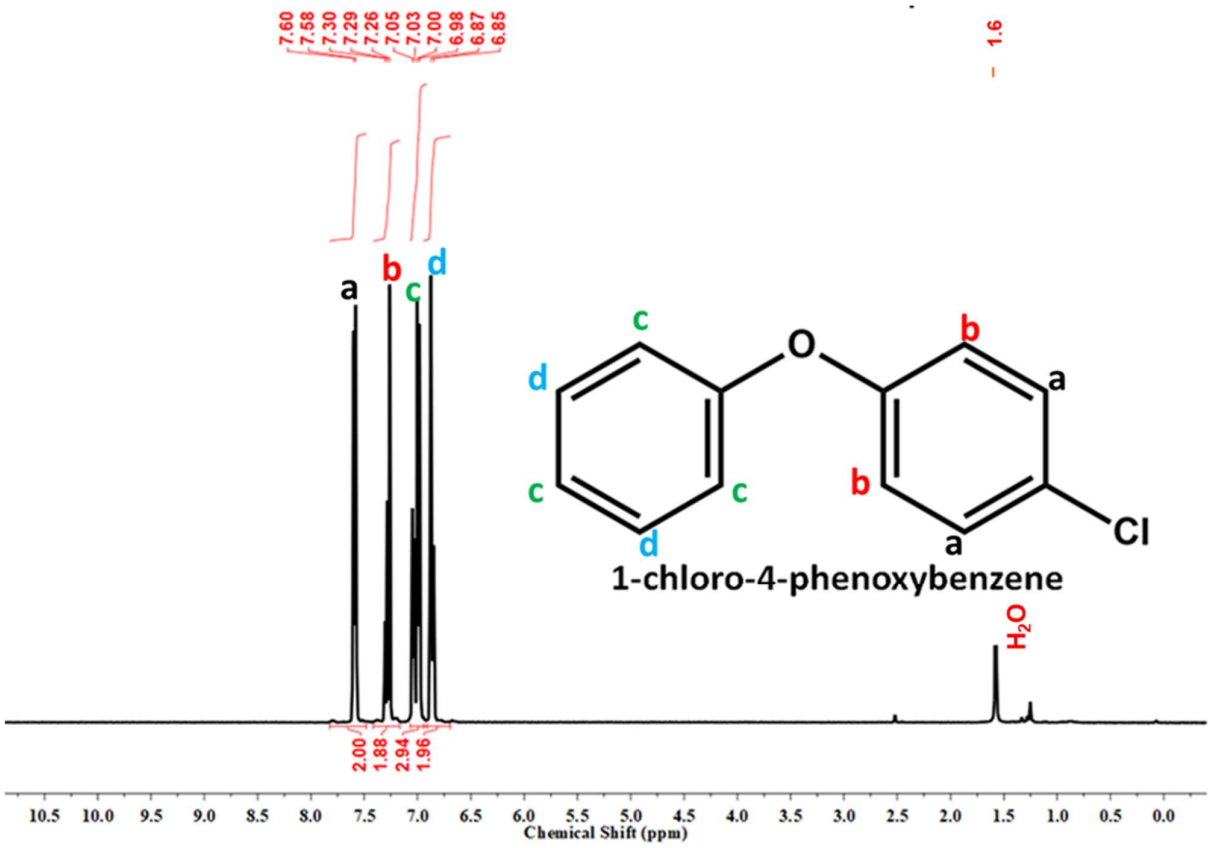

^{1}H NMR (400 MHz, $CDCl_3$) δ 8.19 (d, *J* = 8.6 Hz, 2H), 7.94 (d, *J* = 8.2 Hz, 2H), 7.79 (d, *J* = 8.3 Hz, 1H), 7.49 (d, *J* = 7.7 Hz, 2H), 7.18 (d, *J* = 7.5 Hz, 1H), 7.02 (d, *J* = 8.6 Hz, 2H).

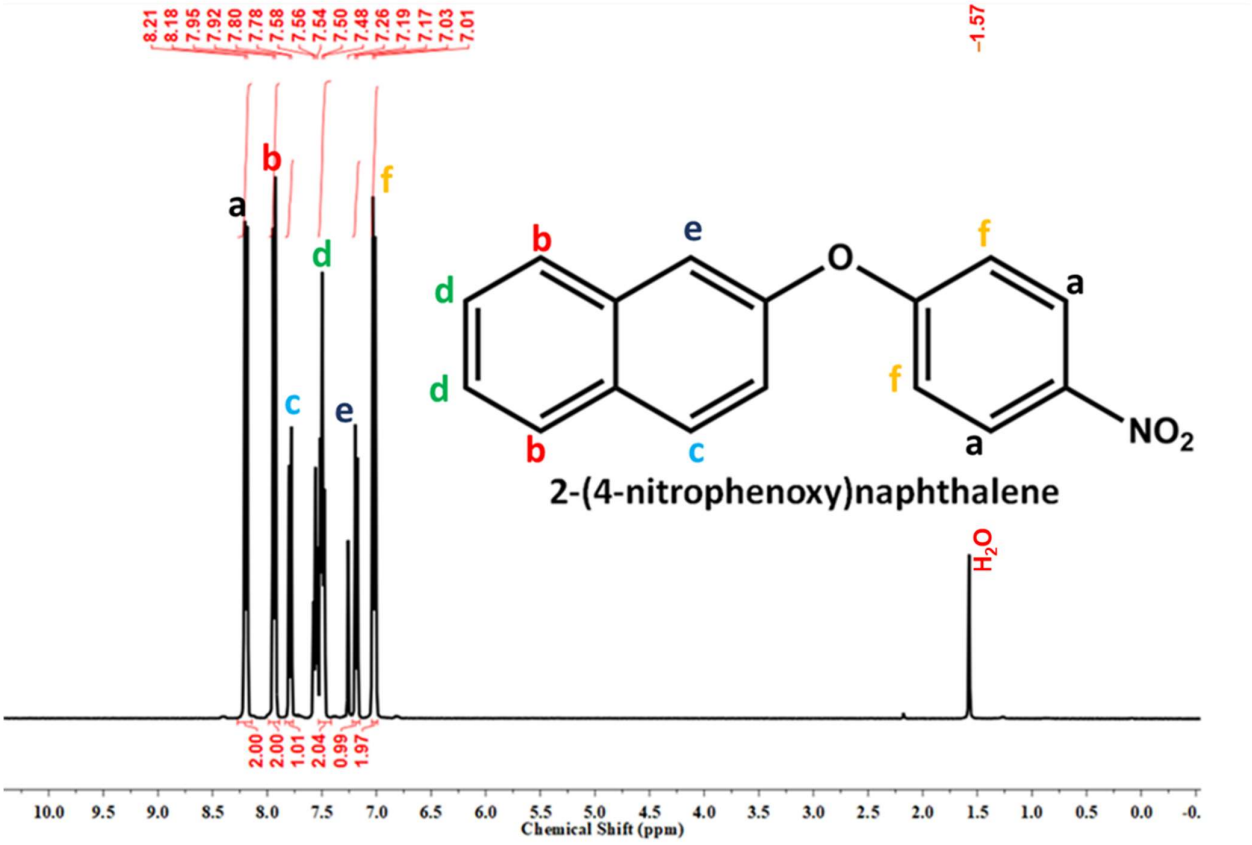

ESI-MS spectra for all the catalytic products: (Figure S43-S50)

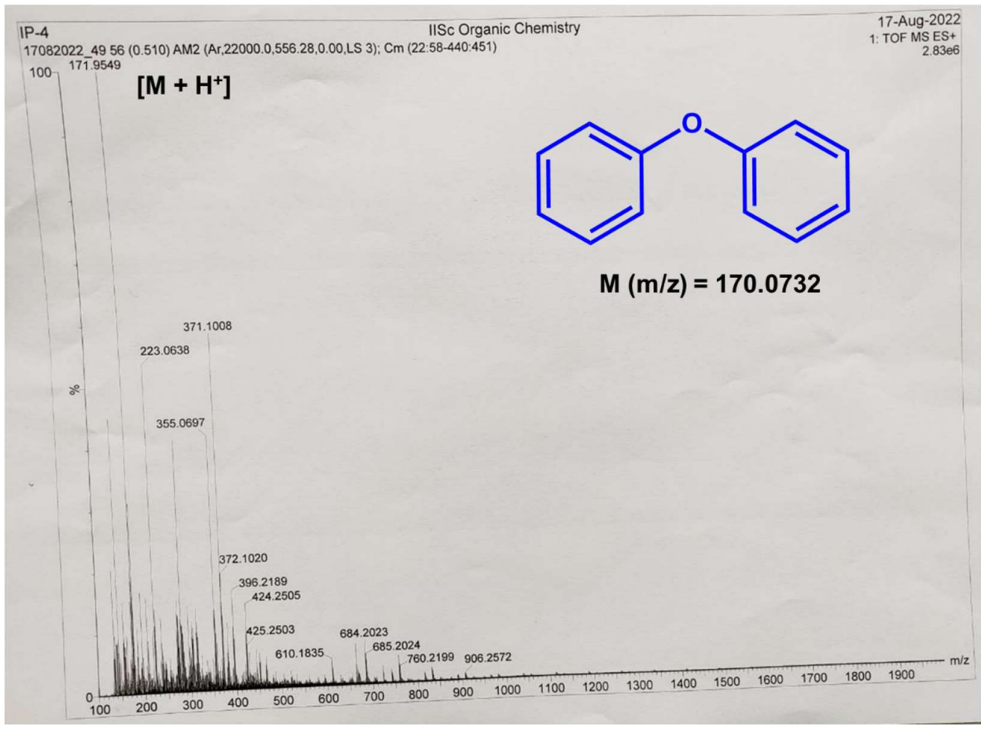

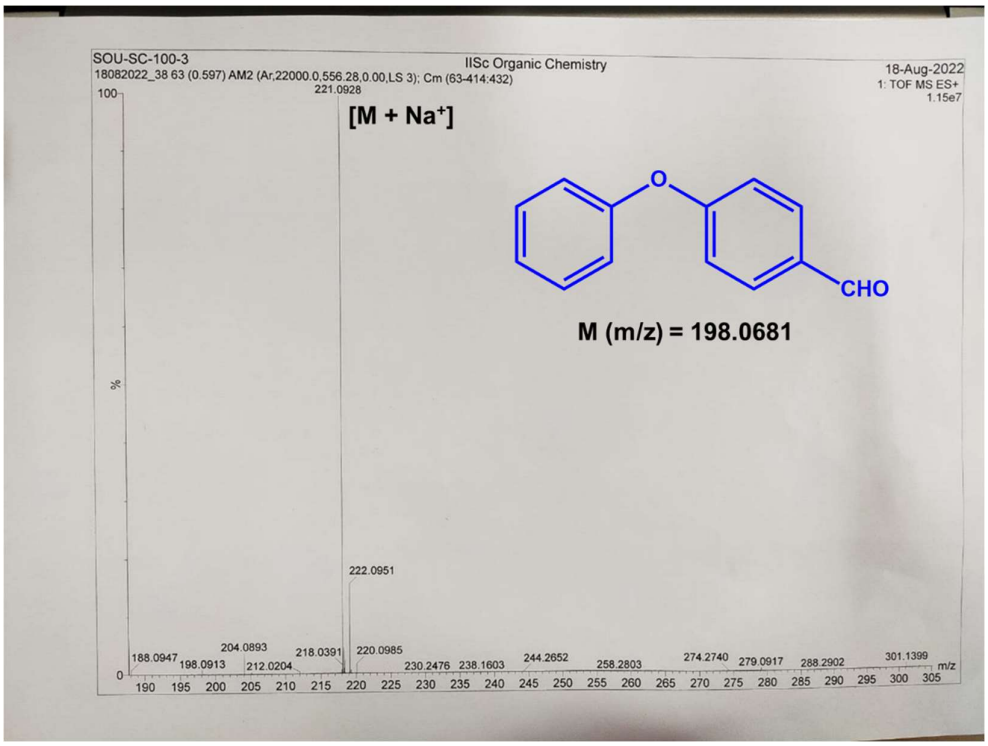

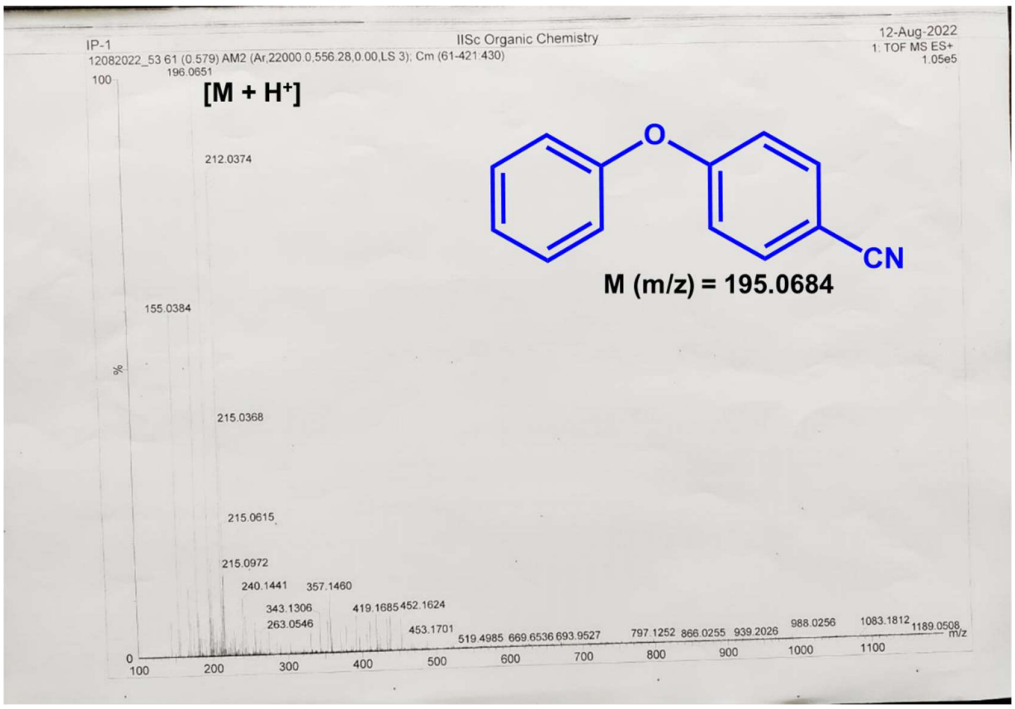
IP-1
IISc Organic Chemistry
12-Aug-2022
12082022_53 61 (0.579) AM2 (Ar,22000.0,556.28,0.00,LS 3); Cm (61-421:430)
1: TOF MS ES+
1.05e5
196.0651
[M + H+]
212.0374
155.0384
215.0368
215.0615
215.0972
240.1441
357.1460
343.1306
263.0546
419.1685
452.1624
453.1701
519.4985
669.6536
693.9527
797.1252
866.0255
939.2026
988.0256
1083.1812
1189.0508
m/z
O
CN
M (m/z) = 195.0684

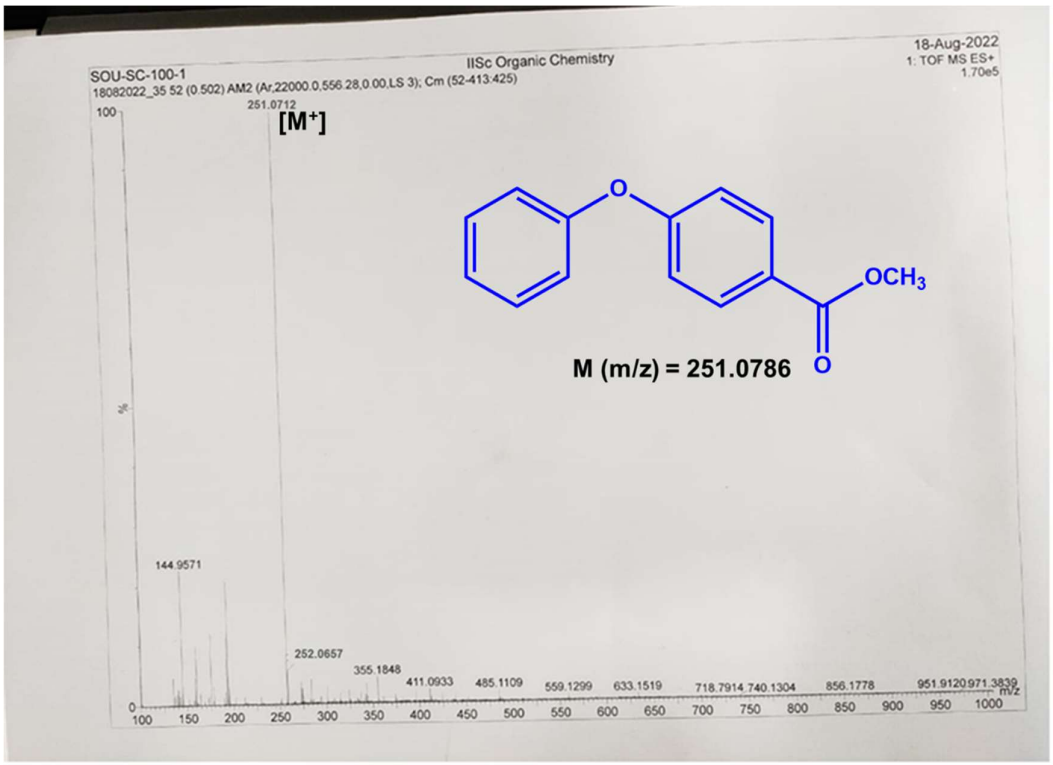
SOU-SC-100-1
IISc Organic Chemistry
18-Aug-2022
18082022_35 52 (0.502) AM2 (Ar,22000.0,556.28,0.00,LS 3); Cm (52-413:425)
1: TOF MS ES+
1.70e5
251.0712
[M+]
144.9571
252.0657
355.1848
411.0933
485.1109
559.1299
633.1519
718.7914
740.1304
856.1778
951.9120
971.3839
m/z
O
OCH3
O
M (m/z) = 251.0786

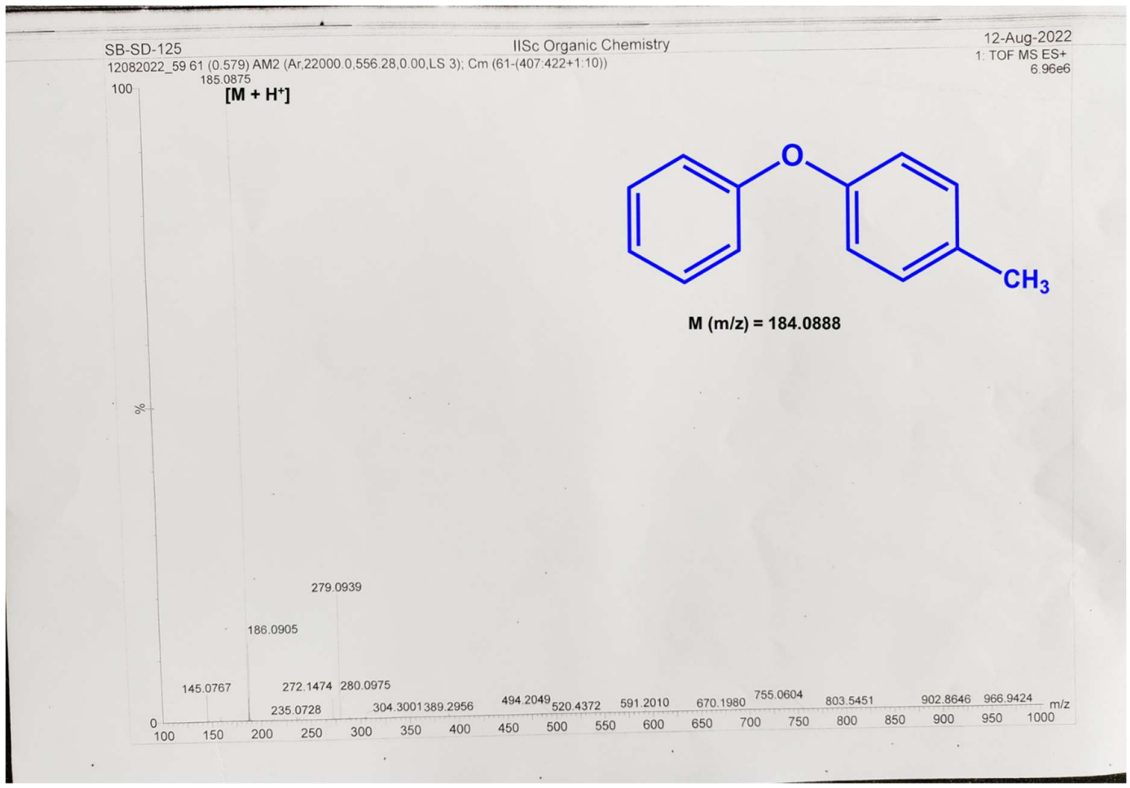
SB-SD-125
IISc Organic Chemistry
12-Aug-2022
12082022_59 61 (0.579) AM2 (Ar,22000.0,556.28,0.00,LS 3); Cm (61-(407:422+1:10))
1: TOF MS ES+
6.96e6
185.0875
[M + H+]
O
CH3
M (m/z) = 184.0888
279.0939
186.0905
145.0767
272.1474
280.0975
235.0728
304.3001
389.2956
494.2049
520.4372
591.2010
670.1980
755.0604
803.5451
902.8646
966.9424
m/z

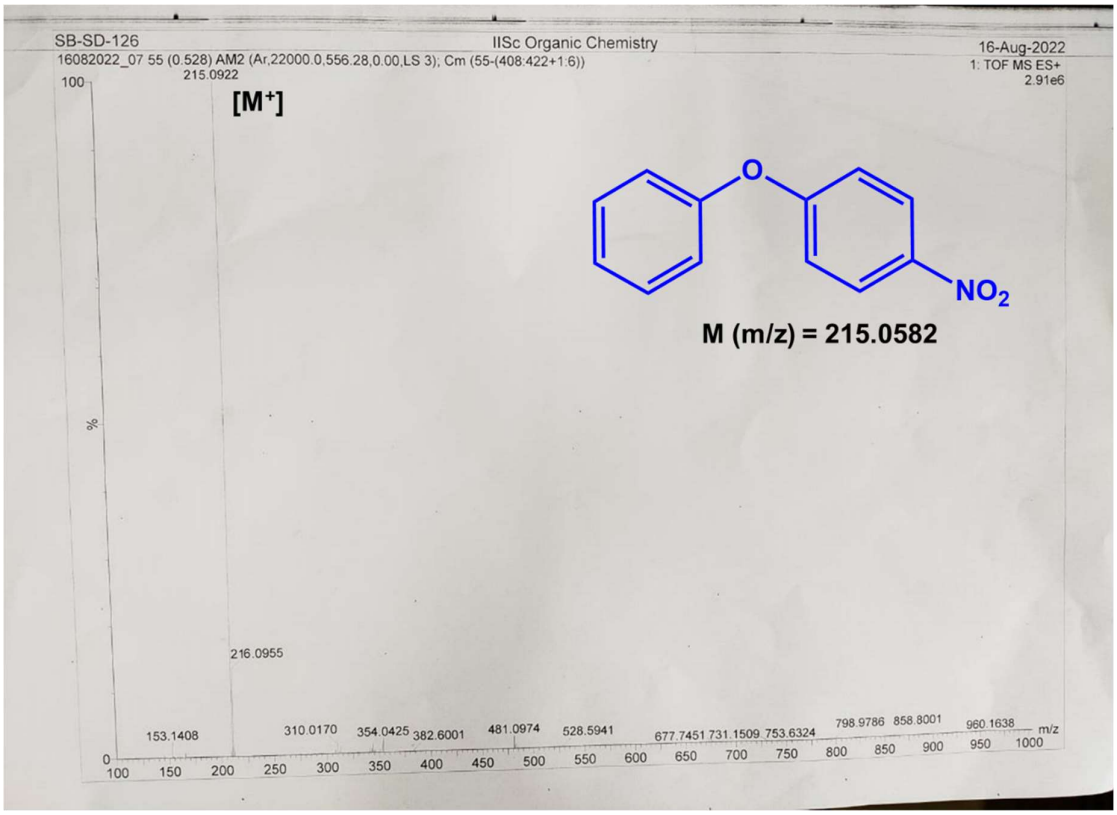
SB-SD-126
IISc Organic Chemistry
16-Aug-2022
16082022_07 55 (0.528) AM2 (Ar,22000.0,556.28,0.00,LS 3); Cm (55-(408:422+1:6))
1: TOF MS ES+
2.91e6
215.0922
[M+]
O
NO2
M (m/z) = 215.0582
216.0955
153.1408
310.0170
354.0425
382.6001
481.0974
528.5941
677.7451
731.1509
753.6324
798.9786
858.8001
960.1638
m/z

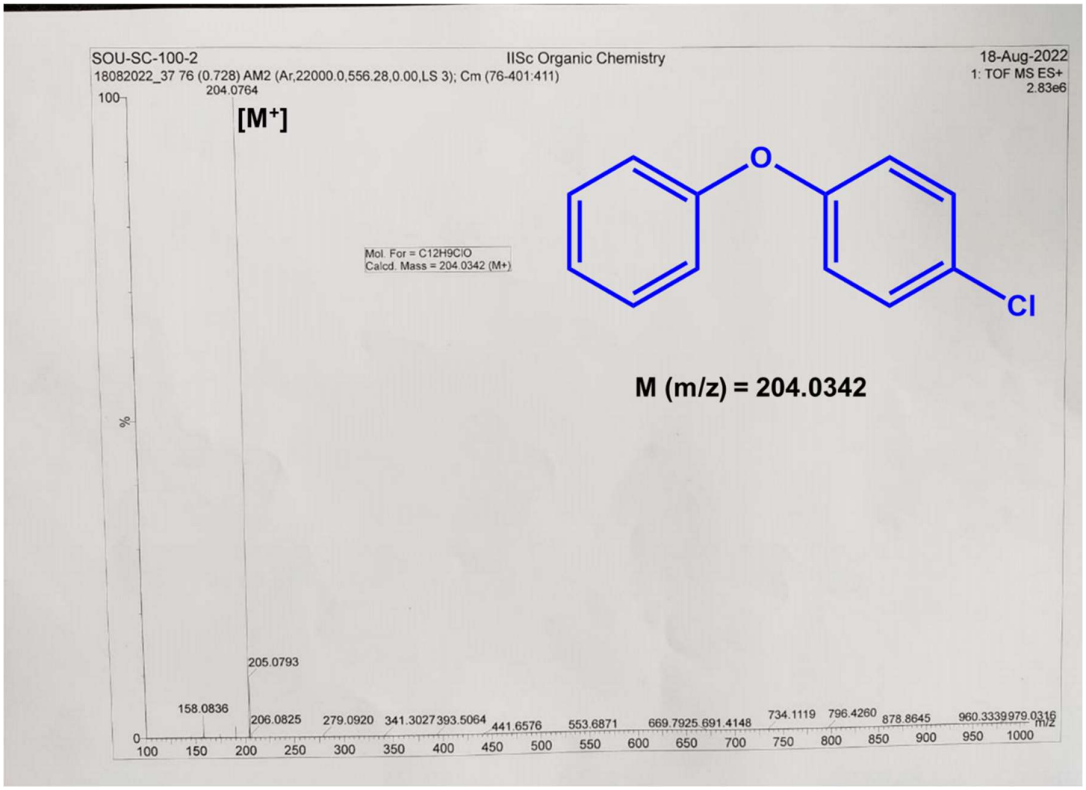
SOU-SC-100-2
IISc Organic Chemistry
18-Aug-2022
18082022_37 76 (0.728) AM2 (Ar,22000.0,556.28,0.00,LS 3); Cm (76-401:411)
1: TOF MS ES+
2.83e6
204.0764
[M+]
Mol. For = C12H9ClO
Calcd. Mass = 204.0342 (M+)
O
Cl
M (m/z) = 204.0342
205.0793
158.0836
206.0825
279.0920
341.3027
393.5064
441.6576
553.6871
669.7925
691.4148
734.1119
796.4260
878.8645
960.3339
979.0316
m/z

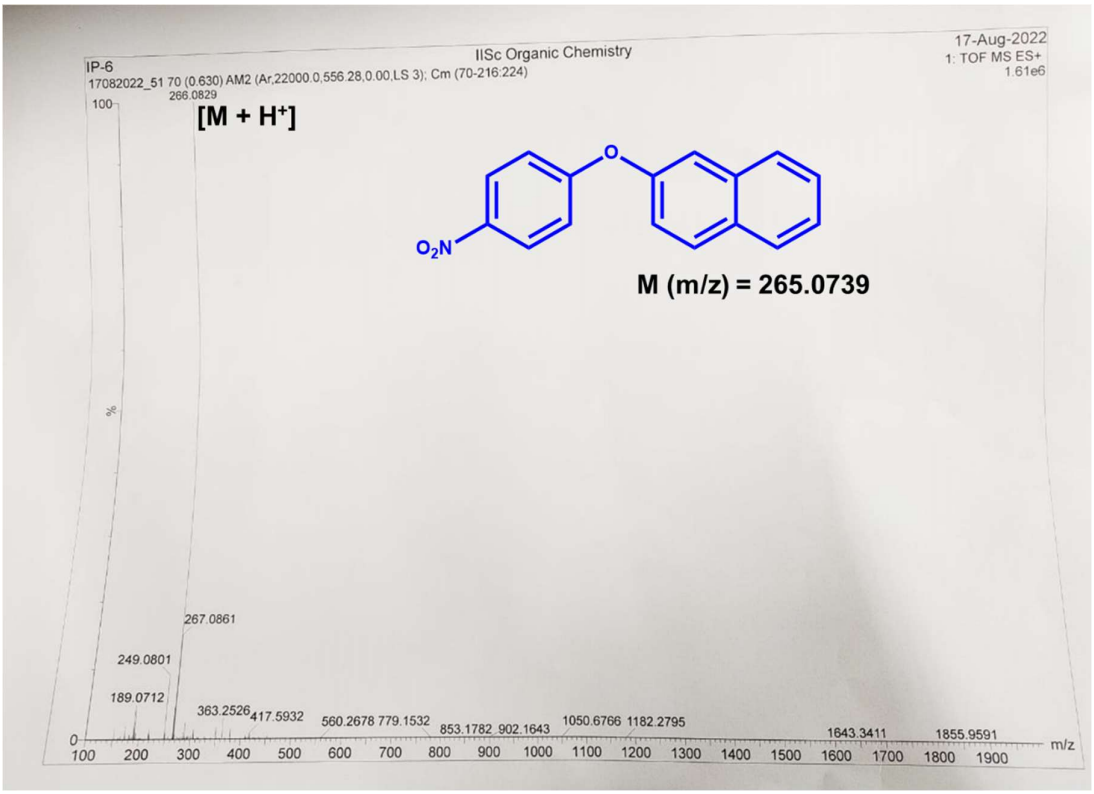
IP-6
IISc Organic Chemistry
17-Aug-2022
17082022_51 70 (0.630) AM2 (Ar,22000.0,556.28,0.00,LS 3); Cm (70-216:224)
1: TOF MS ES+
1.61e6
266.0829
[M + H+]
O
O2N
M (m/z) = 265.0739
267.0861
249.0801
189.0712
363.2526
417.5932
560.2678
779.1532
853.1782
902.1643
1050.6766
1182.2795
1643.3411
1855.9591
m/z